An Abstract of the Thesis of

Mark Alson Gummin for the degree of Doctor of Philosophy in Physics presented on April 16, 1992.

Title: Nuclear Structure Studies of ^{187,189}Ir via Low Temperature Nuclear Orientation and Coincidence Spectroscopy

Abstract approved: Redacted for Privacy

Kenneth S. Krane

The nuclear structure of odd-proton ^{187}Ir was studied following radioactive decay of mass-separated Pt. Two experiments were done: the initial experiment was a nuclear orientation study in which gamma-ray angular distributions were measured from ^{187}Pt oriented in an iron host. Existing spectroscopic information about ^{187}Ir was very incomplete, making a second experiment necessary in which gamma-ray and electron singles and γ-γ and γ-e coincidences were observed. Both experiments were performed at the UNISOR facility of the Holifield Heavy-Ion Research Facility at Oak Ridge, Tennessee. A detailed level scheme is presented, accounting for approximately 92% of the gamma-ray intensity, and including transitions up to 2.4 MeV. The focus of this work has been to measure multipole mixing ratios $\delta(E2/M1)$ of transitions in ^{187}Ir in order to elucidate the nuclear structure. A particle-plus-triaxial-rotor model (PTRM) was used to interpret the data, and mixing ratios calculated in that model are shown to agree very well with data for transitions among the positive-parity bands.

In a second set of experiments, the ^{189}Ir nucleus was studied. A spectroscopic study was again performed in which γ-γ and γ-e coincidences and multiscaled γ-ray and conversion electron singles events were observed. Nuclear orientation of ^{189}Pt was then performed, and angular distributions for the 100 most intense transitions were found. Multipole mixing ratios were derived from those distributions and again compared to theoretical results from the PTRM.

Nuclear Structure Studies of ^{187,189}Ir via Low Temperature Nuclear Orientation and Coincidence Spectroscopy

by

Mark Alson Gummin

A THESIS

submitted to

Oregon State University

in partial fulfillment of
the requirements for the
degree of

Doctor of Philosophy

Completed April 16, 1992

Commencement June 1992

Approved:

Redacted for Privacy

Professor of Physics in charge of major

Redacted for Privacy

Chairman of the Department of Physics

Redacted for Privacy

Dean of Graduate School

Date thesis is presented April 16, 1992

Typed for Mark A. Gummin by Mark A. Gummin

There is such magnificent vagueness in the expectations that had driven each of us to sea, such a glorious indefiniteness, such a beautiful greed of adventures that are their own and only reward! What we get -well, we won't talk of that; but can one of us restrain a smile? In no other kind of life is the illusion more wide of reality -in no other is the beginning *all* illusion -the disenchantment more swift -the subjugation more complete.

from **Lord Jim** by Joseph Conrad

Acknowledgements

This project could not have been realized without a great deal of help from many friends, colleagues, and mentors. I would like to take this time to convey my deepest gratitude to all who have helped me along the way.

I would like to express my most sincere appreciation to my advisor Dr. Kenneth S. Krane, whose keen foresight and immeasurable wisdom have rescued me many times from the near edge of Charybdis. Ken's careful and systematic approach to problem solving has provided a very valuable lesson, and I hope that I have learned by his example.

I would also like to give special thanks to my friends and colleagues Yueshu Xu, Laura VanWormer, Axel Vischer, Shiby Paulose, Uwe Schmid, Prasanna Samarawickrama, and Martin Fuchs for their unending encouragement, advice, and companionship. Their friendship has helped to make graduate school a very memorable experience.

All of the members of the UNISOR collaboration have contributed in many ways to this work, and for that I am deeply indebted. Particular thanks are due Drs. Ken Carter, Jan Kormicki, Paul Semmes, John Wood, and Ed Zganjar. The comradery established during many long graveyard shifts at UNISOR has provided a foundation for the special appreciation of Jürgen Breitenbach, Jing-Kang Deng, Paresh Joshi, Tak Lam, Dubravka Rupnik, and Brian Zimmerman.

Table of Contents

List of Figures

List of Tables

Nuclear Structure Studies of ^{187,189}Ir via Low Temperature Nuclear Orientation and Coincidence Spectroscopy

1. Introduction

The isotopes of Ir-Pt-Au-Hg around $A=187$ lie near a closed proton shell at $Z=82$ and a half-filled neutron shell at $N=104$. This is a transitional region in which the nuclei are changing with increasing mass from prolate towards more oblate shapes. Nuclei in this region have a very rich structure, with rotational bands built upon oblate, prolate, or triaxial shapes, and excitations due to beta- and gamma-vibrational bands as well. A large number of transitional nuclei are also known to display shape coexistence (see review by [Ham85]), in which the nucleus can exhibit bands with, for example, both prolate and oblate deformations. This widely manifested phenomenon is illustrated by the existence of bands with different deformations (strong in-band $B(E2)$ values indicating stable deformations for the bands), and is emphasized by transitions among those bands.

The transitional odd-mass iridium nuclei in this region exhibit very gradual, predictable changes in spectroscopic quantities (mixing ratios, level energies, static and transitional moments, etc.) across a broad range of neutron numbers. A rather dramatic shape transition occurs at mass 185, however, where the ground state has been identified by Schuck *et al.* [Sch79] as the $I=5/2$ member of the $1/2^-[541]$ Nilsson state rather than the $3/2^+[402]$ state, which characterizes the heavier Ir isotopes. Level energy systematics are shown for the odd-A Ir isotopes in Figure 1 to illustrate the smooth behavior as neutron number changes. Electric quadrupole moments of the odd-A isotopes are shown in Table 1. The intrinsic moments Q_0 (calculated in the limit of good K, since K is no longer a good quantum number when axiality is lost) are also seen to increase continuously with decreasing mass until mass 185, where there is a rather large prolate deformation. The rather high degree of K-mixing due to the triaxiality clouds this picture somewhat, but it seems clear that the general shape transition is understood correctly. Finally, the multipole mixing ratios

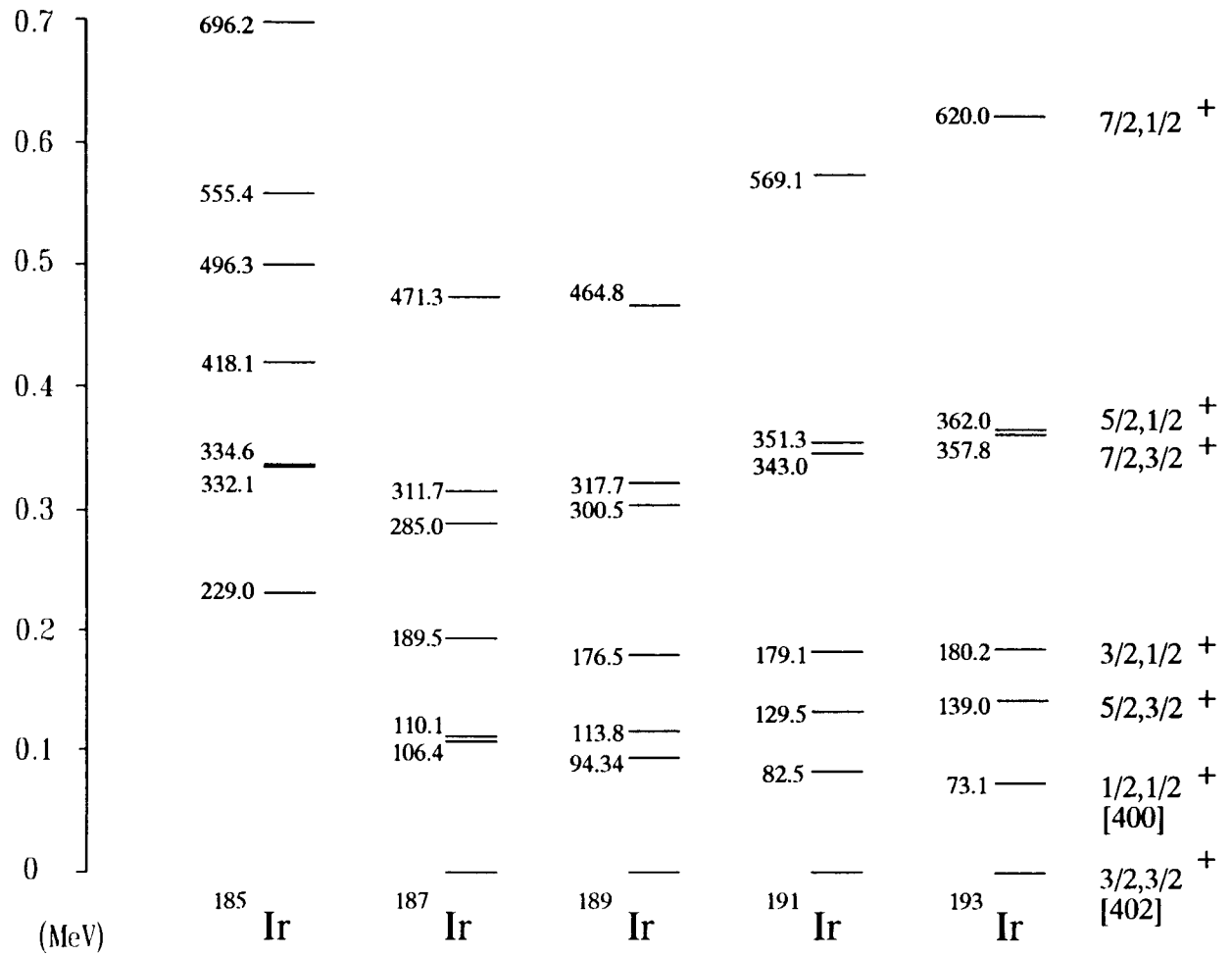

Figure 1 Systematics of level energies for odd-A Ir isotopes. Spin-ordering is the same for each isotope.

are also seen to change very systematically in this mass region. Mixing ratios for selected low-lying positive-parity transitions are shown in Table 2. The strikingly predictable systematic behavior of these isotopes makes a study of their low-lying properties very interesting, and provides a more complete data base with which to test the theoretical models.

Table 1 Spectroscopic and intrinsic quadrupole moments of Ir isotopes. Intrinsic moments are calculated in the axial limit (no K-mixing). The trend is clearly toward large prolate deformation at $A=185$. The ground-state moment is unknown for ^{187}Ir.

A	Q_{spect}(b)[a)]	$I,K^{\pi}[Nn_z\Lambda]$	Q_0(b)
185	-2.06(14)	$5/2,1/2^+[541]$	7.21(49)
187	3.1(3)	$11/2,11/2^-$	5.1(5)
189	1.04(20)	$3/2,3/2^+[402]$	5.2(10)
191	0.816(9)	$3/2,3/2^+[402]$	4.08(5)
193	0.751(9)	$3/2,3/2^+[402]$	3.76(5)

a) From [Rag89].

Table 2 Mixing ratio systematics for three transitions in odd-A Ir isotopes. Signs for ^{187}Ir and ^{189}Ir are from the present work. Note the very systematic change in δ with increasing A.

A	$\delta(E2/M1)$ $5/2^+\rightarrow 3/2^+[402]$	$\delta(E2/M1)$ $3/2^+[400]\rightarrow 3/2^+[402]$	$\delta(E2/M1)$ $7/2^+\rightarrow 5/2^+[402]$
187	−0.64(8)	−0.6(3)	-0.9^{+13}_{-6}
189	−0.55(3)	−0.89(4)	−0.53(6)
191	−0.44(4)	−0.75(3)	−0.34(4)
193	−0.329(12)	−0.48(2)	−0.34(4)

An interesting question concerning the structure of ^{187}Ir is whether the nucleus should be described as a rigid triaxial or a gamma-soft axial rotor. Recent potential

energy surface calculations by Bengtsson *et al.* [Ben87] indicate that for the even-even cores of ^{187}Ir: ^{186}Os should have a single, prolate minimum (with a deformation of around $0.2 \leq \beta_2 \leq 0.25$), and ^{188}Pt a very γ-soft potential energy surface. For the ^{189}Ir cores: ^{188}Os is predicted to have the same prolate minimum as ^{186}Os, while ^{190}Pt is expected to lie near maximum triaxiality at $\gamma = 50°$. In the absence of strong polarization effects, single-particle levels built upon those configurations should reflect one of the two core-structures. (Results from representative Potential Energy Surface calculations are shown in Chapter 6 for ^{187,189}Ir.) It is difficult if not impossible experimentally to distinguish between a weakly-deformed triaxial and a γ-soft nucleus, but impressive agreement with the rigid-rotor model lends credence to that picture, as will be demonstrated below. Another interesting feature of the odd-A Ir nuclei is the strong feeding of the $I=3/2$ level of the $1/2^+[411]$ band (Ghaleb and Krane [Gha84] for ^{193}Ir, Lattimer *et al.* [Lat81] for ^{191}Ir, Hedin and Backlin [Hed72] for ^{189}Ir, and Sebille-Schuck *et al.* [Sch73] for ^{187}Ir). Systematics of this rather interesting structure are shown in Figure 2 for $A=189$ to $A=193$.

The structure of odd-mass isotopes in this region has been described successfully by various theoretical models. While the microscopic models (see [Sah81] and [Naz90], for example) are generally very successful, the more phenomenological particle-rotor codes seem to do a better job describing multipole mixing ratios, which is the primary goal of the present work. The signs of the mixing ratios are of particular interest, since they carry a great deal of information about the nuclear wavefunction. Consequently a particle-rotor model was used for all theoretical comparisons with experimental data. Properties of interband transitions are generally difficult to calculate if the deformations are widely different for the bands involved in the transition. In the case of ^{187}Ir, however, most of the low-lying structure is due to positive-parity bands with similar deformations, the $3/2^+[402]$ and $1/2^+[400]$. This situation conveniently lends itself to calculations of interband transition rates.

The present investigation is part of an overall plan to track the systematics of the lighter mass, odd Ir isotopes from $A=185$ to 189 and to understand the low-lying structure within the framework of a well-known theoretical model. The point, here,

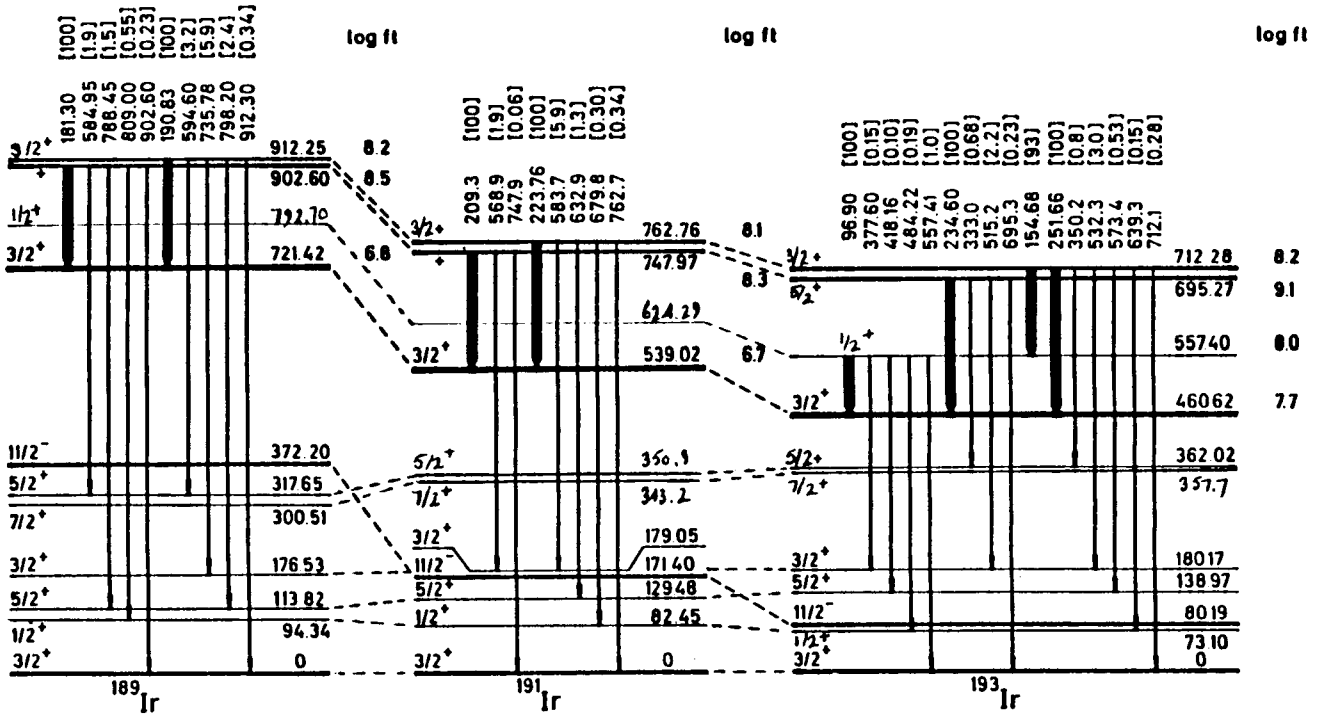

Figure 2 Systematics of the strongly-fed Ir $3/2^+$,$5/2^+$ levels. Much of the structure is from the $1/2^+$[411] level. (Taken from [Hed72].)

is not to "prove" any assumptions about the nuclei being studied or the theoretical model that is used. Rather, it is to gain extra insight into the structure of the nucleus using that model, and to provide a foundation upon which to base some conclusions. With this tenet, then, we will treat the ^{187}Ir and ^{189}Ir nuclei as rigid, "prolatish," triaxial rotors and compare experimental results from nuclear orientation and conversion-electron and gamma-ray spectroscopy with calculations from the particle-plus-triaxial-rotor model.

2. Nuclear Orientation Theory

The probability distribution of radiation (electromagnetic or particle) from a nucleus of spin I_0 is not isotropic in space, but has an angular distribution which depends upon that spin, the *character* of the radiation, and the radiation multipolarity L. The transition takes place between levels $I_i\pi_i \rightarrow I_f\pi_f$ such that the character, X, of the radiation is said to be *electric* if the product of parities is equal to $\pi_i\pi_f=(-1)^L$, and *magnetic* if the product is given by $\pi_i\pi_f=(-1)^{L+1}$. If $\pi_i\pi_f$ is positive, the radiation is $M1$, $E2$, $M3$..., and $E1$, $M2$, $E3$... if it is negative.

The extension from a single nucleus to an ensemble of radiating nuclei is straight forward. If the nuclear spins are randomly oriented, the distribution of radiation is isotropic. If, on the other hand, the spins are oriented along a similar axis, the angular distribution will be a superposition of probability distributions for each nucleus. In that case the orientation of the ensemble is described by a statistical tensor $\rho_q^\lambda(I_0)$, and the emitted radiation is described by the angular distribution coefficient $A_{\lambda q'}(X;Q)$. The most general form for the angular distribution of radiation from an ensemble of oriented nuclei is given in terms of those quantities as [Kra86]

$$W(\boldsymbol{k},Q) = \frac{d\Omega}{4\pi}\hat{I}_0 \sum_{\lambda q q'} \rho_q^{\lambda *}(I_0) A_{\lambda q'}(X;Q) D^{(\lambda)}_{qq'}(\boldsymbol{e}_z \rightarrow \boldsymbol{k}\boldsymbol{x}'), \qquad (1)$$

which describes the probability of observing radiation of character X emitted into the solid angle $d\Omega$ along the $\boldsymbol{k}$ direction. The D-function maps the oriented spin-quantization axis $\boldsymbol{e}_z$ into the detector coordinate system given by $\boldsymbol{k}$ and $\boldsymbol{x}'$, with $\boldsymbol{x}'$ representing the polarization axis of the detector. The parameter Q accounts for the detector polarization efficiency. For so-called directional distribution measurements the polarization of radiation is not observed, and only the $q'=0$ components are retained. In this case the D-functions are given by the spherical harmonics, $Y_{\lambda q}(\theta,\varphi)$. Similarly, for oriented states which are axially symmetric, only the $q=0$ components are non-zero, in which case the spherical harmonics reduce to ordinary Legendre polynomials. Finally, additional corrections are applied to the angular distribution in

order to account for intervening radiations and finite detector solid angles, as will be discussed below.

Nuclear orientation experiments are performed by orienting nuclei in one of two ways: Electric quadrupole interactions, whereby nuclear quadrupole moments interact with local electric field gradients, or magnetic dipole interactions ($H=-\boldsymbol{\mu}\cdot\boldsymbol{B}$), in which the nuclear magnetic moments interact with local magnetic fields. Since the present work has been done using magnetic dipole interactions, all following discussions will be based on that method.

The statistical tensors in the case of axial symmetry are given by the orientation parameters $B_\lambda(I_0)$ as

$$\rho_q^\lambda(I_0) = (\hat{I}_0)^{-1} B_\lambda(I_0)\delta_{q0}. \tag{2}$$

The orientation parameter B_λ describes the degree of orientation reached for a given temperature (at which the ensemble is considered to be in thermodynamic equilibrium, having a Boltzmann distribution of magnetic substates, m). The tensors are defined in terms of the density matrix ρ which describes the orientation. The density matrix is given by

$$\rho_q^\lambda(I_0) = \hat{\lambda}\sum_m (-1)^{I_0+m'} \begin{pmatrix} I_0 & I_0 & \lambda \\ -m' & m & q \end{pmatrix} \langle I_0 m | \rho | I_0 m' \rangle , \tag{3}$$

where the term in parentheses is the Wigner 3-J symbol and $\hat{x}$ means $(2x+1)^{1/2}$. For magnetic dipole interactions the operator is written as

$$\rho = \frac{\exp(\boldsymbol{\mu}\cdot\boldsymbol{B}/kT)}{Tr[\exp(\boldsymbol{\mu}\cdot\boldsymbol{B}/kT)]}. \tag{4}$$

The angular distribution is axially symmetric for (parity conserving) gamma radiation, and, so long as polarization is not measured, the general form for the distribution reduces to an expansion of even powers of the Legendre polynomials as

$$W(\theta) = \sum_{\lambda\ even} a_\lambda Q_\lambda P_\lambda(\cos\theta) \tag{5}$$

where

$$a_\lambda = B_\lambda(I_0, T) U_\lambda(I_i I_f L) A_\lambda(I_i I_f L). \tag{6}$$

Equation (5) is in the form most often used for gamma-ray studies of angular distributions from oriented nuclei. The matrix elements in Equation (3) above are then given by the population parameters

$$\langle I_0 m | \rho | I_0 m' \rangle = p(m)\delta_{mm'} = \frac{\exp(m\Delta_M/T)}{\sum_m \exp(m\Delta_M/T)}, \tag{7}$$

and related to the orientation parameters so that

$$B_\lambda(I_0, T) = \hat{\lambda}\hat{I}_0 \frac{\sum_m (-1)^{I_0+m} \begin{pmatrix} I_0 & I_0 & \lambda \\ -m & m & 0 \end{pmatrix} \exp(m\Delta_M/T)}{\sum_m \exp(m\Delta_M/T)}. \tag{8}$$

The Δ_M is the difference in energy between adjacent magnetic substates and is given by

$$\Delta_M = \mu B_z / k I_0. \tag{9}$$

For purposes of calculating orientation parameters, Δ_M is given in millikelvin as

$$\Delta_M = \frac{0.366\,\mu B_z}{I_0}, \tag{10}$$

where the magnetic moment μ is measured in nuclear magnetons and the field strength B_z is in tesla. All temperature dependence of the angular distribution is included in the B_λ, and the largest term in the angular distribution is determined by the spin, I_0, of the oriented nucleus, since the 3-J symbol is equal to zero if $\lambda > 2I_0$. The *de*orientation parameter U_λ decreases the degree of orientation of a given level (*i.e.* it is

always ≤ 1) because of m-subshell mixing due to radiations preceding those from the level of interest. For a transition among states I_1 and I_2, and of pure multipolarity L, the deorientation parameters are

$$U_\lambda(I_1 I_2 L) = (-1)^{I_1+I_2+L+\lambda} \hat{I}_1 \hat{I}_2 \begin{Bmatrix} I_1 I_1 \lambda \\ I_2 I_2 L \end{Bmatrix}, \tag{11}$$

where the last term is a Wigner 6-J symbol. If the transition is one of mixed multipolarity, the individual U_λ are weighted according to the intensity of each multipole component, and are given by

$$U(I_1 I_2) = \frac{\sum_L U_\lambda(I_1 I_2 L) \mid \langle I_2 \| L \| I_1 \rangle \mid^2}{\sum_L \mid \langle I_2 \| L \| I_1 \rangle \mid^2}. \tag{12}$$

For a low-lying level the U_λ is a product of all of those from higher-lying levels which populate that level in a cascade. That is, for a cascade of gamma rays from the level I_0 to the level I_i via the levels $I_1 I_2 I_3 \ldots I_n$, the deorientation parameters for the level I_i are

$$U_\lambda(I_0 \ldots I_i) = U_\lambda(I_0 I_1) U_\lambda(I_1 I_2) U_\lambda(I_2 I_3) \ldots U_\lambda(I_n I_i).$$

Q_λ is a geometrical correction factor which corrects the distribution for the finite size of the detector. These are calculated from the geometry of the active region of the Ge crystal, the separation of the crystal from the source, and the absorption cross-sections for photons in the crystal as a function of gamma-ray energy (see [Kra72]). The corrections are generally between about 85 and 95%. Finally, the A_λ is the actual angular distribution coefficient, involving all information about the radiation multipolarities of the transition and the initial and final nuclear spins of levels involved in the transition.

As a final note, the orientation parameters are often written to include a term which accounts for the fraction of ions, f, which are implanted into "good", substitu-

tional lattice sites. During on-line orientation experiments, ions are rather violently implanted into the host lattice. Not all of those ions find themselves in a lattice site within which it will experience the full hyperfine interaction; the orientation parameters (which depend on the field strength B) will then be different for these sites. A simple, two-site model is often used to describe the ensemble, in which the fraction f are assumed to be in "good" lattice sites, and experience the full hyperfine field. The remaining (1-f) ions are assumed to experience no interaction at all, thus remain unoriented. The f is often implied, then, and the B_λ are referred to as the *effective* orientation parameters. Typical values for f are 60-80% [Her77, Her78].

When radiation of only two multipole orders (L and $L'=L+1$) is involved in a transition, the transition is described using the multipole mixing ratio δ, which is defined in terms of the transition matrix elements as

$$\delta(X'L'/XL) = \frac{\langle I_2 \| X'L' \| I_1 \rangle}{\langle I_2 \| XL \| I_1 \rangle}. \tag{13}$$

The magnitude of δ is then given by

$$|\delta(X'L'/XL)| = \left[\frac{T(X'L')}{T(XL)} \right]^{1/2}, \tag{14}$$

where T is the decay probability (intensity) of each component. Because of angular momentum selection rules and the strong energy dependence of transition probabilities [Boh69] (which suppresses higher-order multipoles), generally only electric quadrupole and magnetic dipole radiations are involved in mixed electromagnetic transitions. The mixing ratios discussed throughout this work will therefore be considered to be

$$\delta \equiv \delta(E2/M1). \tag{15}$$

The multipole mixing ratios are related to the angular distribution coefficients via

$$A_\lambda = \frac{F_\lambda(LLI_fI_i) + 2\delta F(LL'I_fI_i) + \delta^2 F_\lambda(L'L'I_fI_i)}{1+\delta^2} \tag{16}$$

where the *F*-coefficients are defined as

$$F_\lambda(LL'I_fI_i) = (-1)^{I_f+I_i+1}\hat{\lambda}\hat{L}\hat{L}'\hat{I}_i\begin{pmatrix} L & L' & \lambda \\ 1 & -1 & 0 \end{pmatrix}\begin{Bmatrix} LL'\lambda \\ I_iI_iI_f \end{Bmatrix}. \tag{17}$$

The last two terms again represent Wigner 3-*J* and 6-*J* symbols. The *F*-coefficients are given in tabular form in [Kra71] for initial spins I_i up to 8 and multipolarities λ up to 3. Finally, for radiation of pure multipolarity the A_λ are equal to the F_λ, and are therefore known exactly. The angular distribution formalism shown above is developed in full detail by [Kra86] and [Ste75].

A frequently used term in the discussion of angular distributions is the *anisotropy*. The anisotropy of radiation from an ensemble of oriented nuclei is defined in terms of the angular distribution as

$$A(\theta) = 1 - \frac{R(\theta)}{R(0°)} = 1 - \frac{W(\theta)}{W(0°)} \tag{18}$$

where $R(\theta)$ is the ratio of cold to warm count rates at angle θ, and $W(\theta)$ is the angular distribution. The anisotropy is most often taken from 0° and 90° measurements, so is referred to as $A(90)$. At "warm" temperatures thermal motion prohibits orientation of the nuclear spins; the radiation is isotropic, and the angular distribution is equal to one (there is no anisotropy).

In order to extract spectroscopic information from measured gamma-ray (or electron) singles intensities, we must relate those intensities to the directional distribution as defined above. The measured γ-ray intensity (averaged over some suitable time) is given in terms of the angular distribution as

$$\frac{dN_\gamma(\theta)}{dt} = \frac{dN_0}{dt} b_\gamma \epsilon_\gamma(\theta)\Omega(\theta)W(\theta) \tag{19}$$

where dN_0/dt is the actual decay (or production) rate of the isotope from which the γ ray of interest is emitted, b_γ and ϵ_γ are respectively the branching ratio and detector efficiency for that gamma ray, and Ω is the solid angle subtended by the detector. Normal operating procedures during NO experiments are to cycle between "cold" and

"warm" temperatures. This serves to normalize the intensities (as will be discussed in the data analysis section, 3.1.5) so that values for the decay rates, branching ratios, and efficiencies are not needed; only intensities need to be measured.

3. Experimental Apparatus and Procedures -^{187}Ir

3.1 Nuclear Orientation of ^{187}Pt

3.1.1 Introduction

The main focus of this work has been to use nuclear orientation as a spectroscopic tool to elucidate the nuclear structure of odd-A Ir isotopes. The central theme has been to measure multipole mixing ratios $\delta(E2/M1)$ of electromagnetic transitions with better accuracy than is possible by other techniques such as conversion electron spectroscopy, and to use those mixing ratios to understand the low-energy structure. The nuclear orientation procedure involves orienting the magnetic moments of the radioactive nuclei being studied in a strong magnetic field. The gamma rays emitted in the decay are then correlated with the axis of orientation, and the anisotropy reflects the multipolarity of the radiation. Spectroscopic properties (nuclear spins, parities, and mixing ratios, for example) are then deduced from the angular distributions.

In order to extract spectroscopic information and to understand the degree of orientation, one must have a thorough knowledge of the decay scheme. Only rather incomplete decay studies had previously been done on the odd-A isotopes in this region, however, so complete coincidence spectroscopy experiments were performed in addition to the nuclear orientation. Coincidence spectroscopy techniques at UNISOR are very well established and many papers have been written describing the procedures. Little mention will therefore be made of the experimental procedures. The Nuclear Orientation Facility, however, is still quite new, so much more attention will be paid to details regarding the techniques used in that part of the study.

The Nuclear Orientation Facility at the Holifield Heavy-Ion Research Facility (HHIRF) at Oak Ridge National Laboratory is part of the University Isotope Separator at Oak Ridge (UNISOR) facility. The UNISOR facility consists of an isotope separator on-line to the HHIRF 25-MV folded tandem electrostatic accelerator, spectro-

scopic counting stations, and a ^{3}He-^{4}He dilution refrigerator. Schematic diagrams of the HHIRF tandem and the isotope separator and Nuclear Orientation Facility (NOF) are shown in Figures 3 & 4. The isotope separator and associated equipment and NOF are described in [Spe81] and [Gir88] respectively.

The NOF at UNISOR was designed with two objectives in mind. The first requirement was for a "top-loading" bottom-access facility. That is, the radioactivity is directed up from underneath the refrigerator for implantation, and the sample holder is removable from above. This provides the ability to change the cold-finger and sample holder relatively quickly (roughly 5 hours) without warming up the cryostat from liquid He temperatures. This feature enables the experimenter to refresh the contaminated sample holders during on-line runs without much loss of precious beam time. The next feature was the unique design of the superconducting magnet, which has large beveled opening ports at 90° in order to permit measurement at the 45° positions. This is presently the only operating refrigerator with the capability to measure at the 45° positions. Including the 45° detectors can sometimes quickly distinguish between the two possible mixing ratio solutions which are found using 0° and 90° measurements alone.

The ^{3}He-^{4}He dilution units, which are commercially available, can also maintain temperatures in the millikelvin range while under large heatloads for long periods of time, making them ideal for the present application. Details concerning ^{3}He-^{4}He dilution refrigerator operating principles can be found in books by [Lou74] and [Bet76] and articles by [Whe71] and [Rad71].

3.1.2 Thermometry

Perhaps the most pervasive issue in nuclear orientation work is that of accurate sample temperature measurement. As has already been illustrated in Equation (8), the degree of nuclear orientation is related directly to the temperature [or, more precisely, to the factor $\exp(m\mu B_z/kTI_0)$]. (*Temperature*, here, refers to the macroscopic temperature of the environment into which the radioactive atom is introduced.) A high

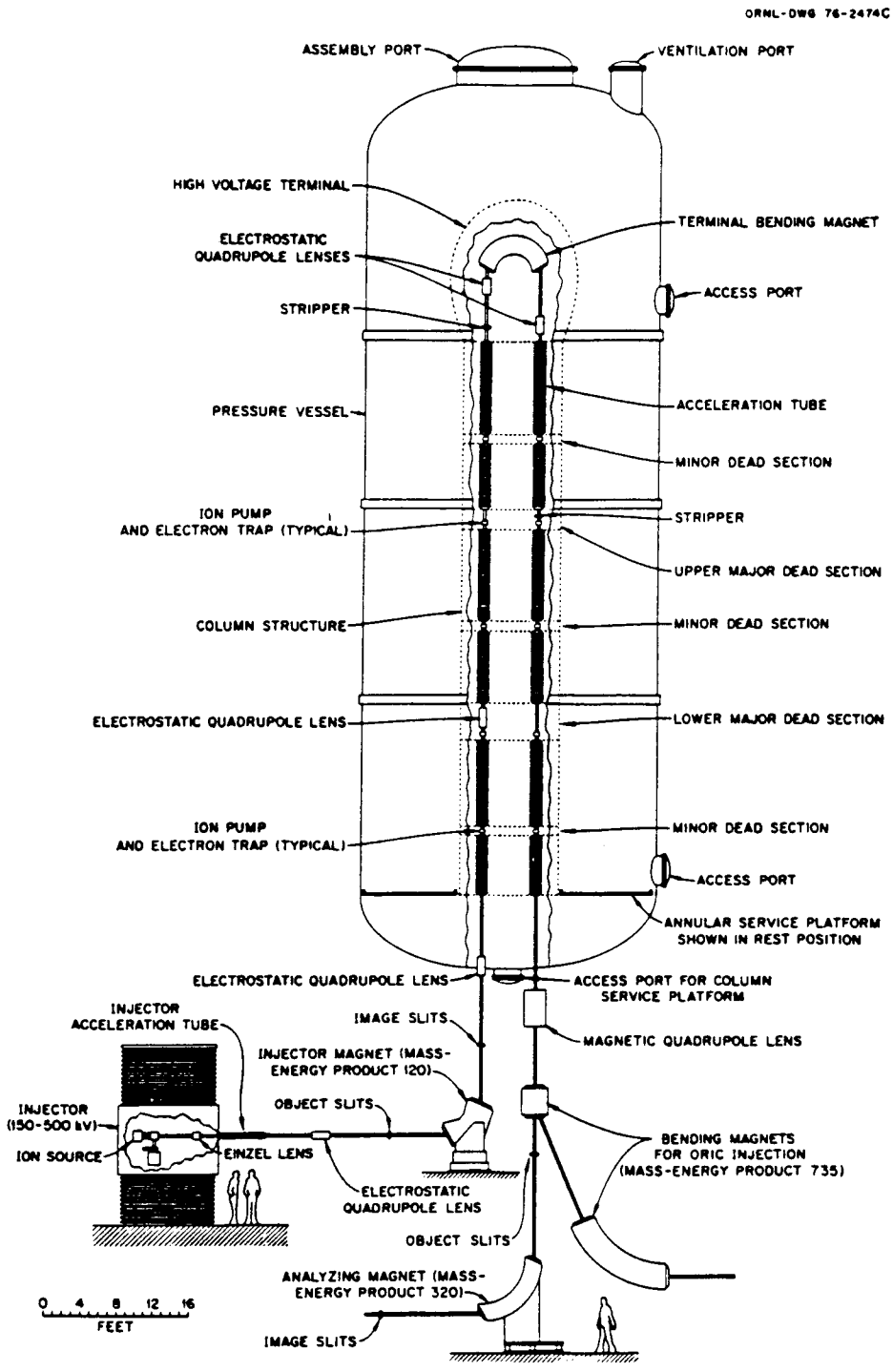

Figure 3 Sectional diagram of the HHIRF folded tandem accelerator.

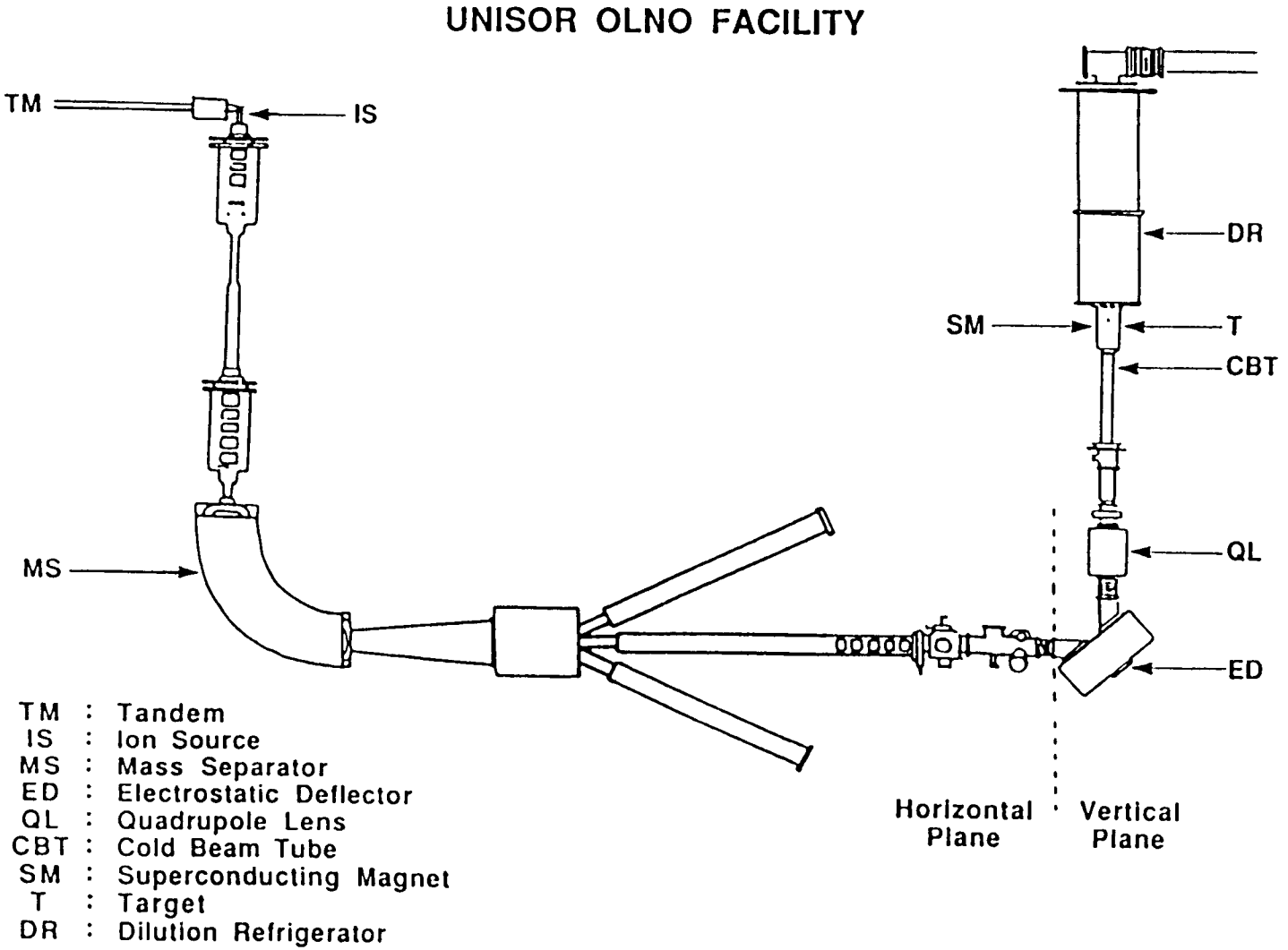

Figure 4 Schematic diagram of the UNISOR facility.

degree of orientation can therefore be reached only for very high field strengths and very low temperatures. Implantation of the sample under study into a ferromagnetic lattice can supply hyperfine fields of several hundreds of Tesla for certain elements (see Figure 5), and ^{3}He-^{4}He dilution refrigerators can maintain temperatures as low as a few millikelvin for long periods of time (weeks).

For normalization purposes Nuclear Orientation (NO) experiments are generally performed by cycling the temperature (in roughly two-hour cycles) between the lowest attainable (base) temperature and about 500 mK (at which temperature count rates are isotropic). Sample temperatures must be monitored continuously throughout the experiment in order to enable "summing" of data taken at similar temperatures and to facilitate accurate analysis of the data. A thermometer commonly used for NO experiments is ^{57}Co in Fe, and this was used for all of the present work.

Preparation of the source was as follows: a small amount of ^{57}Co activity was dissolved in HCl, dried on the surface of an Fe foil of thickness 0.1 mm and approximate diameter 1 cm, and then diffused into the foil at 850 K for 12 hours. Consideration was given to the amount of activity in the foil, as it is desirable to have only enough activity to provide good counting statistics at all angles and temperatures (keeping in mind the detector efficiencies, absorption in the cryostat, and the anisotropy). Spectra collected during cold cycles at the 0° positions, for example, require around 10,000 counts within a 10-minute counting period, as the angular distribution is a minimum there for cold cycles -with only about 20% of the counts that would be measured at high temperatures. Conversely, if thermometer-peak count rates are too high, there is difficulty fitting the peak due to Compton tailing. Of course, the count rates can be optimized somewhat before the run by simply changing the source-detector distance.

Following the diffusion of Co activity into the foil, the Fe foil was soldered onto the copper cold-finger of the ^{3}He-^{4}He dilution refrigerator at the UNISOR On-line Nuclear Orientation Facility [Gir88] and highly polished to remove residual activity and prepare the surface for implantation. The cold-finger assembly was then "top-loaded" into the operating position in the dilution refrigerator. The foil was

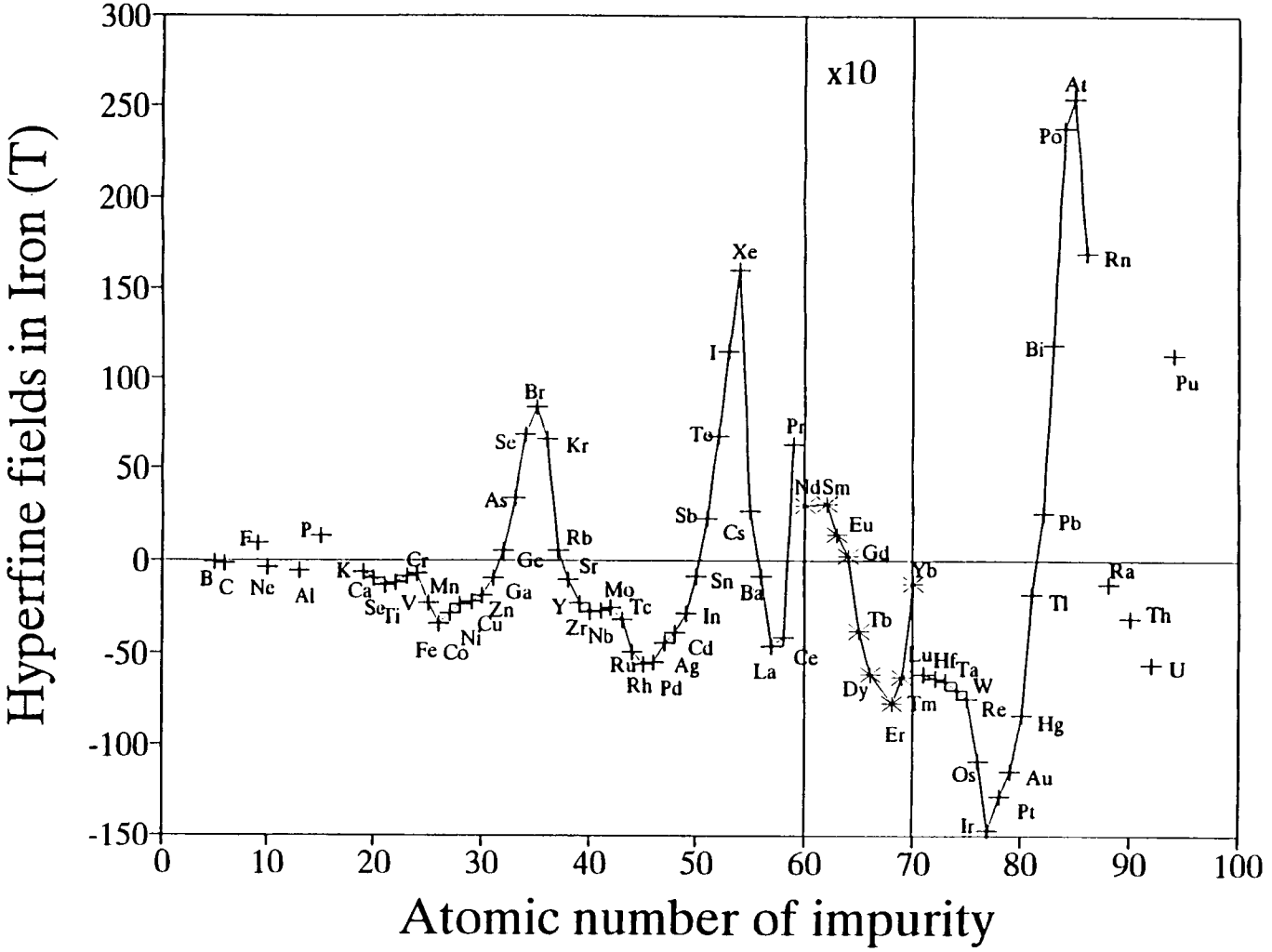

Figure 5 Hyperfine-fields for various elements implanted in Fe.

polarized by a 0.6 T external field provided by a superconducting magnet inside the cryostat, which provided a hyperfine-field of around 128 T for the orientation of 2.35 h ^{187}Pt. Angular distributions of the ^{57}Co radiation were used as an absolute measure of the temperature of the Fe host into which the activity was implanted. The decay-scheme of ^{57}Co is a simple one, with almost all of the intensity depopulating a single level. Two gamma rays in the decay of ^{57}Co can be used to determine sample temperatures over a range of about 3-90 mK [Mar86], one at 122.1 keV and the other at 136.5 keV (which, although it has lower intensity, has a much larger anisotropy). Interference from the Pt decay prevented the use of the 122-keV line as a temperature monitor, but enough activity was diffused into the foil to provide good statistics from the 136-keV line. This line was monitored continuously throughout the experiment, allowing spectra which were collected at similar temperatures to be summed into groups of roughly two hours. Count rates from the 136-keV line were also used to correct the spectra for pulse pileup as will be discussed later. A plot of count rates for the 136-keV line is shown in Figure 6 for one of the 0° detectors, indicating the large anisotropy, and therefore its usefulness as a thermometer.

Finally, since the angular distribution of this line is so well known [Mar86], it was also used to determine the precise locations of the detectors relative to the axis of the applied magnetic field. This procedure will be discussed in the data analysis section.

3.1.3 Isotope Production and Measurement

A self-supporting ^{176}Hf target was bombarded by 125 MeV ^{16}O atoms from the ORNL EN-Tandem. The resulting Hg activity was mass separated and implanted at 50 keV into the Fe foil for orientation. On-line orientation of ^{187}Hg was performed but will not be discussed here. To illustrate the choice of reaction, the decay sequence is shown in Figure 7.

Projectile type and energy were chosen so as to maximize ^{187}Hg production for the on-line experiment, while the short half-lives of both ^{187}Hg and ^{187}Au permitted

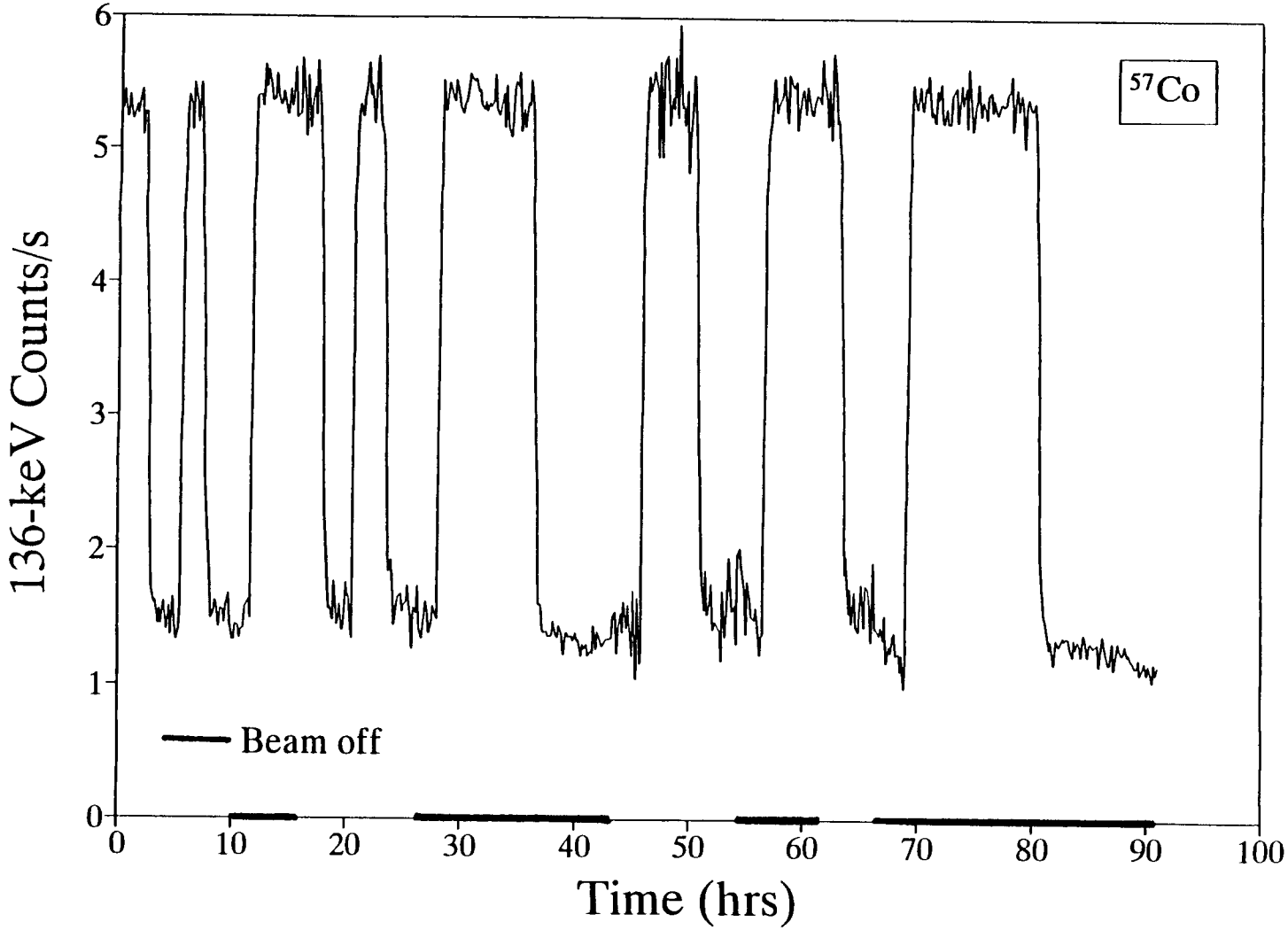

Figure 6 Count-rates for the 136-keV ^{57}Co thermometer line at 0°. "Warm" cycles have higher rates at this angle.

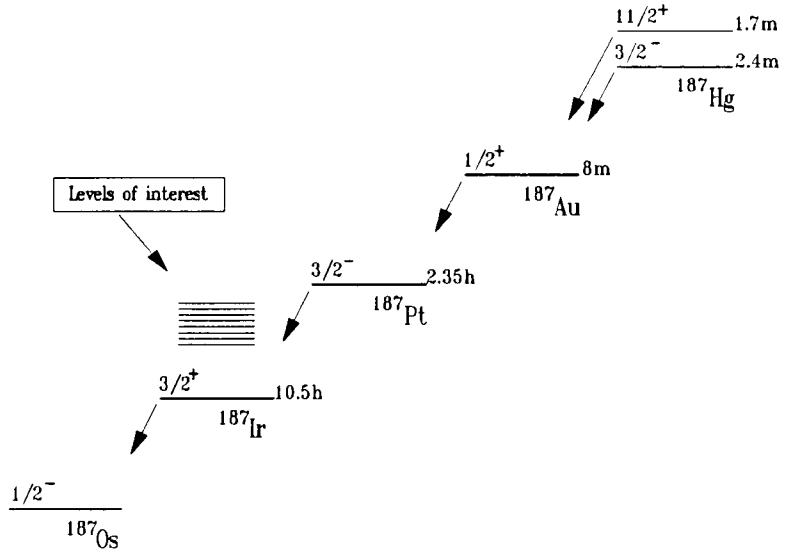

Figure 7 Beta-decay chain following ^{187}Hg production.

subsequent off-line measurements of ^{187}Pt decay without the interference of those activities. A configuration of 7 coaxial detectors (4 high purity Ge and 3 Ge(Li), with average volumes of about 54 cm^3 and a minimum resolution of 1.75 keV FWHM at 1332 keV) was used to collect gamma-ray singles events. The detectors were arranged at 45 degree intervals along the axis of the orienting magnetic field, approximately 15 cm from the source. A schematic diagram of the experimental setup is shown in Figure 8. Three detectors placed at the 45° positions facilitated extraction of fourth-order coefficients in the angular distributions of radiation from the oriented nuclei (see data analysis section). Data were monitored on-line using a Canberra ND9900 data acquisition system connected to a Digital Equipment Corporation MicroVAX II. The ND9900 module includes a graphical interface which permits continuous pulse-height analysis of each detector. The individual spectra were written periodically to disk and then transferred to tape for subsequent analysis. 8192-channel spectra were collected for more than 540 ten-minute cycles. A summed-total spectrum taken from warm cycles is shown in Figure 9, which illustrates the positions of the ^{57}Co thermometer lines.

The refrigerator was operated in the semi-on-line mode, *i.e.*, collecting activity

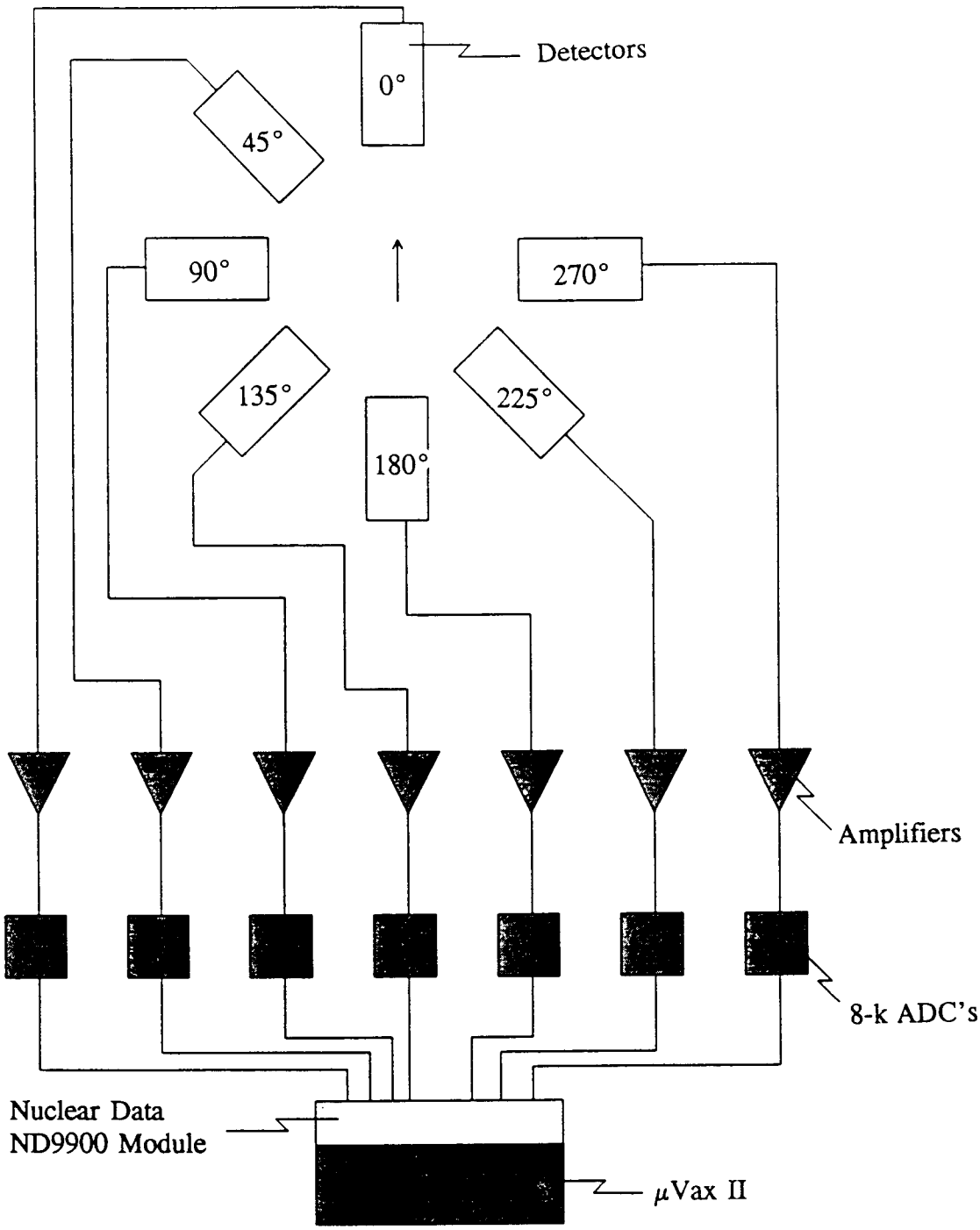

Figure 8 Schematic diagram of electronics setup for NO experiments.

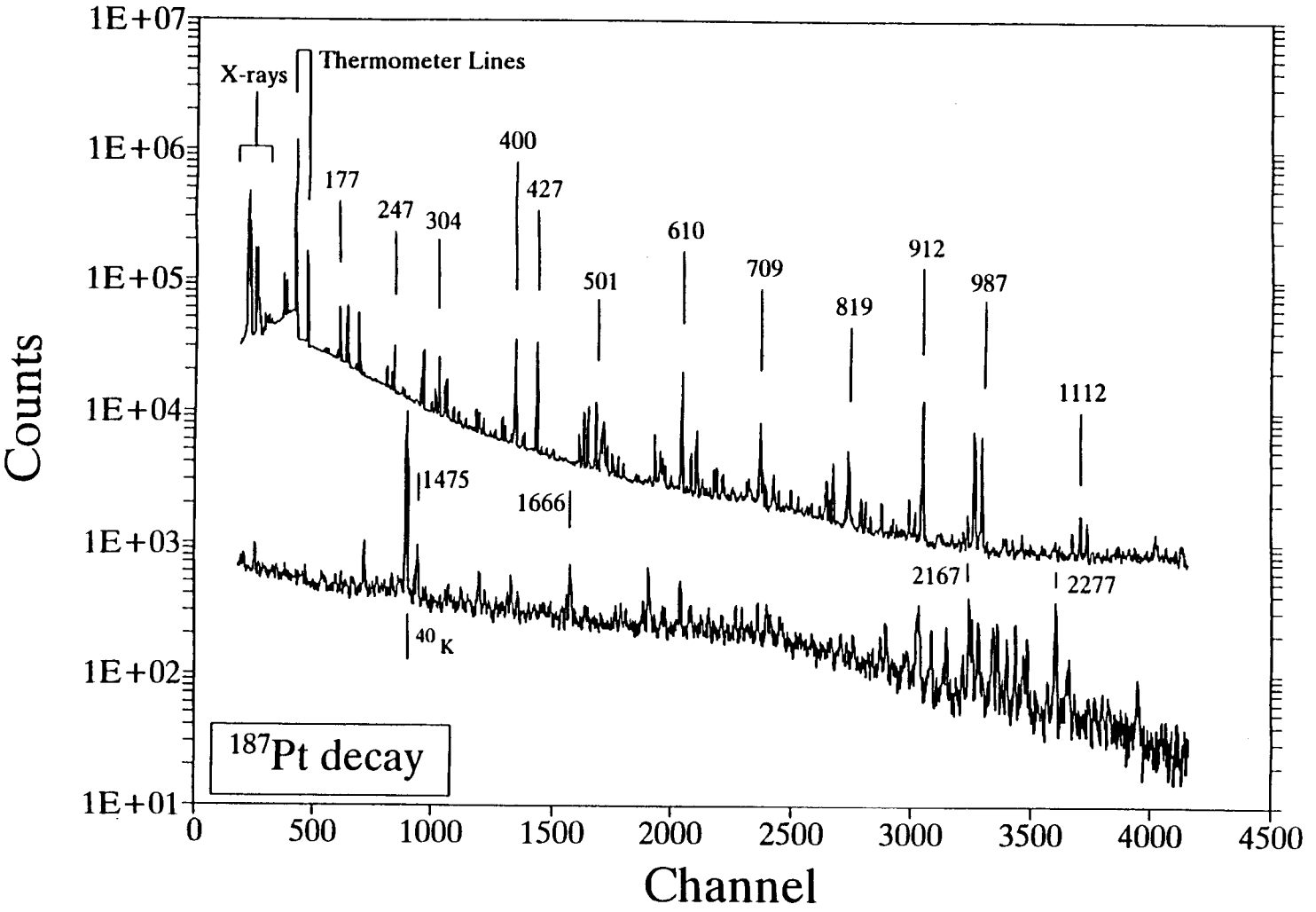

Figure 9 Summed "warm" ^{187}Pt spectrum from NO run. Note the high intensities near 2 MeV.

for several hours then removing the beam and monitoring daughter activity. As is evident from the decay sequence (Figure 7), the short-lived Hg and Au activities decay quickly after removing the beam, leaving only the Ir and Os daughters. The long decay periods at the end of the beam-off cycles removed all but the long-lived Os activity. The second beam-on period then began with a relatively "clean" Fe foil. The refrigerator was also cycled between base temperature and 500 mK in order to permit normalization of "cold" rates to the "warm" (isotropic) count rates (see data analysis section). The beam-on/beam-off cycle was repeated two times. An average ^{187}Hg implantation rate of about 1.5×10^5 atoms/s was achieved during beam-on cycles, and a base temperature of 6.8(1) mK was maintained with minimal beam-heating of the cold-finger throughout the cold, beam-on cycles, as can be seen in Figure 6.

3.1.4 Pulse Pileup Corrections

The loss of counts in a counting system is a persistent problem in spectroscopic experiments, and must be accounted for if absolute measurements are needed or if rates from different detectors are compared. Various effects are responsible for loss of counts in a peak: random and coincidence summing (see [Deb79] and references therein), whereby events arrive in the (Ge) detector simultaneously, resulting in literal summing of the energies (these two events are then removed from their respective full-energy peaks, and a new sum-peak results); escapes, in which 511-keV γ-rays due to lattice electrons annihilating positrons from e^+e^- pairs produced in the crystal by a high-energy gamma ray or the incident gamma ray itself exits before depositing the full energy; and finally, the so-called pileup events.

Pileup events are an artifact of the finite resolving time of the entire detecting system, causing events to "pile up" at one stage of the process. The most simple spectroscopic system consists, first of all, of a germanium crystal, a preamplifier, various cables, an amplifier, and finally an analog-to-digital converter (ADC) and multi-channel analyzer which stores the digitized events. Only the crystal and the

ADC have any appreciable "recovery" time following an event, but by far, the slowest process is that of conversion. Typical analog to digital conversion rates are only 25-50,000 s^{-1}. Events which enter the system during the window in which another is being converted, then, are not counted, and are lost from the spectrum. While there is no way to know exactly how many counts have been lost, it is trivial to count the time for which the ADC was busy converting. This dead-time can then be used along with a statistical model, as given in [Leo87], for example, to estimate the true count rates.

Spectra were corrected for pulse pileup using a modified "two source technique" [Nuc90]. The 271-d ^{57}Co thermometer served as an essentially constant-rate source throughout the course of the experiment, while fluctuations in beam rate provided a variable-rate source, slowly changing dead-times in the detector/-amplifier/ADC configurations (D/A/ADC). The change in the count-rates of the "constant" source then reflects the loss due to pileup during the ADC dead-time. Dead-times ranged from 2% during the decay periods to almost 25% with beam on target. For dead-times larger than about 5%, it is imperative that one uses a higher-order correction for pulse pileup, rather than a simple, linear correction (multiplying by the ratio of real- to live-times). This is especially true whenever rates from different detectors (with different dead-times) are compared, as in NO experiments. The pulse-pileup corrected rates are given in terms of the measured areas by

$$Rate = \frac{Area}{LT} e^{PPC(RT/LT-1)} \tag{20}$$

where (the positive) *PPC* is the pulse pileup constant for each D/A/ADC configuration, and *RT* and *LT* are the real- and live-times for the counting system. Again, since most of the intrinsic dead-time is in the conversion process, ADC live-times (which were stored in channel 0 of each spectrum) were used. A weighted least-squares regression was done to the natural log of the measured rates of the thermometer line (taken from warm cycles, when rates are isotropic) as a function of (*RT*/*LT*-1), giving the *PPC* and corrected rate. Count rates for each 10-minute cycle

are shown in Figure 10 for the 136-keV line, showing both the pileup-corrected and uncorrected rates for one of the 90° detectors, where high efficiency (thus high rates) resulted in large dead-times. Live-time corrections alone cannot correct for such high dead-times. The data were divided into 8 cold and 8 warm cycles based upon these rates, and spectra taken during those cycles were corrected for gain-shift and then summed. Uncertainties from counting statistics were below the 1% level, permitting accurate determination of the *PPC*'s for each angle. A polar plot of the angular distribution of the 136-keV thermometer line is shown in Figure 11, from which the base temperature of 6.8(1) mK was extracted.

3.1.5 Data Analysis

Following the necessary pileup corrections, gamma-ray intensities were found for each of the 16 summed spectra, and related to the angular distribution. The peak-fitting routine SAMPO [Rou69] was used to fit all gamma ray and electron spectra. SAMPO fits each peak as a gaussian with exponential high- and low-energy tails. The technique used to extract coefficients of the Legendre polynomials involves the use of all possible combinations of angles in order to minimize systematic uncertainty. The first step is to take ratios of cold to warm rates in order to normalize the data and remove all terms in Equation (19) except for the angular distribution, $W(\theta)$ (which, for high temperatures, is equal to 1). We then define the ratio $R(\theta)$ as

$$R(\theta) = \frac{\dot{N}_c(\theta)}{\dot{N}_w(\theta)} = W(\theta) \tag{21}$$

where $\dot{N}_{c/w}(\theta)$ stands for the pileup-corrected rates for *cold/warm* temperatures. The ratios for angles of 45°, 90°, 135°, and 270° are then divided by that of 0°. The same ratios are taken for 180°, giving 8 independent combinations. The angular distribution is invariant to reflections along the symmetry axis as well as axially symmetric; that is to say that $W(0°) = W(180°)$ and $W(45°) = W(135°)$, *etc.* We therefore normally refer to detectors at 45, 135, 225, 315° as *the* 45° detectors, while

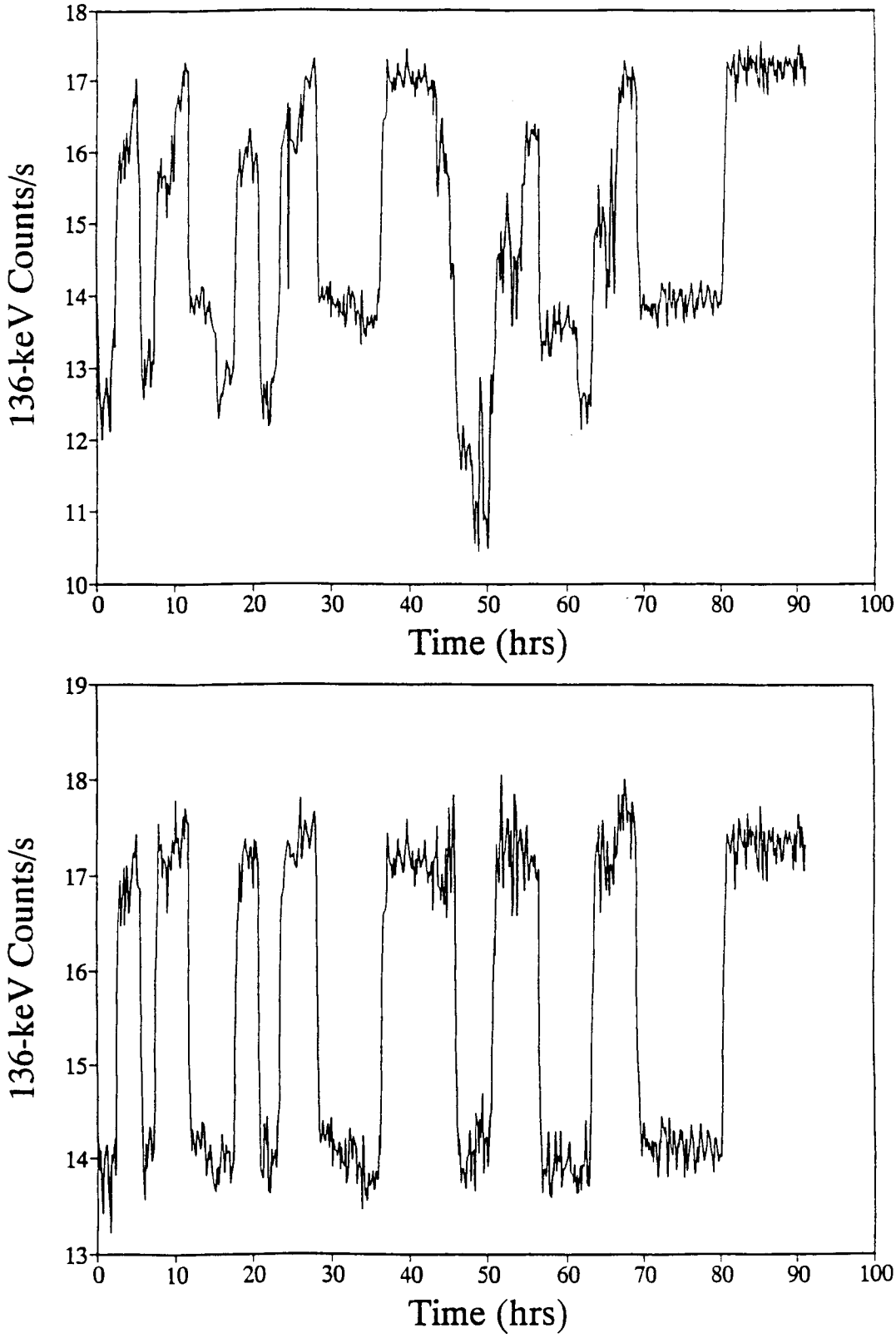

Figure 10 ^{57}Co-thermometer line illustrating a large pileup correction for 90° detector. Upper plot shows uncorrected rates while the lower has been pileup corrected.

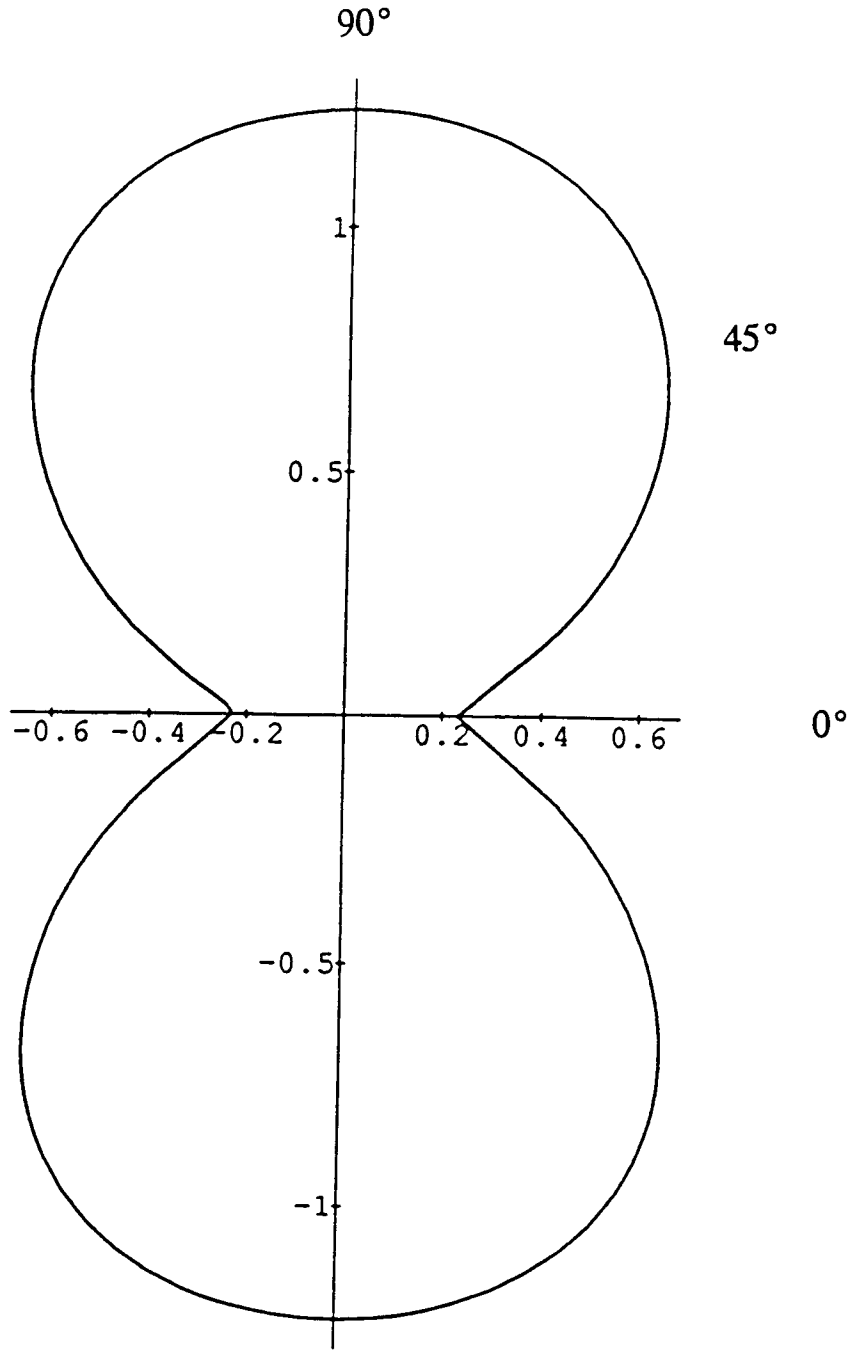

Figure 11 Polar plot of 136-keV radiation. The base temperature was found to be 6.8(1) mK based on this distribution.

those at 0 and 180° or 90 and 270° are *the* 0° and 90° detectors respectively. Using the definitions of $W(\theta)$ and a_λ as in Equation (6), we then write

$$\frac{R(45°)}{R(0°)} = \frac{1+\frac{1}{4}a_2Q_2(45°)-\frac{13}{32}a_4Q_4(45°)}{1+a_2Q_2(0°)+a_4Q_4(0°)} \tag{22}$$

and

$$\frac{R(90°)}{R(0°)} = \frac{1-\frac{1}{2}a_2Q_2(90°)+\frac{3}{8}a_4Q_4(90°)}{1+a_2Q_2(0°)+a_4Q_4(0°)}, \tag{23}$$

giving two unknown quantities, a_2 and a_4, in two equations. The redundancy in angle serves to decrease the statistical uncertainty, and using diametrically opposed detectors tends to average over any slight changes of the source position on the cold-finger during the implantation cycles. The detailed solutions to the a_λ are given in Appendix A, along with the 6-detector analysis scheme.

As was previously mentioned, the precise detector positions are also found using the above procedure for the angular distribution of the ^{57}Co lines. The thermometer-line intensity is found for each angle, normalized to warm data as above, and a_λ is found. The A_λ and U_λ are known precisely for the ^{57}Co transitions [Mar86], and an analytical expression for B_λ (the Brillouin function [Kra86]) is employed. The angular distributions $W(\theta)$ are then calculated for a range of angles $0\pm1\pm2°$, $45\pm1\pm2°$, and $90\pm1\pm2°$, and compared to the experimental values. When written in tabular form, it is a simple matter to "narrow in" on the detector positions within about 0.5°. These positions are then used in all subsequent calculations, and the base temperature is determined using the new positions.

Coefficients a_λ were extracted for over 50 lines in ^{187}Ir, and are compiled in Table 3. Values shown in the table have already been corrected for the Q_λ, so that $a_\lambda = U_\lambda B_\lambda A_\lambda$. The distributions were consistent with the $I_0(^{187}\mathrm{Pt}_{gs}) = 3/2$; *i.e.*, coefficients of the fourth-order Legendre polynomials (which are particularly sensitive to 45°) were all consistent with zero. This condition must be met since the B_λ are

Table 3 ^{187}Ir coefficients of the Legendre polynomials in $W(\theta)$. Values have already been corrected for Q_λ, so that $a_\lambda = U_\lambda B_\lambda A_\lambda$. Because of low rates in one of the 45° detectors, a_2 values accompanied by "#" were analyzed assuming $a_4 = 0$. Unresolved doublets are denoted by an asterisk "*".

E(keV)	a_2	a_4	E(keV)	a_2	a_4
83.18	0.025(12)	#	551.64	0.22(8)	0.09(13)
91.60	-0.187(31)	#	622.19	0.039(15)	-0.020(19)
97.67	-0.11(7)	#	629.27	-0.138(7)	-0.010(10)
106.55	0.006(4)	-0.006(5)	706.01	0.26(6)	0.01(9)
110.17	0.110(5)	-0.006(6)	*708.88	0.068(6)	-0.001(8)
174.99	0.201(23)	0.003(35)	712.45	0.360(21)	#
189.61	0.091(18)	-0.002(26)	789.95	0.014(22)	0.016(31)
198.99	0.09(5)	0.05(7)	792.13	0.083(14)	-0.037(22)
205.16	-0.112(23)	0.014(28)	795.74	-0.164(24)	0.047(33)
*244.79	0.123(13)	-0.020(20)	816.06	0.141(38)	-0.05(6)
247.60	0.090(6)	-0.003(8)	819.13	0.199(8)	-0.009(12)
281.99	-0.023(11)	-0.004(14)	833.00	-0.031(49)	0.01(7)
*284.51	0.043(9)	-0.018(10)	895.10	0.016(30)	-0.064(32)
304.67	-0.035(5)	0.002(7)	1475.19	0.020(18)	0.011(27)
311.68	0.160(9)	0.035(15)	1552.91	0.030(27)	-0.014(38)
329.70	-0.054(22)	0.007(31)	1665.87	0.026(20)	0.042(25)
332.76	-0.19(5)	0.06(7)	1805.00	-0.007(21)	0.035(29)
361.09	0.127(18)	0.022(28)	2104.41	-0.188(27)	#
376.42	0.116(37)	0.05(6)	2119.41	-0.074(30)	0.059(40)
388.61	0.022(19)	0.046(30)	2167.04	0.060(18)	-0.073(26)
410.03	0.02(5)	#	2171.25	-0.062(25)	0.044(35)
480.33	-0.019(12)	0.021(19)	2178.89	-0.125(23)	0.019(31)
483.73	-0.27(8)	#	2197.63	-0.183(31)	0.022(37)
486.27	-0.035(7)	-0.001(17)	2202.86	-0.128(27)	#
499.09	-0.123(48)	#	2214.83	-0.003(32)	0.003(47)
504.24	-0.11(5)	#	2277.24	-0.035(17)	0.027(23)
529.48	-0.120(22)	-0.021(32)	2291.22	-0.044(47)	0.045(75)
536.33	0.002(29)	-0.016(39)	2294.50	-0.140(41)	0.012(61)

identically zero for $\lambda > 2I_0$. Extraction of these fourth-order terms provided the first test of the UNISOR NOF, which was designed specifically to enable measurement at the 45° positions. It was therefore essential that any systematics associated with scattering or shadowing from the magnet at these angles be identified. From the list of coefficients shown in Table 3, it is evident that there are no spurious effects associated with measurements at those positions.

Mixing ratios for transitions in ^{187}Ir (or their signs) were determined using the distribution coefficients. In only a few cases were the mixing ratios determined directly from NO data, as there are very few transitions in ^{187}Ir with which the relative method (described below) can be used for gamma rays in competition with pure $E2$ transitions. As the decay scheme is quite complex, a top-down analysis (whereby the U_λ are found for each subsequent level in the decay) is also not possible, and therefore the individual U_λ and B_λ are not known. It is not possible, then, to calculate mixing ratios independently from the a_2's. For mixing ratios which are known from other means (conversion electrons or coulomb excitation, for instance) the signs are often easily determined using the a_λ. In many cases the sign of A_2 (for a given δ) is clearly either positive or negative. The sign of the mixing ratio is then determined by the sign of the a_2.

The *relative method* can also sometimes be used to calculate mixing ratios directly. When the a_λ are known for two different transitions depopulating the same level, and one of those is a pure electric quadrupole transition, the ratio of coefficients is simply

$$\frac{a_2(\gamma_1)}{a_2(\gamma_2)} = \frac{A_2(\gamma_1)}{A_2(\gamma_2)}. \qquad (24)$$

Since A_2 is known exactly for pure $E2$ transitions, the other is then simply derived.

3.1.6 Doublets

Complete analysis of the orientation data was severely hindered by the large

number of doublets in the spectrum. There are several very closely spaced lines in ^{187}Ir, some of which were resolvable as multiplets, but not well enough to find their angular distributions. Only very good knowledge of the branching ratios would facilitate extraction of the angular distributions of these complicated lines. The buildup of daughter activity in the spectrum also contributed to the doublet problem, as many of the doublets are mixed transitions with both Ir and Os lines. Over a dozen of these further complicated analysis of several key transitions. Again it is possible to analyze the mixed doublets in certain circumstances if both the relative activities and branching ratios, *i.e.*, the absolute branching ratios are known. The pulse-pileup corrected rates for a very closely spaced doublet (fit as a singlet) can be written as the sum of individual rates, *i.e.*,

$$\dot{N}_\gamma = \dot{N}_{\gamma 1} + \dot{N}_{\gamma 2}. \tag{25}$$

Then for gamma-rays from the same isotope

$$\dot{N}_\gamma(\theta) = \dot{N}_0 \epsilon_\gamma(\theta) \Omega_\gamma(\theta) \{ b_{\gamma 1} W_{\gamma 1}(\theta) + b_{\gamma 2} W_{\gamma 2}(\theta) \}, \tag{26}$$

while for lines from different isotopes

$$\dot{N}_\gamma(\theta) = \epsilon_\gamma(\theta) \Omega_\gamma(\theta) \{ \dot{N}_{01} b_{\gamma 1} W_{\gamma 1}(\theta) + \dot{N}_{02} b_{\gamma 2} W_{\gamma 2}(\theta) \}. \tag{27}$$

Taking ratios of cold to warm rates and using all combinations of angles again allows one to solve a system of equations for the individual angular distributions.

Two similar techniques were used in an attempt to analyze the doublets using spectra taken at the end of the decay period. Following the long decay periods, only Os peaks remained in the spectra. It was possible, then, to extract angular distribution coefficients for those peaks (which were members of mixed doublets) from one cold/warm cycle. Knowing the angular distribution of the Os line, the Ir member of the doublet could then be analyzed using the approach shown below. Another technique was to use only the two cold cycles at the extreme end of the decay period. Normalization was accomplished by taking ratios of rates from different detectors during the isotropic cycles. The only remaining terms are the products of efficiency

and solid angle, $\epsilon_i\Omega_i/\epsilon_j\Omega_j$, where the subscripts refer to different angles. These ratios were found for all combinations of angles for the energies of interest.

Following an intensive effort to apply these techniques to the ^{187}Pt decay, it was decided that the results were too inconclusive. The largest effort was put into analysis of the mixed triplet near 187 keV, since the Ir line at 186.3 keV would be critical to the analysis of an entire cascade sequence (yielding the orientation parameters). The two closely-spaced lines in Ir (at 186.3 and 187.6, whose branching ratios were accurately known following the spectroscopy run) are complicated by another strong line at 187.4 keV in Os. The Os line was found to have an a_2 coefficient of

$$a_2 = \text{-0.064(19)} \quad \text{from one c/w cycle,}$$
$$a_2 = \text{-0.047(20)} \quad \text{from ratios of } \epsilon\Omega.$$

The Ir line at 187.6 keV is also known to depopulate a level with $I=1/2$, and so has no anisotropy. While this should make analysis of the angular distribution of the 186.3 keV line quite easy, the angular distribution of the triplet (fit as a singlet) has a very small magnitude;

$$a_2(187)_{\text{total}} = \text{-0.037(10)}.$$

With such a small distribution coefficient and such large propagated uncertainties, no conclusions could be drawn about the 186.3 keV anisotropy. Several other attempts were made at other doublets, but similar problems occurred for each. The technique is mentioned here only because a great deal of effort was expended on it, and it is believed that the technique *is* valuable given the proper circumstances. We have found no other reference to any work done on the problem of resolving doublets in nuclear orientation work.

3.2 Spectroscopy of ^{187}Ir

3.2.1 Experimental Procedures

Previous ^{187}Pt decay studies had been done at ISOLDE by Schuck *et al.* [Sch73]. While their low-energy internal conversion data were very complete, coincidence data were somewhat lacking, and the decay scheme was left quite incomplete. Many strong lines were unplaced, for example, and no transitions were observed above 1.3 MeV. It became apparent from our work that there was a considerable amount of unassigned gamma-ray intensity (with E $\sim$ 2 MeV) feeding the low-lying states. The previously existing decay scheme [Fir91] and gamma-ray spectrum from the ISOLDE work are shown in Figures 12 and 13. As was mentioned earlier, the large number of doublets also complicated analysis of the NO data, making it necessary to measure carefully the branching ratios for some of these lines in order to find their angular distributions (thus their mixing ratios).

To provide the information necessary to analyze the NO data, a spectroscopy run was performed in which 110 MeV ^{12}C atoms produced in the ORNL EN-Tandem were used to create iridium via the reaction ^{181}Ta(^{12}C,6n)^{187}Au. ^{187}Au was produced at a rate greater than 5×10^5 atoms/s for the duration of the run. The mass-separated activity was collected on an aluminized Mylar tape and moved on to the spectroscopy stations *via* a tape transport system [Mle81]. Two counting stations were used to collect multiscaled gamma-ray and electron singles and γ-γ and γ-e coincidences. The first station used two high efficiency coaxial germanium detectors in a 90° geometry (resolution $\leq$ 1.8 keV FWHM at 1333 keV) and a cooled Si(Li) electron detector. The second was set up with one Ge and another cooled electron detector. A schematic representation of a typical coincidence spectroscopy configuration is shown in Figure 14, in which multiscaled singles events and γ-e and γ-γ coincidences could be observed. One-hour beam on/off cycles were used to collect the activity, allow the Au to decay away, and move the sample on to the next collecting station. The relatively short (8.4 m) half-life of ^{187}Au and short (1 hour) counting periods

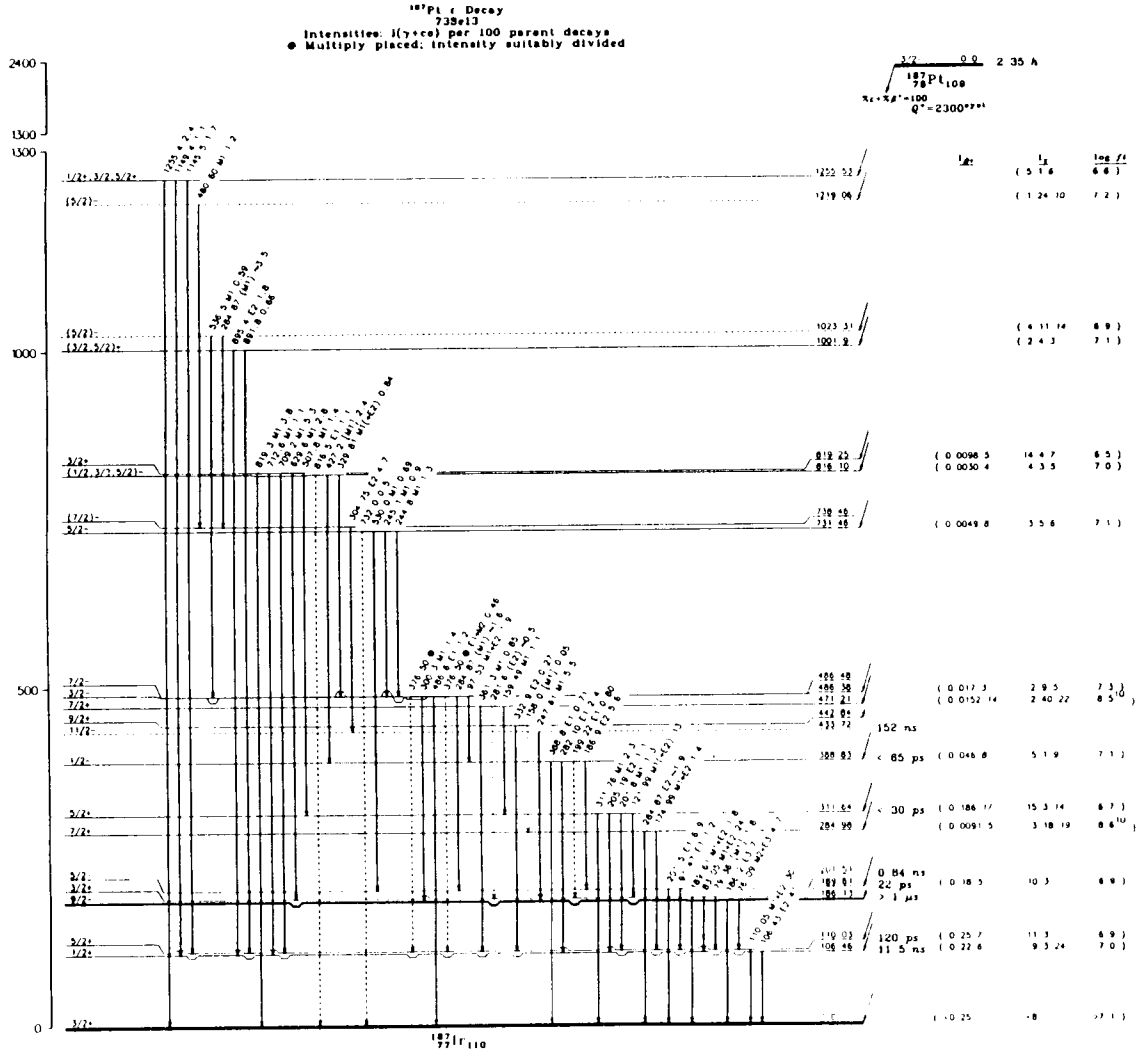

Figure 12 ^{187}Ir decay scheme based on ISOLDE work [Sch73] (from [Fir91]).

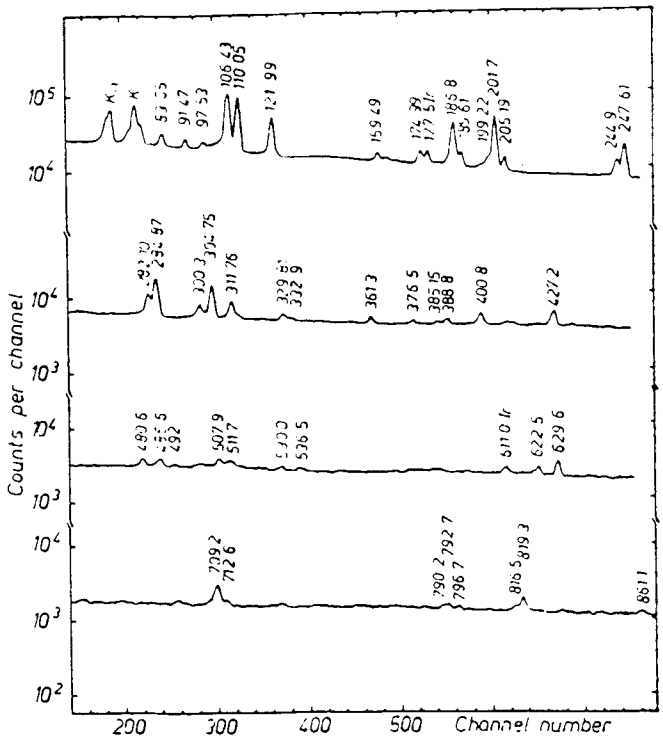

Figure 13 Gamma-ray singles spectrum of ^{187}Ir taken from [Sch73].

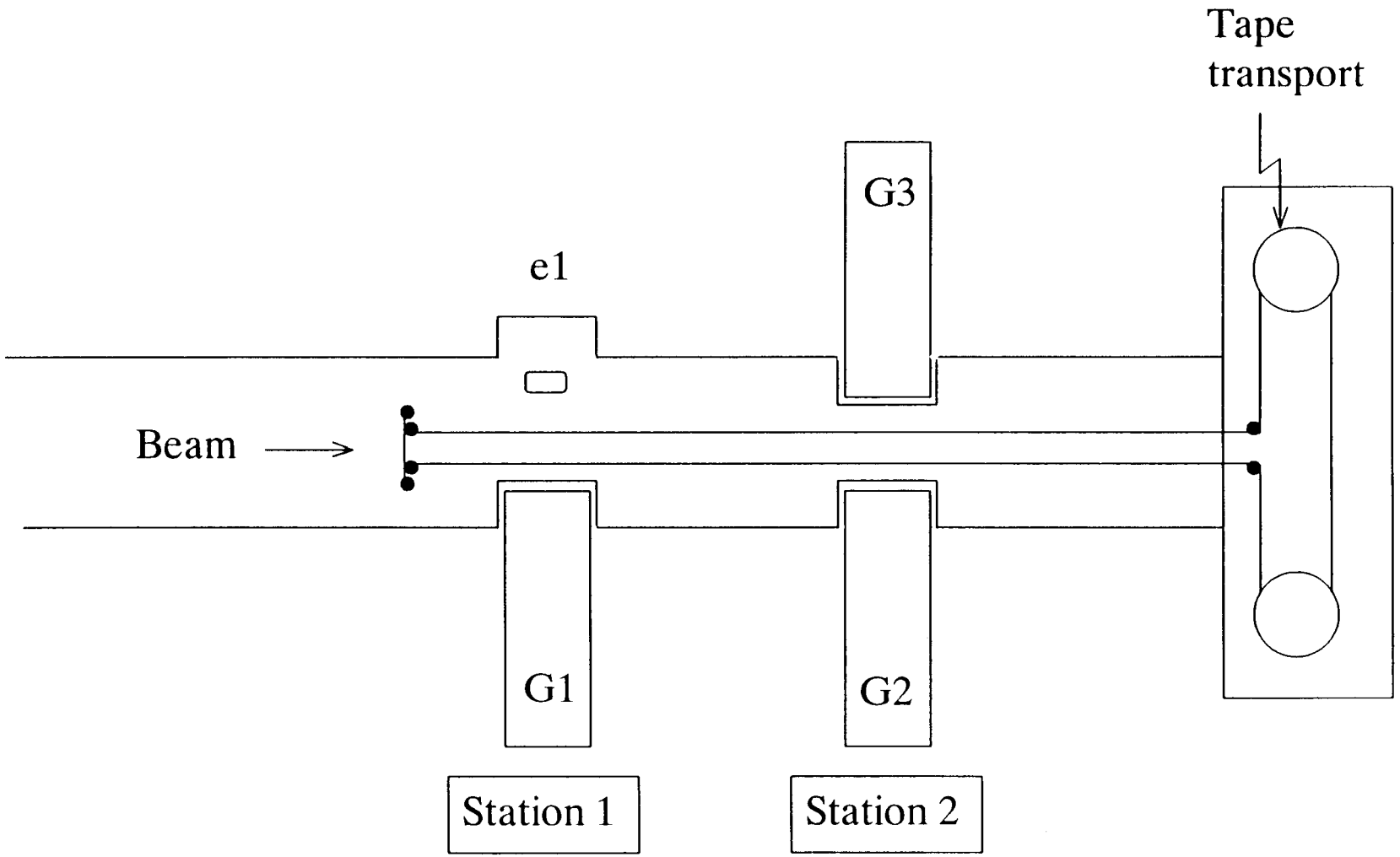

Figure 14 Schematic diagram of typical coincidence spectroscopy setup at UNISOR.

facilitated measurement without interference from parent or daughter activities. Gamma-ray and electron singles spectra from the spectroscopy run are shown in Figures 15 and 16.

Transitions in ^{187}Ir were identified by half-life analysis of multiscaled time-planes. Each of the lines added to the low-energy region, as well as those above 1.3 MeV, were identified in this manner. Coincidence data also helped to identify some of those lines and strengthen their inclusion as ^{187}Ir transitions. All gamma-ray and electron intensities reported here represent fits of summed, multiscaled singles spectra taken during the spectroscopy run. Conversion coefficients, α, were determined from those intensities, and mixing ratios were calculated using theoretical conversion values (interpolated through high-order fits of values from [Ros78]) in the relation

$$\delta^2 = -\frac{\alpha_{exp} - \alpha_{M1_{th}}}{\alpha_{exp} - \alpha_{E2_{th}}}, \tag{28}$$

which is derived from the definitions of δ and α in terms of the intensities T as

$$\delta^2 = \frac{T(E2)}{T(M1)}, \quad T_\gamma = T(E2) + T(M1), \quad \textit{and} \quad \alpha = \frac{T_e}{T_\gamma}. \tag{29}$$

All of the signs of mixing ratios were determined from angular distribution coefficients. (Mixing ratios are compiled in Table 9.) Conversion coefficients are shown in Table 4 for transitions in ^{187}Ir up to 2.2 MeV. Resolution of the Si(Li) electron detectors is far inferior to that of the spectrometer used by Schuck *et al.* [Sch73], and many of the low-energy lines are unresolved, but the much higher efficiency of the Si(Li) detector permitted measurement of many more electron lines. Our data agree well with their results, however, and the high statistics permitted extraction of conversion lines for even the high-energy transitions. The combined set of NO and spectroscopy data was used to produce the new decay scheme shown in Figure 17. All level placements as shown in Table 5 were made using γ-γ coincidence data, which are shown in Table 6. Angular distributions from nuclear orientation were used to strengthen or clarify spin-parity assignments as well as placements.

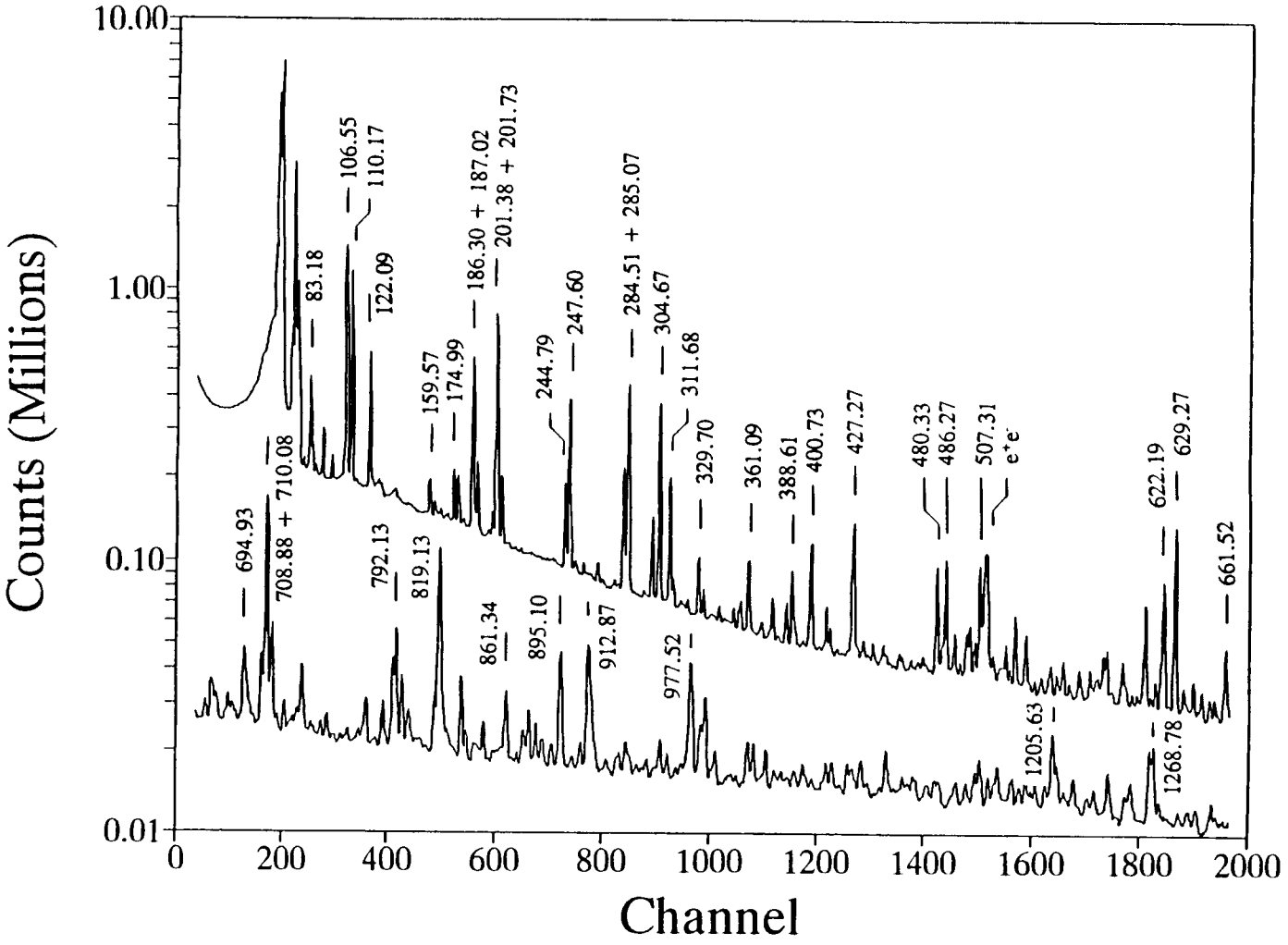

Figure 15a Low-energy region of ^{187}Ir gamma-ray singles spectrum.

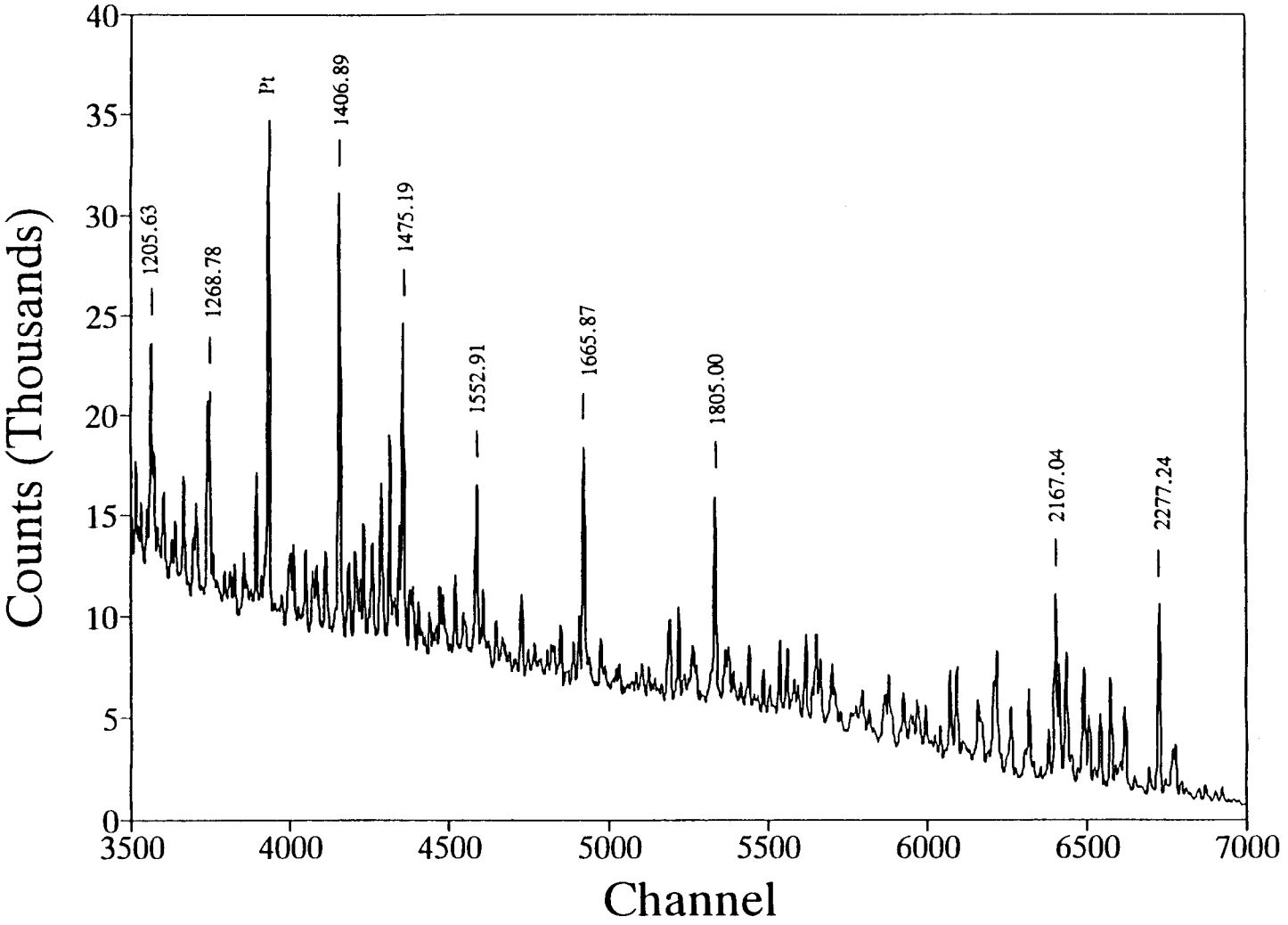

Figure 15b High-energy region of ^{187}Ir gamma-ray singles spectrum.

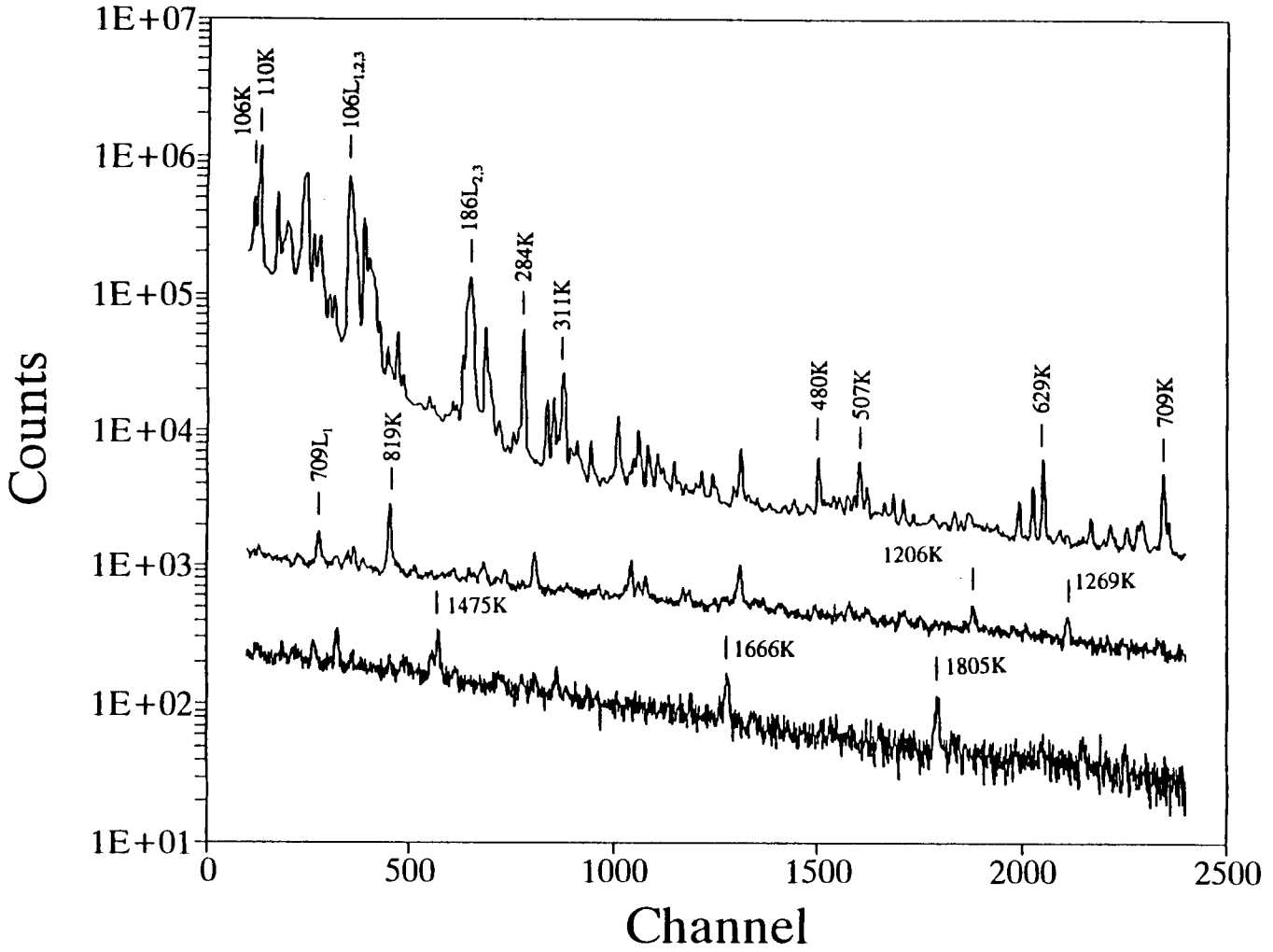

Figure 16 Conversion electron singles spectrum of ^{187}Ir.

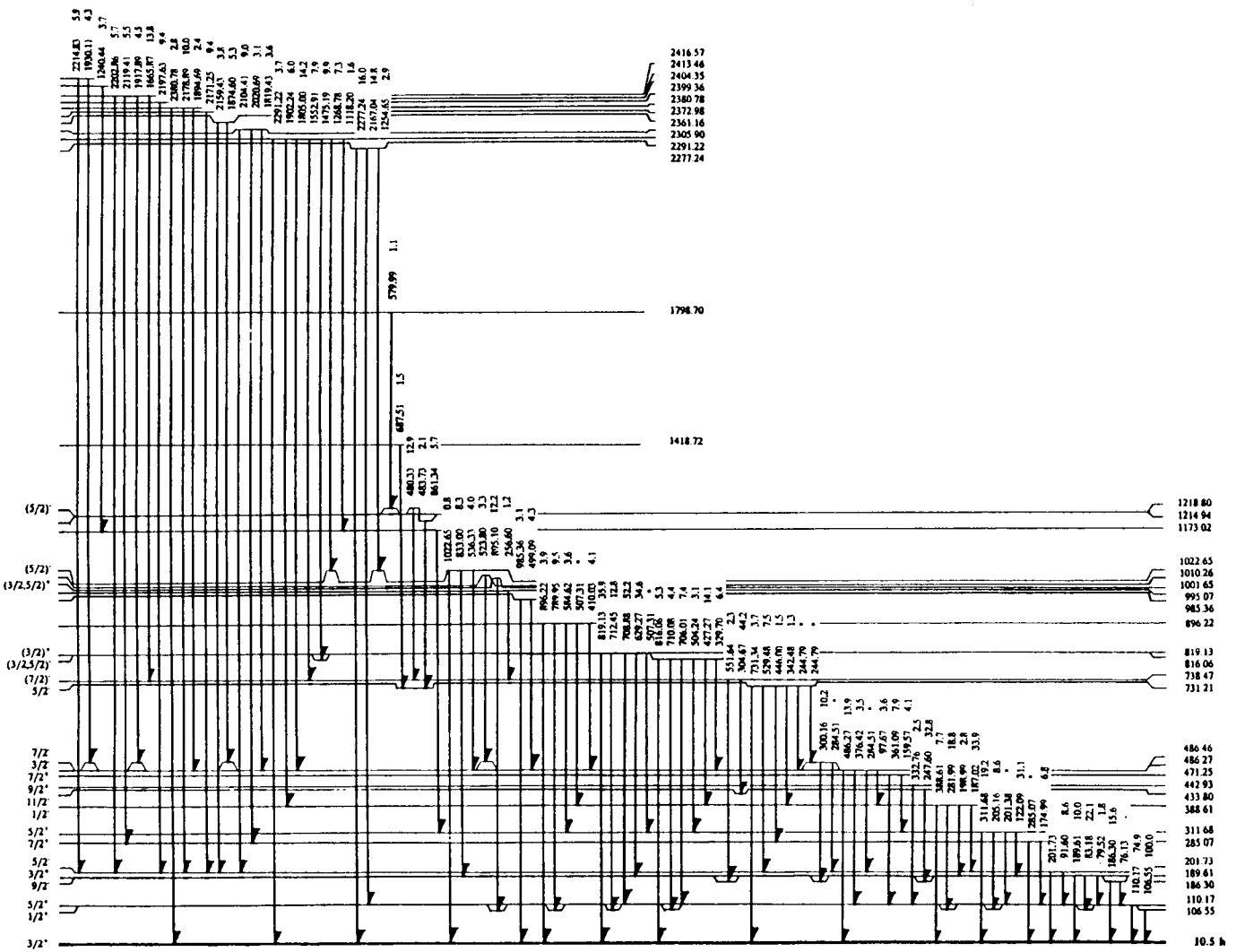

Figure 17 Proposed decay scheme of ^{187}Ir.

Coincidence events are generated whenever two γ rays or a γ ray and conversion electron are detected within approximately 200 nanoseconds of each other. The time between coincident events and the energies of each are written continuously on magnetic tape during the experiment. The histogramming program CHIL [Mil87] was used to build two-dimensional coincidence matrices, from which events occurring within a narrow time window (30-50 nanoseconds) were extracted.

Coincidence data helped to place many new transitions in the decay scheme. Low-energy electron-gated γ-ray rates are much higher than the competing gamma-gated rates due to both the large conversion for low energies and the high efficiency of the Si(Li). Several weak transitions to low-lying states were placed solely on e-γ coincidences. Selected electron-gated γ-ray or γ-gated electron coincidences are shown in Figures 18-21. Only those e-gated gamma or γ-gated electron gates which added any new information (that is, only the low-energy gates) are included in Table 6.

3.2.2 Results and Discussion

The strong triplet at 201 keV was very difficult to resolve, resulting in large uncertainties in the intensities. This triplet was resolved in the conversion electron spectrometer of [Sch73]. The third (weak) component is unplaced.

Also from conversion electrons, [Sch73] have identified the 244-keV line as a doublet with approximately equal intensities, and [Kem75] and [Fir91] placed the doublet depopulating the level at 731 keV. Strong coincidences with 300 and 486 keV transitions support their placement.

An additional 284 keV doublet depopulating the levels at 486.26 and 486.46 keV is suggested by coincidences with transitions feeding those levels. Gates on the 523-keV line (and others which feed the level at 486.46), for example, show no coincidences with the 187, 282, or 486 keV lines. Gamma rays populating the 486.27 level, however, *are* seen in coincidence with these lines (see Figures 20 and 21).

There was no evidence for double placement of the 333 keV line as in [Sch73].

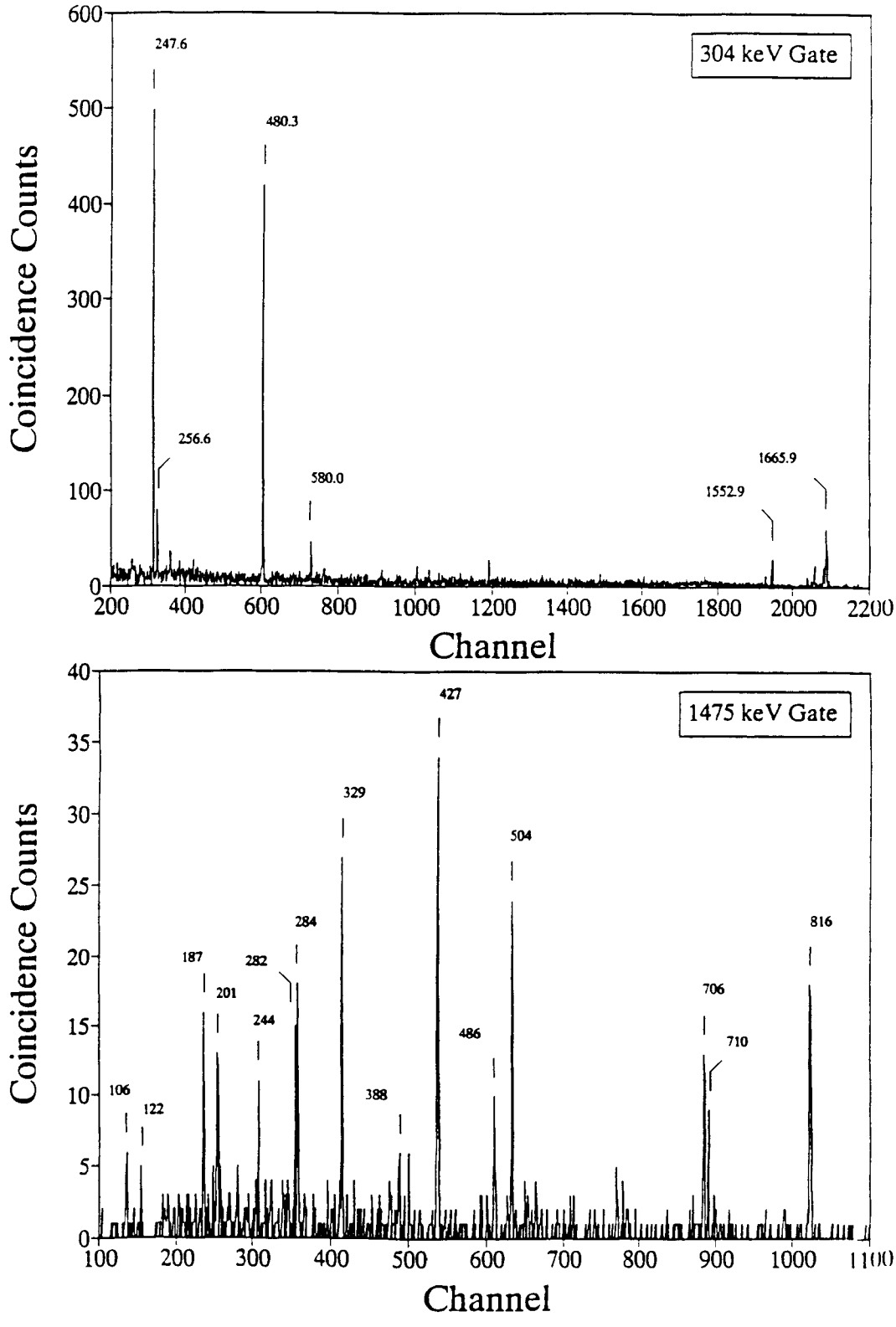

Figure 18 Gamma rays gated on the 304 and 1475 keV γ-ray transitions.

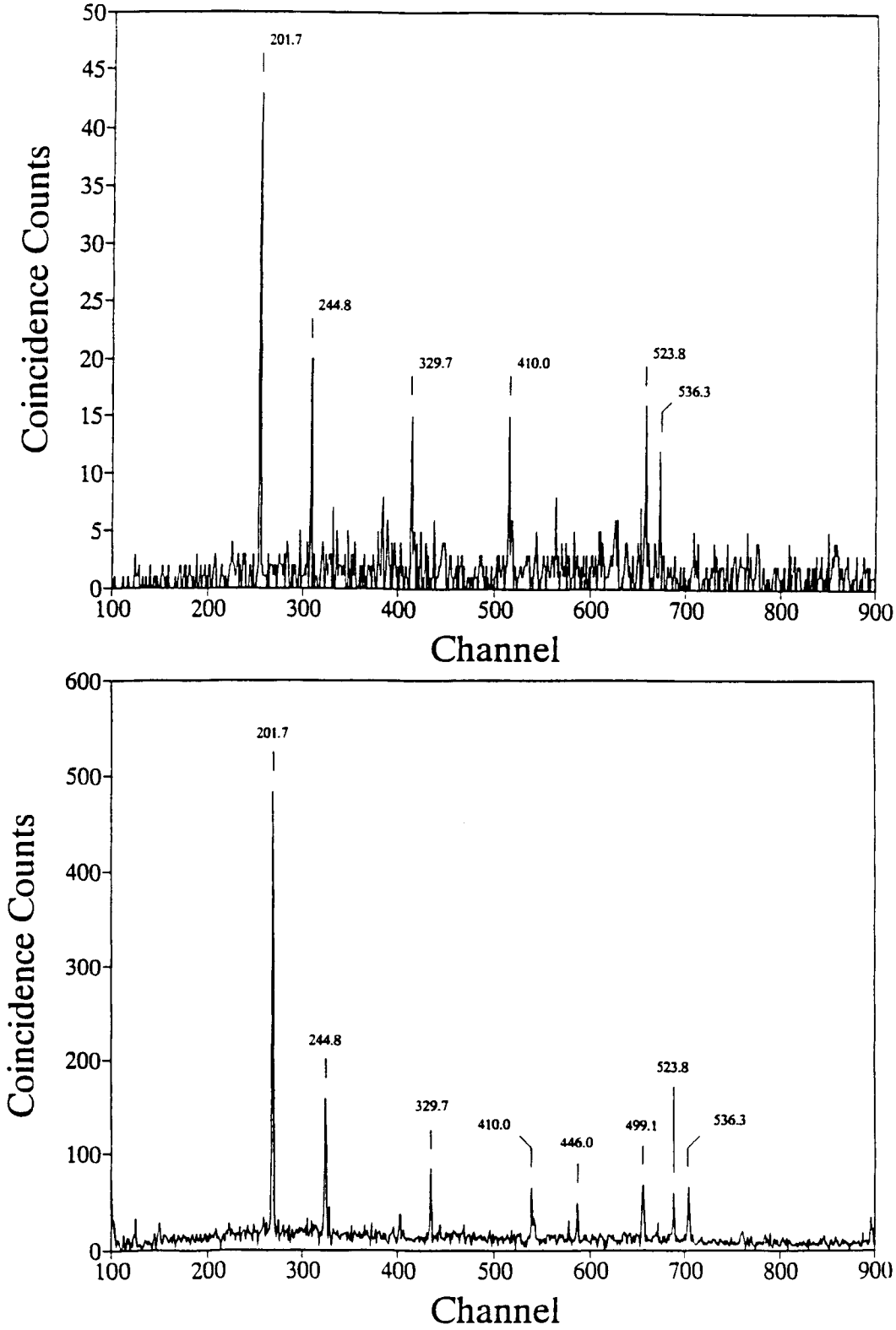

Figure 19 Gamma-gated (upper) and electron-gated (lower) γ rays in coincidence with 284 keV doublet depopulating the levels at 486.27 and 486.46 keV.

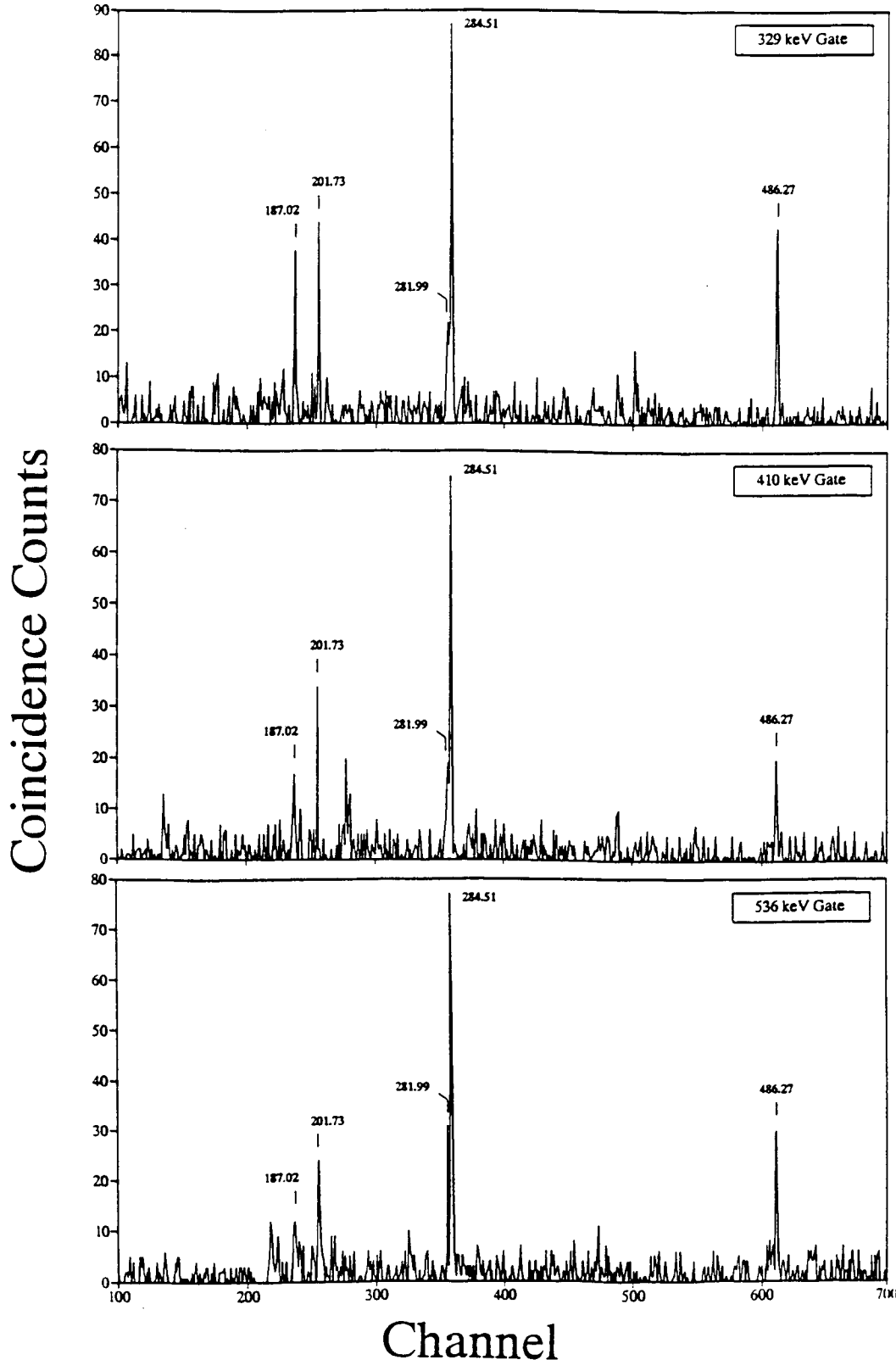

Figure 20 γ-gated coincidences with gamma-rays feeding the 486.27 keV level.

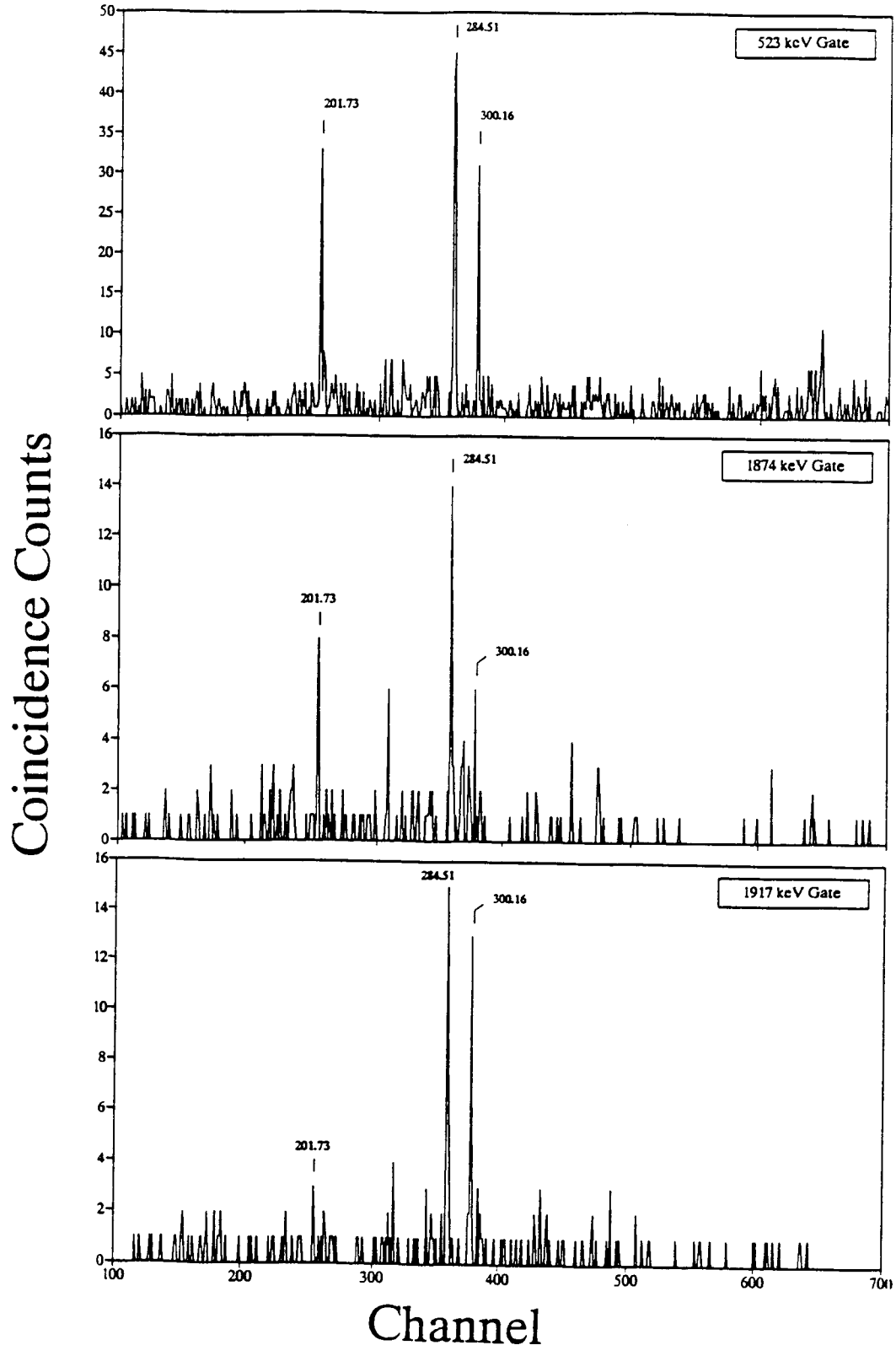

Figure 21 Gamma-rays coincident with those feeding the 486.46-keV level.

Strong coincidences with transitions from the 311 and 388 keV levels indicate that the line at 507 keV is a doublet. Coincidence gates were used to determine the relative intensities, and roughly equal intensities were assigned.

The strong 1475, 1552, and 1666 keV transitions are placed by coincidences, and energy sums of the latter two confirm the feeding of the isomer at 186.3 keV by the 247, 304, 480 keV sequence.

Many of the high-energy transitions populate the $5/2^-$ level at 201 keV. Level intensity balances don't seem to support all of this feeding, however γ-γ coincidences clearly justify their placement.

The line at 551 keV is in coincidence with that of 480 keV, and the energy sum strengthens its placement depopulating the level at 738 keV. The line is broad, indicating a doublet, and quite weak. The relative method was used to calculate the mixing ratio assuming it is in competition with the 304-keV *E*2 transition, and coincidentally (?) the mixing ratio is the same as that of the 550-keV line from Andre *et al.* [And75]. That gamma-ray, however is shown depopulating a level with I=15/2 which could not be observed in a decay (I_0=3/2) study.

Table 4 ^{187}Ir conversion electron data. Gamma-ray intensities are normalized to the 106-keV line, electrons to 304-keV, and conversion coefficients to the theoretical 304-keV *E*2 value.

E_e (keV)	Attribution	I_e	%err	α_{exp}	$E1_{th}$	$E2_{th}$	$M1_{th}$	Multipolarity
30.5	106.55K	2765	1.8	0.708(17)	0.2775	0.7040	4.354	*E*2(+*M*1)
95.3	106.55L_3	3806	1.1	0.974(19)	0.0104	0.9572	0.0064	
34.1	110.17K	7907	0.8	2.703(45)	0.2551	0.6671	3.954	*M*1+*E*2
97.0	110.17$L_{1,2}$	1839	1.9	0.629(15)	0.0336	1.0609	0.6438	
46.1	122.09K	3326	0.8	2.735(32)	0.1967	0.5520	2.947	*M*1+*E*2
108.4	122.09$L_{1,2}$	844.9	1.3	0.695(11)	0.0281	0.6792	0.4975	
110.3	*186.30K	761.7	1.5	1.25(7)	#0.5806	0.2055	0.8943	*E*3
173.6	186.30L_2	948.8	0.5	1.56(9)	#1.593	0.0932	0.0126	
175.3	186.30L_3	491.3	1.0	0.806(46)	#0.8871	0.0628	0.0012	
113.3	189.61K	304.8	1.7	0.781(24)	0.0646	0.1966	0.8507	*M*1+*E*2
128.9	205.16K	50.1	1.5	0.1494(33)	0.0531	0.1610	0.6814	*E*2
192.1	205.16$L_{1,2}$	29.6	2.6	0.0884(27)	0.0075	0.0807	0.1099	
168.6	*245.00K	195.1	0.9	0.442(8)	0.0342	0.1007	0.4241	*M*1(+*E*2)
231.4	245.00$L_{1,2}$	32.8	2.0	0.0743(19)	0.0049	0.0414	0.0673	
171.5	247.60K	599.1	0.6	0.468(18)	0.0334	0.0980	0.4120	*M*1(+*E*2)
234.1	247.60$L_{1,2}$	90.6	2.6	0.0708(33)	0.0047	0.0398	0.0653	
205.4	281.99K	31.0	2.7	0.0422(15)	0.0244	0.0703	0.2889	*E*1
224.1	300.16K	92.0	0.9	0.2299(42)	0.0210	0.0601	0.2438	*M*1(+*E*2)
286.7	300.16$L_{1,2}$	16.8	2.8	0.0419(13)	0.0030	0.0200	0.0385	
228.5	304.67K	100.0	0.8	0.0579(8)	0.0203	0.0579	0.2341	*E*2
291.6	304.67$L_{1,2}$	32.6	1.3	0.0189(3)	0.0029	0.0191	0.0370	
235.5	311.68K	149.3	1.6	0.1992(40)	0.0192	0.0547	0.2201	*M*1+*E*2
298.3	311.68$L_{1,2}$	24.1	2.6	0.0321(9)	0.0027	0.0176	0.0347	
253.5	329.70K	34.9	1.1	0.1396(24)	0.0169	0.0476	0.1891	*M*1+*E*2
316.4	329.70$L_{1,2}$	5.67	5.9	0.0227(14)	0.0024	0.0145	0.0298	
256.4	332.76K	5.57	3.9	0.0572(26)	0.0165	0.0466	0.1845	*E*2
266.4	342.48K	2.44	12.6	0.047(6)	0.0155	0.0434	0.1707	*E*2
284.8	361.09K	49.3	1.0	0.1596(28)	0.0137	0.0382	0.1481	*M*1
300.4	376.42K	6.41	8.0	0.0471(45)	0.0125	0.0345	0.1325	*E*1(+M2)
308.7	384.83K	20.1	1.8	0.1340(38)	0.0119	0.0327	0.1249	*M*1(+*E*2)
312.5	388.61K	3.97	13.6	0.0131(18)	0.0116	0.0320	0.1217	*E*1
324.2	400.73K	3.81	10.4	0.0073(8)	0.0108	0.0297	0.1122	*E*1
332.8	410.03K	15.2	1.5	0.0963(21)	0.0103	0.0282	0.1055	*M*1+*E*2
351.0	427.27K	9.45	2.9	0.0172(6)	0.0094	0.0256	0.0946	(*E*2)
404.2	480.33K	32.2	0.9	0.0641(13)	0.0073	0.0195	0.0695	*M*1+*E*2
466.9	480.33$L_{1,2}$	3.88	3.9	0.0077(3)	0.0010	0.0044	0.0108	

Table 4 continued.

407.7	483.73K	5.59	4.0	0.0685(35)	0.0072	0.0192	0.0682	*M*1
410.5	486.27K	4.59	4.7	0.0084(4)	0.0071	0.0190	0.0673	*E*1
419.2	495.34K	2.16	18.0	0.055(11)	0.0068	0.0182	0.0641	*M*1+*E*2
423.2	499.09K	9.16	2.5	0.0548(30)	0.0067	0.0179	0.0629	*M*1+*E*2
486.2	499.09$L_{1,2}$	1.74	10.4	0.0104(12)	0.0009	0.0040	0.0098	
431.2	*507.31K	30.9	0.9	0.0552(13)	0.0065	0.0172	0.0603	(*M*1)
494.1	507.31$L_{1,2}$	5.74	3.4	0.0102(4)	0.0009	0.0038	0.0094	
447.6	523.80K	6.86	2.6	0.0529(19)	0.0061	0.0161	0.0554	*M*1(+*E*2)
453.3	529.48K	10.7	1.6	0.0366(8)	0.0059	0.0157	0.0539	*M*1+*E*2
459.9	536.33K	9.13	3.0	0.058(7)	0.0058	0.0152	0.0521	*M*1(+*E*2)
541.0	617.05K	0.84	8.9	0.0097(9)	0.0043	0.0112	0.0363	(*E*2)
546.1	622.19K	20.8	0.8	0.0307(5)	0.0043	0.0110	0.0355	*M*1+*E*2
608.6	622.19$L_{1,2}$	5.86	2.5	0.0087(3)	0.0006	0.0022	0.0055	
553.2	629.27K	39.9	0.5	0.0295(5)	0.0042	0.0108	0.0345	*M*1+*E*2
615.9	629.27$L_{1,2}$	6.42	2.2	0.0047(1)	0.0006	0.0021	0.0053	
585.2	661.52K	7.74	2.1	0.0266(7)	0.0038	0.0097	0.0304	*M*1+*E*2
618.6	694.93K	7.95	2.4	0.0323(28)	0.0034	0.0088	0.0268	*M*1+(*E*2)
632.7	*708.88K	32.3	0.6	0.0159(3)	0.0033	0.0084	0.0255	
695.6	708.88$L_{1,2}$	6.82	2.3	0.0033(1)	0.0005	0.0016	0.0039	
636.3	712.45K	8.13	1.7	0.0162(4)	0.0033	0.0083	0.0252	*M*1+*E*2
652.2	728.33K	1.00	11.4	0.0147(19)	0.0031	0.0080	0.0238	*M*1+*E*2
656.2	*732.35K	2.05	4.3	0.0112(11)	0.0031	0.0079	0.0235	
713.7	789.95K	1.20	10.9	0.0032(4)	0.0027	0.0068	0.0194	*E*1
716.0	792.13K	2.58	5.2	0.0046(2)	0.0027	0.0067	0.0192	
719.7	795.74K	4.14	2.8	0.0153(5)	0.0026	0.0067	0.0190	*M*1+*E*2
743.0	819.13K	18.3	1.0	0.0131(4)	0.0025	0.0063	0.0177	*M*1+*E*2
806.1	819.13$L_{1,2}$	2.86	4.1	0.0020(1)	0.0003	0.0011	0.0027	
785.5	861.34K	1.40	6.6	0.0063(5)	0.0023	0.0057	0.0156	*E*2(+*M*1)
799.2	875.27K	0.88	7.2	0.0047(3)	0.0022	0.0055	0.0150	(*E*2)
819.6	895.10K	2.02	5.4	0.0042(2)	0.0021	0.0053	0.0141	(*E*2)
831.6	907.84K	0.61	9.6	0.0076(8)	0.0021	0.0051	0.0136	*M*1+*E*2
1130.3	1205.63K	1.71	4.3	0.0056(3)	0.0012	0.0030	0.0067	*M*1+*E*2
1165.5	1240.44K	0.63	11.2	0.0055(6)	0.0012	0.0029	0.0062	*M*1(+*E*2)
1193.3	1268.78K	1.59	5.8	0.0055(3)	0.0011	0.0028	0.0059	*M*1(+*E*2)
1331.6	1406.89K	1.70	3.7	0.0050(5)	0.00095	0.0023	0.0046	*M*1(+*E*2)
1394.8	1470.69K	0.93	5.5	0.0049(3)	0.00088	0.0021	0.0041	(*M*1)
1399.1	1475.19K	1.99	2.8	0.0052(3)	0.00087	0.0021	0.0040	(*M*1)
1477.0	1552.91K	0.64	6.4	0.0021(1)	0.00080	0.0019	0.0036	*E*2
1590.2	1665.87K	0.99	3.8	0.00183(7)	0.00071	0.0017	0.0030	*E*2(+*M*1)
1729.3	1805.00K	0.83	3.7	0.00149(6)	0.00062	0.0015	0.0024	*E*2
1739.7	1815.79K	0.14	9.2	0.00109(10)	0.00062	0.0014	0.0024	
1743.7	1819.43K	0.10	8.1	0.00071(6)	0.00062	0.0014	0.0024	*E*1

Table 4 continued.

1826.3	1902.24K	0.19	5.7	0.00080(5)	0.00057	0.0013	0.0021	(*E*1)
1842.0	1917.89K	0.08	9.7	0.00048(5)	0.00057	0.0013	0.0021	*E*1
1854.3	1930.11K	0.14	11.7	0.00085(10)	0.00056	0.0013	0.0021	(*E*1)
2028.7	2104.41K	0.30	6.9	0.00087(6)	0.00049	0.0011	0.0017	(*E*1)
2083.6	2159.43K	0.05	9.7	0.00031(3)	0.00047	0.0010	0.0016	*E*1
2095.1	2171.25K	0.16	8.0	0.00042(3)	0.00046	0.0010	0.0016	*E*1
2102.9	2178.89K	0.20	7.0	0.00051(4)	0.00046	0.0010	0.0015	*E*1
2121.5	2197.63K	0.14	7.5	0.00037(3)	0.00045	0.0010	0.0015	*E*1
2126.8	2202.86K	0.08	8.2	0.00036(3)	0.00045	0.0010	0.0015	*E*1
2138.7	2214.83K	0.08	8.4	0.00035(3)	0.00045	0.0010	0.0015	*E*1
2201.0	2277.24K	0.06	18.5	0.00009(2)	0.00043	0.0009	0.0014	(*E*1)

Unresolved doublets are indicated by "*", and values marked with "#" are $E3_{th}$. Theoretical K-conversion coefficients were interpolated through high-order fits of values from the table of Rosel *et al.* [Ros78]. Coefficients for L shells are from the National Nuclear Data Center PHYSCO routine which uses the tables of Hager and Seltzer, and those of Dragoun.

Table 5 Gamma-ray transitions in ^{187}Ir. Unresolved doublets are indicated by "*", in which case the summed intensity is given.

E_γ(keV)	I_γ	%err	E_{in}	I_{in}^π	E_{fin}	I_{fin}^π
76.13(10)			186.30	$9/2^-$	110.17	$5/2^+$
79.52(10)	1.8	6.4	189.61	$3/2^+$	110.17	$5/2^+$
83.18(10)	22.1	1.6	189.61	$3/2^+$	106.55	$1/2^+$
91.60(10)	8.6	1.6	201.73	$5/2^-$	110.17	$5/2^+$
97.67(10)	3.6	1.6	486.27	$3/2^-$	388.61	$1/2^-$
106.55(10)	100.0	1.6	106.55	$1/2^+$	0.00	$3/2^+$
110.17(10)	74.9	1.5	110.17	$3/2^+$	0.00	$3/2^+$
122.09(10)	31.1	0.9	311.68	$3/2^+$	189.61	$3/2^+$
159.57(10)	4.1	1.4	471.25	$7/2^+$	311.67	$5/2^+$
162.64(10)	1.6	2.4				
166.31(10)	1.0	3.8				
174.99(10)	6.8	1.4	285.07	$7/2^+$	110.17	$5/2^+$
186.30(10)	15.6	5.6	186.30	$9/2^-$	0.00	$3/2^+$
187.02(10)	33.9	3.1	388.61	$1/2^-$	201.73	$5/2^-$
189.61(10)	10.0	2.6	189.61	$3/2^+$	0.00	$3/2^+$
198.99(10)	2.8	3.2	388.61	$1/2^-$	189.61	$3/2^+$
*201.38(12)	67.2	1.6	311.68	$5/2^+$	110.17	$5/2^+$
*201.73(10)			201.73	$5/2^-$	0.00	$3/2^+$
205.16(10)	8.6	1.7	311.68	$5/2^+$	106.55	$1/2^+$
*244.79(10)	11.3	1.5	731.21	$5/2^-$	486.46	$7/2^-$
*244.99(10)			731.21	$5/2^-$	486.27	$3/2^-$
247.60(10)	32.8	3.8	433.80	$11/2^-$	186.30	$9/2^-$
256.60(11)	1.2	5.3	995.07		738.47	$(7/2)^-$
268.73(11)	0.5	6.3				
281.99(10)	18.8	2.2	388.61	$1/2^-$	106.55	$1/2^+$
*284.51(10)	56.6	4.3	486.46	$7/2^-$	201.73	$5/2^-$
*284.51(10)			486.27	$3/2^-$	201.73	$5/2^-$
*285.07(10)			285.07	$7/2^+$	0.00	$3/2^+$
300.16(10)	10.2	1.6	486.46	$7/2^-$	186.30	$9/2^-$
304.67(10)	44.2	1.1	738.47	$(7/2)^-$	433.80	$11/2^-$
311.68(10)	19.2	1.2	311.68	$5/2^+$	0.00	$3/2^+$
329.70(10)	6.4	1.3	816.06	$(3/2,5/2)^-$	486.27	$3/2^-$
332.76(10)	2.5	2.4	442.93	$9/2^+$	110.17	$5/2^+$
342.48(10)	1.3	2.9	731.21	$5/2^-$	388.61	$1/2^-$
361.09(10)	7.9	1.4	471.25	$7/2^+$	110.17	$5/2^+$
376.42(10)	3.5	5.1	486.46	$7/2^+$	110.17	$5/2^+$
384.83(10)	3.8	2.2				
388.61(10)	7.7	1.5	388.61	$1/2^-$	0.00	$3/2^+$
400.73(10)	13.4	1.8				

Table 5 continued.

410.03(10)	4.1	1.6	896.22	$(3/2)^+$	486.27	$3/2^-$
427.27(10)	14.1	1.9	816.06	$(3/2,5/2)^-$	388.61	$1/2^-$
439.59(10)	1.4	2.7				
446.00(10)	1.5	2.2	731.21	$5/2^-$	285.07	$7/2^+$
480.33(10)	12.9	1.9	1218.80	$(5/2)^-$	738.47	$(7/2)^-$
483.73(10)	2.1	3.2	1214.94		731.21	$5/2^-$
486.27(10)	13.9	1.8	486.27	$3/2^-$	0.00	$3/2^+$
495.34(10)	1.0	7.4				
499.09(11)	4.3	5.0	985.36		486.27	$3/2^-$
504.24(11)	3.1	6.1	816.06	$(3/2,5/2)^-$	311.68	$5/2^+$
*507.31(10)	14.4	2.1	819.13	$(3/2)^+$	311.68	$5/2^+$
*507.31(10)			896.22		388.61	$1/2^-$
523.80(11)	3.3	5.8	1010.26		486.46	$7/2^-$
529.48(10)	7.5	1.5	731.21	$5/2^-$	201.73	$5/2^-$
536.33(11)	4.0	11.5	1022.65	$(5/2)^-$	486.27	$3/2^-$
551.64(10)	2.3	2.3	738.47	$(7/2)^-$	186.30	$9/2^-$
555.64(10)	1.6	2.4				
579.99(15)	1.1	10.3	1798.70		1218.80	$(5/2)^-$
584.62(10)	3.6	2.8	896.22		311.68	$5/2^+$
586.73(10)	4.2	2.6				
596.56(11)	3.0	16.5				
617.05(10)	2.2	3.1				
622.19(10)	17.3	1.5				
629.27(10)	34.6	1.5	819.13	$(3/2)^+$	189.61	$3/2^+$
640.77(10)	2.8	1.8				
659.98(10)	1.9	2.9				
661.52(10)	7.5	1.4				
675.04(10)	2.6	3.2				
687.51(10)	1.5	3.9	1418.72		731.21	$5/2^-$
694.93(11)	6.3	8.2	896.22	$(1/2,3/2)^-$	201.73	$5/2^-$
706.01(10)	7.4	2.7	816.06	$(3/2,5/2)^-$	110.17	$5/2^+$
708.88(10)	52.2	1.7	819.13	$(3/2)^+$	110.17	$3/2^+$
710.08(16)	4.4	15.1	816.06	$(3/2,5/2)^-$	106.55	$1/2^+$
712.45(10)	12.8	1.8	819.13	$(3/2)^+$	106.55	$1/2^+$
728.33(12)	1.8	6.2				
731.34(14)	3.7	7.8	731.21	$5/2^-$	0.00	$3/2^+$
732.35(11)	4.7	8.8				
771.60(12)	1.9	5.8				
789.95(10)	9.5	1.2	896.22		106.55	$1/2^+$
792.13(10)	14.4	1.0				
795.74(10)	7.0	1.3				
816.06(10)	5.3	1.1	816.06	$(3/2,5/2)^-$	0.00	$3/2^+$
819.13(10)	35.9	2.6	819.13	$(3/2)^+$	0.00	$3/2^+$

Table 5 continued.

833.00(10)	8.3	1.1	1022.65	$(5/2)^-$	189.61	$3/2^+$
847.00(10)	3.3	1.3				
861.34(11)	5.7	5.7	1173.02		311.68	$5/2^+$
875.27(10)	4.8	1.5				
895.10(10)	12.2	2.3	1001.65	$(3/2,5/2)^+$	106.55	$1/2^+$
896.22(11)	3.9	6.5	896.22		0.00	$3/2^+$
907.84(10)	2.1	2.9				
912.87(10)	12.9	4.0				
977.52(10)	11.6	1.9				
978.83(10)	8.0	2.5				
983.82(10)	4.2	3.2				
985.36(12)	3.1	3.8	985.36		0.00	$3/2^+$
1022.65(14)	0.8	9.4	1022.65	$(5/2)^-$	0.00	$3/2^+$
1118.20(11)	1.6	3.8	2291.22		1173.02	
1145.85(14)	1.5	7.1				
1157.32(10)	2.4	2.5				
1201.30(12)	1.5	7.3				
1205.63(10)	7.9	1.7				
1208.44(10)	3.8	3.0				
1240.44(10)	3.7	1.6	2413.46		1173.02	
1254.65(12)	2.9	3.0	2277.24		1022.65	$(5/2)^-$
1268.78(10)	7.3	1.1	2291.22		1022.65	$(5/2)^-$
1406.89(11)	8.7	9.2				
1470.69(10)	4.8	1.8				
1475.19(11)	9.9	6.1	2291.22		816.06	(3/2,5/2)
1552.91(10)	7.9	2.2	2291.22		738.47	$(7/2)^-$
1600.81(12)	3.4	7.7				
1665.87(10)	13.8	1.1	2404.35		738.47	$(7/2)^-$
1805.00(10)	14.2	0.9	2291.22		486.27	$3/2^-$
1815.79(10)	3.2	2.3				
1819.43(10)	3.6	2.0	2305.90		486.27	$3/2^-$
1874.60(10)	5.3	1.6	2361.16		486.46	$7/2^-$
1882.39(10)	4.6	2.1				
1894.69(10)	2.4	2.9	2380.78		486.27	$3/2^-$
1902.24(10)	6.0	1.5	2291.22		388.61	$1/2^-$
1913.41(10)	6.7	1.5				
1917.89(11)	4.5	2.9	2404.35		486.46	$7/2^-$
1930.11(10)	4.3	1.9	2416.57		486.46	$7/2^-$
2020.69(11)	3.1	3.9	2305.90		285.07	$7/2^+$
2062.38(10)	7.0	1.3				
2101.42(11)	5.5	3.5				
2104.41(10)	9.0	1.1	2305.90		201.73	$5/2^-$
2119.41(10)	5.5	1.6	2404.35		285.07	$7/2^+$

Table 5 continued.

2134.44(10)	2.1	2.4			
2138.74(10)	7.2	1.1			
2143.55(11)	1.4	2.2			
2159.43(10)	3.8	1.7	2361.16	201.73	$5/2^-$
2167.04(10)	14.8	0.9	2277.24	110.17	$5/2^+$
2171.25(10)	9.4	1.1	2372.98	201.73	$5/2^-$
2178.89(11)	10.0	1.6	2380.78	201.73	$5/2^-$
2184.60(12)	2.1	3.8			
2197.63(10)	9.4	1.6	2399.36	201.73	$5/2^-$
2202.86(10)	5.7	1.4	2404.35	201.73	$5/2^-$
2214.83(10)	5.9	1.5	2416.57	201.73	$5/2^-$
2225.64(10)	9.1	1.1			
2231.13(11)	1.9	2.5			
2235.17(12)	2.1	4.4			
2266.62(10)	2.4	2.2			
2277.24(10)	16.0	1.0	2277.24	0.00	$3/2^+$
2291.22(10)	3.7	1.3	2291.22	0.00	$3/2^+$
2294.50(10)	4.3	1.2			
2300.97(10)	1.4	2.0			
2380.78(10)	2.8	1.2	2380.78	0.00	$3/2^+$

Table 6 ^{187}Ir γ-γ and γ-e coincidences. "*" denotes the strongest coincidence, "#" means there are more than 500 coincidences, "!" indicates more than 100, and "w" means less than 15 or questionable. Energies that are not annotated imply clear coincidence with $20 \leq N_{coin} \leq 100$. Counts have not been corrected for efficiency. Unresolved multiplets are denoted by "D" or "T".

Gate (keV)	Coincidences
79.5	122
83.2	106#*, 122!, 629w, 709w
91.6	110!*, 187!, 244, 247, 285!, 304
97.7	187!*, 199w, 201, 282, 388w
106.6	83#*, 122#*, 159, 205!, 282!, 507w, 629, 709, 712, 790, 895
110.2	79, 91!*, 122!, 175!, 201!, 333w, 361, 427w, 709!, 2167!
122.1	83!, 106#*, 110w, 159, 189, 507, 896w, 1118w
159.6	106, 122
162.6	-
166.3	110, 285w, 480w
175.0	110*, 499w, 2119w
187.0	91, 97!, 106w, 110w, 201#*, 244!, 329, 342, 427!, 507, 536, 695, 790w, 1475, 1805, 1902
189.6	122*, 187, 629*, 709w
199.0	83, 97w, 106*, 187, 189w, 244w
201.7T	83w, 97, 110, 187#*, 244!, 285#*, 329w, 427!, 507, 511, 529, 617, 661, 694, 1475, 1805, 1819, 1875, 1902, 1913w, 2104, 2159, 2171, 2179, 2197, 2203, 2214
205.2	106!*, 504, 507, 1813
244.8D	97, 106w, 187!, 201!, 285#*, 300!, 304w, 486, 687, 1208, 1558
247.6	285, 304#*, 384w, 480!, 1666
256.6	247, 304!*
268.7	201*, 285
282.0	97w, 106*, 201, 427
284.5T	91, 97, 106!, 110w, 201#*, 244#, 304, 329!, 388w, 410!, 427!, 446, 483, 499!, 507, 523!, 536!, 695, 1475, 1805!, 1819, 1875, 1918, 1930, 2020, 2119
300.2	199, 244!*, 384!, 523, 1875, 1930, 1916
304.7	247#*, 256!, 285, 480#*, 580, 728w, 801w, 1552!, 1627, 1641, 1660, 1666!
311.7	159, 504, 507*, 586, 1118, 1205, 1269
329.7	187!, 201!, 282, 285!*, 388w, 486!, 1475
332.8	110w
342.5	187, 201, 282, 388

Table 6 continued.

361.1	110*, 622w, 819w, 833w
376.4	244*
384.8	106w, 247w, 300, 400!*
388.6	106, 329, 410, 427!*, 536, 1805, 1902
400.7	187, 329w, 384!*, 427, 486w, 504w, 709, 816
410.0	106, 187, 201, 285!*, 388, 486
427.3	106, 187!*, 199, 201!, 282!, 388, 400, 1475!
480.3	247!, 304#*, 410, 551w, 580
483.7	201, 244*, 285w, 529w
486.3	244!*, 329!*, 400, 410, 536, 1666w, 1805, 1819, 1894
491.6	201*
495.3	895w
499.1	187, 201, 285!*, 300, 486
504.2	122, 201w, 205, 311, 1475*
507.3D	83w, 91w, 106, 110w, 122, 187!*, 199, 201!, 205, 282!, 311!*, 388, 511w
511.0	83, 106, 110, 122, 201!, 282!, 311!, 511!*, 596, 629, 709, 819, 1666w
523.8	201!, 285!*, 300!
526.4	-
529.5	201!*, 483
536.3	201, 282, 285!*, 486!, 1254, 1268
551.6	110w, 480
555.6	480w, 573w, 661*, 709w
579.9	304!*, 480, 732
584.6	106, 122w, 205, 311
586.7	122w, 311w, 732
596.6	511, 622!*, 709
617.1	201
622.2	596!*, 1666w
629.3	83w, 106*, 189
640.8	486w, 587w, 709*, 792
661.5D	201!*, 555, 732
675.0	1208w
687.5	244, 285w, 300w, 342w, 446w, 529w, 709, 731
694.9	187, 201!*, 304, 732
706.0	1475
708.9D	106, 110, 189, 641, 732!*, 789w
712.5	106w, 511w
728.3	285, 304, 480w, 486w
732.4	580, 622, 660, 709!, 792!*
771.6	-
790.0D	106w, 285, 640, 732!*, 822

Table 6 continued.

795.7	83^{w}, 1208*
816.1	400^{w}, 1475*
819.1	159^{w}, 201^{w}, 792^{w}, 1268^{w}
833.0	709^{w}, 1254, 1268
847.0	106^{w}, 285, 480, 1240
861.3	205^{w}, 311^{w}, 622^{w}, 661^{w}, 1118, 1240*, 1430^{w}
875.2	285^{w}
895.1	106^{w}, 285, 622, 1205*
907.8	311^{w}
912.9	-
977.5D	106^{w}, 244^{w}, 311^{w}, 1983^{w}, 1205^{w}
985.1	-
1118.2	201^{w}, 304^{w}, 861*
1145.9	201, 507^{w}
1157.3	110^{w}, 300^{w}
1201.3	201^{w}, 285*, 486^{w}, 622^{w}
1205.6	201, 205, 282, 311, 709, 792, 895*
1208.4	201^{w}, 244^{w}, 285*, 529*, 622^{w}, 875^{w}, 895^{w}, 795^{w}
1240.4	861
1254.7	486^{w}, 499^{w}, 511^{w}, 536^{w}, 790^{w}, 833^{w}
1269.8	285^{w}, 304, 486, 536^{w}, 833^{w}, 1022^{w}
1475.2	106^{w}, 122^{w}, 187, 201, 244, 282, 285, 329!, 388, 427!*, 486, 504!, 705, 709^{w}, 816
1552.9	304!*, 495
1600.8	-
1665.9	247^{w}, 304!*, 486, 511, 622
1805.0	187, 201, 282, 285!*, 388^{w}, 486
1815.8	285^{w}, 622
1819.4	285*, 486^{w}
1874.6	201, 244, 285*, 300, 486^{w}
1902.2	187, 201*, 282, 388^{w}, 597^{w}
1913.4	282, 311^{w}, 486^{w}
1917.9	285*, 300
1930.1	201^{w}, 285*, 300, 486^{w}
2104.4	201*
2119.4	175, 201^{w}, 285*
2159.4	201*
2167.0	110*, 187^{w}, 201^{w}
2171.3	106, 110^{w}, 122^{w}, 201*
2178.9	201*
2197.6	201*
2277.2	-

Table 6 continued.

Electron-gated gammas:	
E_e(keV)	Coincidences
47 (122.1)	83, 106, 159, 189, 504, 507, 586, 861, 978.8, 1205, 1268, 1475, 1600, 1882, 1913
95lo (106.6)	83, 122, 159, 205, 282, 427, 507, 629, 675, 709, 712, 732, 772, 790, 792, 795, 833, 861, 895, 977.5, 1205, 1240, 2062, 2101, 2138
95hi (110.2)	79, 91, 122, 175, 201, 333, 361, 376, 427, 507, 629, 709, 1407, 2167

Gamma-gated electrons:	
E_γ(keV)	Coincidences
166	$110L_{1,2}$
584	$79L_1$, 122_K
586	$79L_1$, 122_K
772	$106L_{2,3}$, $106M_3N_{2,3}$
792	$106L_{2,3}M_3N_{2,3}$
795	$79L_1$, $83L_1$, $106L_{2,3}$, $106M_3N_{2,3}$
895	$79L_1$, $83L_1$, $106L_{2,3}$, $106M_3N_{2,3}$, 189_K
978	$79L_1$, $83L_1$, $106L_{2,3}$, $106M_3N_{2,3}$, 122_K
1205	122_K
1600	122_K
2138	$106L_{2,3}$, $106M_3N_{2,3}$
2294	$110L_{1,2}$

4. Experimental Procedures -^{189}Ir

4.1 Nuclear Orientation of ^{189}Pt

As with ^{187}Pt, the nuclear orientation of ^{189}Pt was performed as a semi-on-line experiment following the implantation of ^{189}Au activity. Details of the experiment differed very little from those of the ^{187}Pt orientation, so only those procedures which were different will be commented on at this time.

^{189}Au activity was collected at the cold-finger for 25 hours while the orientation of Pt was monitored. Average Au production (and implantation) rates were about 4.4×10^5 atoms/sec. Following the implantation period, the beam was removed and the decay was monitored. All ^{189}Ir analysis was done using spectra collected during this period, as the contamination from Au decay during the beam-on cycles severely complicates the analysis of Ir lines from that data set. The reaction used to produce the activity was ^{181}Ta(^{12}C,4n)^{189}Au, with ^{12}C energies of 120 MeV. Spectra were collected in 10-minute cycles at 7 angles relative to the applied field, while gamma-ray singles spectra were continuously monitored and written periodically to the disk

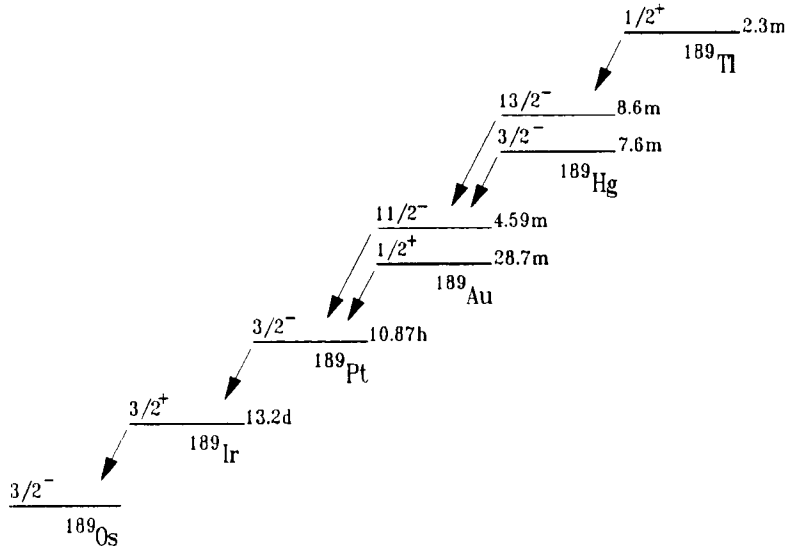

Figure 22 Decay sequence following ^{189}Tl production.

of the MicroVax II. One 6-hour cold period was followed by a 13-hour warm collection period. The ^{189}Au decay sequence is shown in Figure 22 for half-life comparison, and to illustrate the choice of collection times. Since ^{189}Tl was produced for the spectroscopy experiment, the decay chain is shown for ^{189}Tl production.

Portions of the 0° and 90° spectra are shown in Figure 23 to illustrate the large anisotropies of three lines near 600 keV. Counts have been normalized to the "warm" count-rates, so that the anisotropy is clearly visible. The anisotropies of the lines at 569, 608, and 627 keV are respectively -10%, -29%, and $+50\%$. As the gamma spectrum was exceptionally "clean" and high implantation rates were achieved, it was possible to find a_2 and a_4 coefficients for over 100 transitions in Ir. The coefficients are compiled in Table 7. As in ^{187}Pt, the ground-state of ^{189}Pt has $I_0=3/2$, so that a_4 terms in the angular distribution must be equal to zero. This is clearly the case as can be seen in the table, and only those lines with very low intensities (resulting in large uncertainties) are seen to have a_4 coefficients which are different from zero. The analysis of angular distribution coefficients was identical to the ^{187}Ir analysis except that the detector at 225° was used instead of 135°. From the summed spectra, the base temperature was found to be 6.8(1) mK, the same as that reached during the ^{187}Pt orientation run.

Mixing ratios were calculated for several transitions using the relative method. These are compiled in Table 10 along with theoretical values from the PTRM and values taken from [Fir90]. Signs were determined for several of those values from [Fir90] using our NO data.

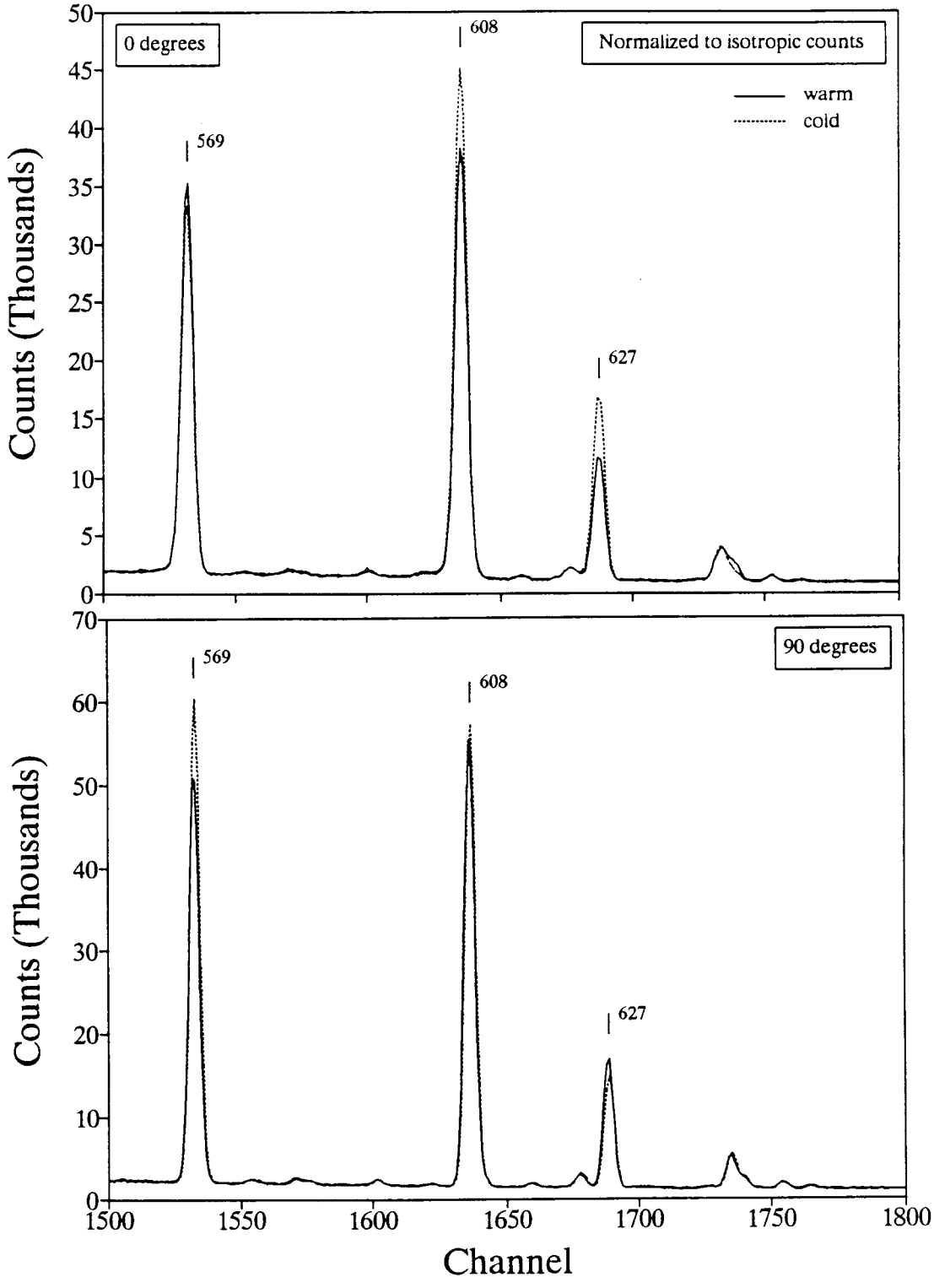

Figure 23 Portion of ^{189}Ir spectra illustrating large anisotropies in the region of 600 keV. The 627-keV line has an anisotropy of A(90°)= 50%.

Table 7 Coefficients of the Legendre polynomials for ^{189}Ir. Values have already been corrected for Q_λ, so that $a_\lambda = U_\lambda B_\lambda A_\lambda$.

E(keV)	a_2(da_2)	a_4(da_4)	E(keV)	a_2(da_2)	a_4(da_4)
94.31	0.045(7)	0.045(10)	828.11	-0.058(22)	-0.021(28)
113.79	0.260(26)	0.031(29)	835.99	0.231(48)	0.06(6)
141.09	0.114(5)	-0.005(7)	879.84	-0.022(43)	-0.00(6)
176.50	0.122(10)	0.004(13)	883.91	0.017(32)	-0.002(43)
181.27	0.162(42)	0.07(6)	911.53	-0.061(32)	0.060(35)
186.73	0.175(6)	-0.004(7)	924.74	-0.041(16)	-0.041(23)
190.85	-0.09(5)	-0.04(6)	929.68	0.34(7)	-0.25(12)
203.94	-0.180(21)	-0.004(26)	934.44	0.11(7)	0.08(11)
212.73	-0.13(7)	-0.00(8)	968.83	-0.044(44)	-0.037(48)
223.28	-0.220(7)	0.017(9)	986.73	0.07(6)	0.09(8)
243.46	-0.082(8)	-0.013(8)	992.57	-0.216(44)	-0.00(6)
258.35	-0.177(31)	-0.026(36)	1002.69	-0.21(6)	-0.02(8)
275.49	0.30(8)	-0.22(11)	1007.91	0.115(34)	-0.03(5)
284.60	-0.01(5)	0.04(6)	1012.18	-0.13(7)	0.05(9)
288.34	-0.38(11)	0.09(13)	1026.73	-0.172(13)	0.032(17)
296.01	-0.02(10)	0.04(9)	1034.27	-0.07(6)	0.09(8)
300.54	-0.093(3)	0.005(4)	1044.28	0.155(44)	-0.05(7)
317.64	0.359(4)	-0.010(6)	1070.77	-0.26(5)	-0.07(7)
351.17	0.27(7)	0.02(12)	1080.74	0.092(45)	0.09(7)
352.70	-0.188(41)	0.11(5)	1089.38	0.06(9)	0.04(11)
404.05	0.033(7)	0.003(10)	1106.43	0.054(22)	0.013(29)
430.98	0.059(36)	-0.01(5)	1108.86	0.510(38)	0.04(6)
459.68	-0.09(5)	0.16(8)	1120.14	-0.10(5)	0.18(6)
493.05	-0.161(26)	0.060(35)	1143.82	0.03(9)	-0.02(12)
530.30	-0.100(36)	0.024(43)	1183.60	0.20(9)	0.04(13)
540.03	-0.209(45)	-0.00(5)	1207.56	0.18(6)	0.08(10)
545.00	-0.237(4)	0.008(5)	1230.72	-0.41(6)	0.23(8)
568.92	-0.062(3)	-0.006(4)	1241.06	-0.459(48)	0.04(6)
576.95	-0.31(9)	0.13(11)	1253.99	0.105(17)	0.001(26)
594.74	0.32(6)	0.11(8)	1312.43	0.100(44)	0.09(7)
607.63	0.164(3)	-0.029(4)	1323.38	0.011(18)	-0.068(25)
616.16	-0.10(8)	0.14(10)	1326.85	-0.20(7)	0.04(8)
623.15	-0.043(32)	0.016(34)	1344.30	0.12(5)	0.04(8)
627.10	0.503(6)	-0.025(7)	1362.72	-0.25(5)	0.12(7)
644.35	0.079(11)	0.000(14)	1381.53	-0.33(5)	-0.06(6)
651.58	-0.047(31)	-0.001(43)	1387.65	-0.026(42)	0.08(6)
655.40	-0.36(7)	0.08(8)	1395.06	0.09(7)	-0.21(11)
698.38	0.023(22)	-0.030(31)	1405.64	0.11(5)	-0.11(7)

Table 7 continued.

721.39	0.245(4)	-0.012(6)	1408.24	-0.13(5)	-0.03(6)
726.35	0.137(48)	0.09(8)	1422.66	0.01(7)	-0.13(11)
733.78	0.039(34)	0.068(48)	1446.23	-0.39(6)	0.21(8)
735.80	-0.378(30)	-0.025(36)	1457.89	-0.088(31)	0.067(44)
751.21	0.01(6)	-0.04(9)	1496.54	-0.008(37)	-0.06(6)
756.13	-0.03(5)	0.01(8)	1501.56	-0.114(33)	-0.011(47)
782.12	0.05(7)	-0.01(9)	1509.84	0.20(8)	0.17(11)
788.88	-0.262(33)	0.039(39)	1528.69	0.219(45)	-0.05(7)
792.72	-0.007(7)	-0.003(8)	1571.51	0.277(37)	0.08(6)
798.56	0.290(24)	-0.036(30)	1593.12	-0.08(7)	0.29(7)
808.85	0.15(6)	-0.12(8)	1613.07	0.07(6)	-0.06(10)
811.57	0.045(35)	-0.011(47)	1652.80	0.00(5)	0.09(8)

4.2 Spectroscopy of ^{189}Ir

The ^{189}Ir spectroscopy was performed before the nuclear orientation run and prior to installation of the ND9900 data acquisition system. Data was taken using the Tennecomp computer, which performed multiscaling and multi-channel analysis. This data acquisition system is described in detail in [Car76]. Six time-planes were recorded to provide half-life identification of transitions in Ir. Identification of new lines was made on the basis of multiscaled and coincidence data. Coincidence data consisting of γ-γ, and γ-e coincidences were written to tape on the Perkin-Elmer system from which 2-D coincidence histograms were produced.

The reaction ^{181}Ta(^{16}O,8n)^{189}Tl was used to produce the Pt activity. The cross-section for production of Tl was maximized at an ^{16}O energy of 160 MeV. To remove as much parent activity as practical from the Ir spectrum, activity was collected on the tape for two hours, allowed to decay for one hour, then moved on to the next station. Some of the 28.7-m Au activity remained in the sample, but the three-hour collection times (6 30-minute time-planes) reduced the intensity relative to the Pt decay. Multiscaled gamma-ray and electron singles and γ-e coincidences were recorded at the first station using a Ge detector and a cooled Si(Li), while the second station recorded γ-γ coincidences and multiscaled singles events. Energy and efficiency calibrations were made using NBS standard-sources. All energies and intensities reported here represent SAMPO fits of the summed singles data. ^{189}Ir γ-γ coincidences are shown in Table 8. Figure 24 shows the summed gamma-ray spectrum from the Ge detector which was used for energy and intensity determination.

The spectroscopic work of [Hed72] was rather complete; only a few small discrepancies between that data and our own exist. Newly identified lines have, on the average, less than 1% relative intensity. It was proposed to do a "top-down" analysis of the ^{189}Pt orientation data, however, so it was decided to redo the spectroscopy. Complications in the conversion electron spectra made analysis of that data quite difficult, and so our conversion data is not as complete as earlier work. The decay scheme of ^{189}Ir of [Hed72] (taken from [Fir90]) is shown in Figure 25. Analysis of

coincidence data is not complete at this time, so an updated decay scheme is not presented. Strong coincidences with several of the unplaced transitions indicate that placements should be possible. Complete spectroscopy data will be published at a later date.

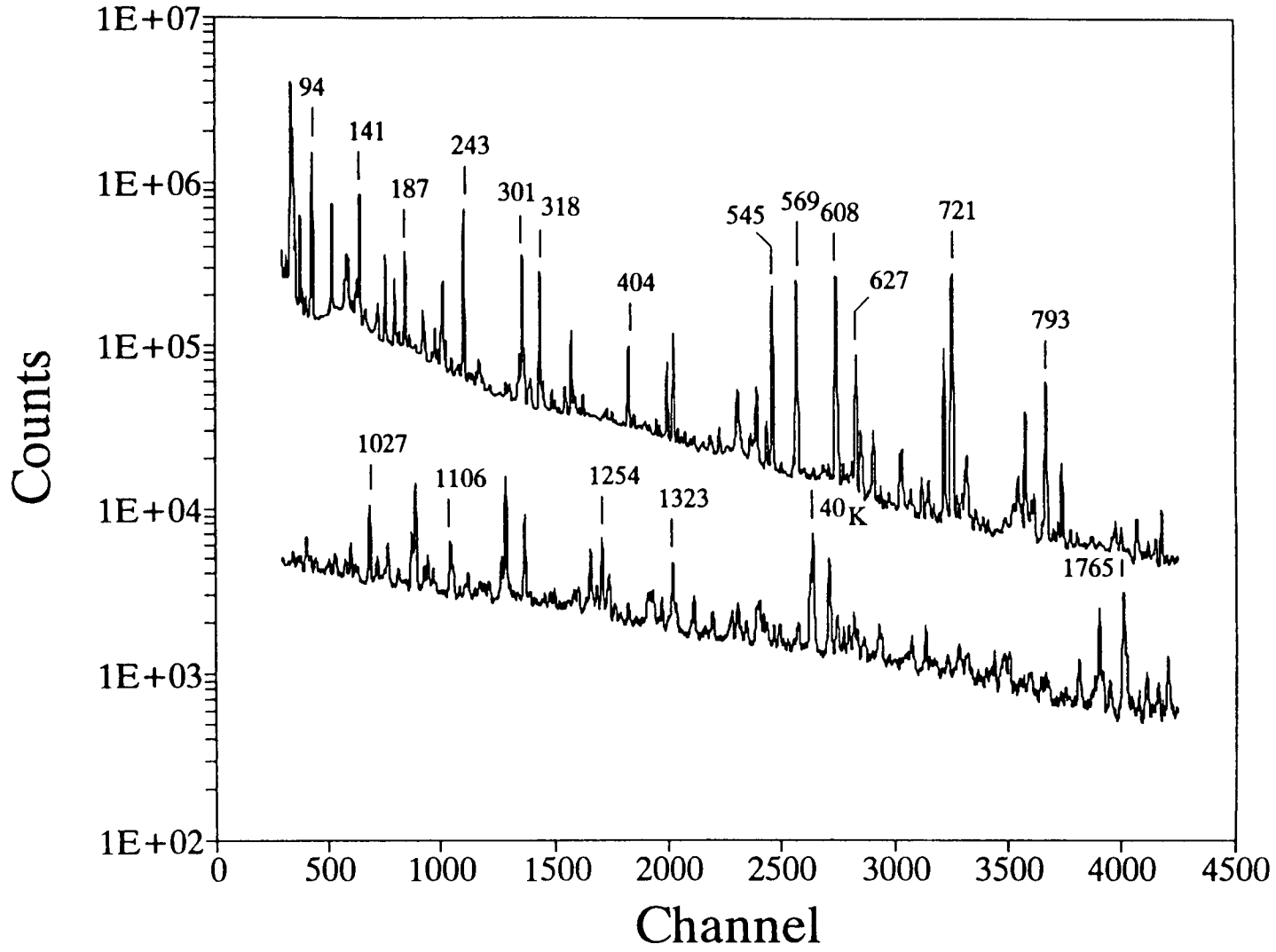

Figure 24 ^{189}Pt γ-ray singles spectrum.

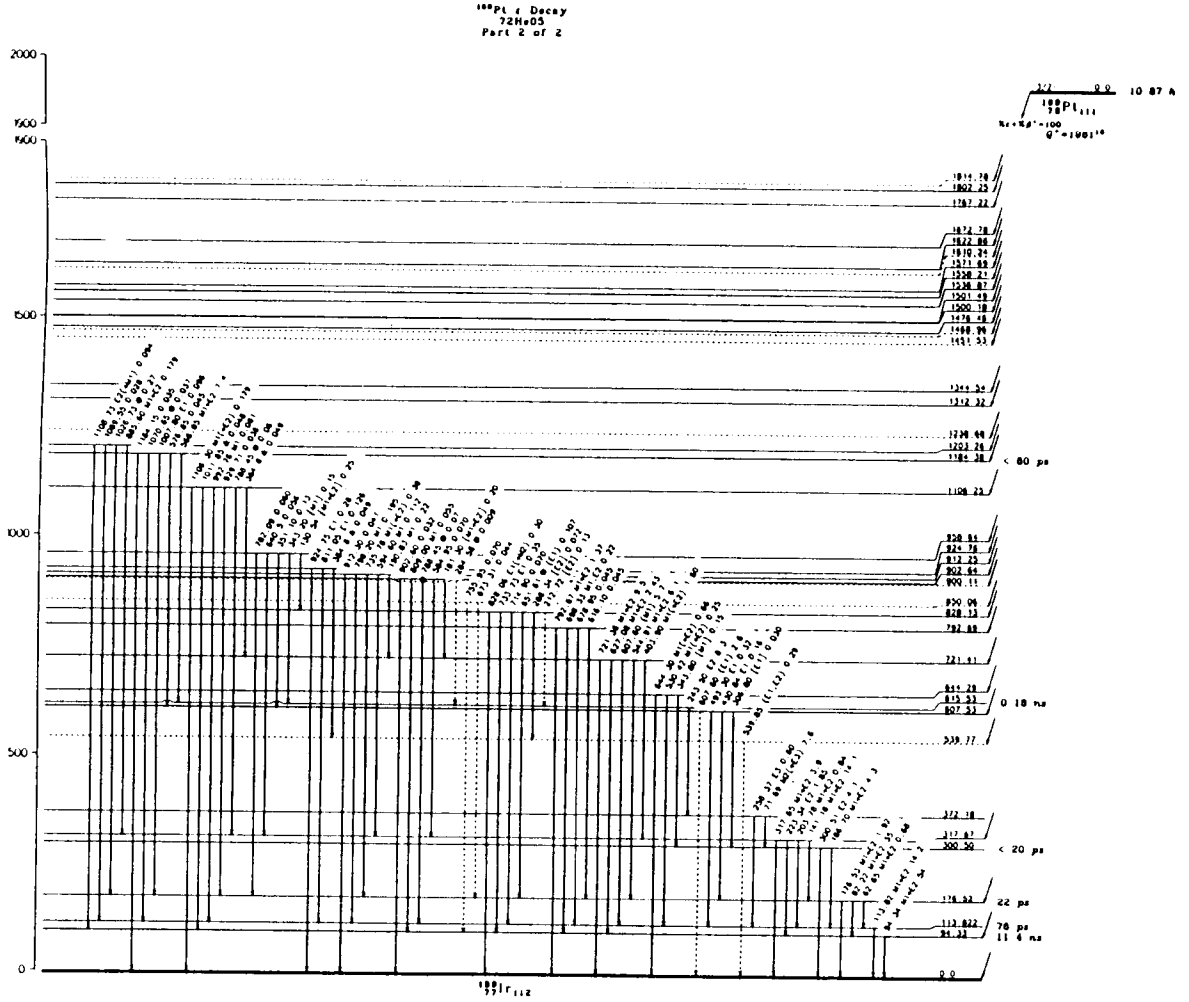

Figure 25a ^{189}Ir decay scheme (taken from [Fir90]).

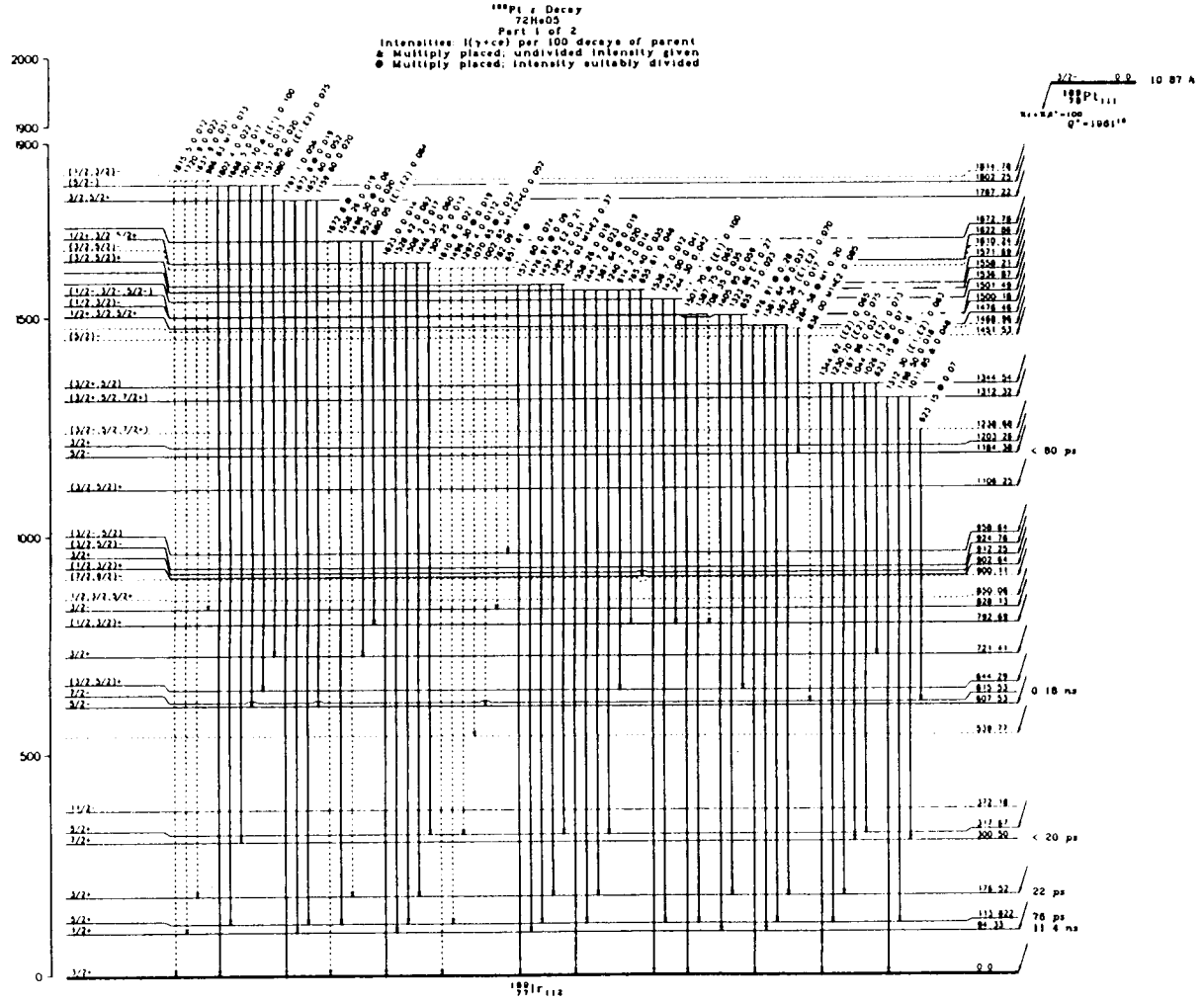

Figure 25b ^{189}Ir decay scheme (taken from [Fir90]).

Table 8 ^{189}Ir γ-γ coincidences. Strong coincidences are denoted by "S", and the strongest is given by "*". Intermediate and weak lines are indicated by "M" and "W" respectively. Quantitatively, "S" means more than 100 coincidences, "M" means $25 < N_{coin} < 100$, and "W" implies that less than 25 counts are seen.

Gate (keV)		Coincidences
76(K_α)		82 88 94 114 127 141 176 181 187 191 204 213 217 223 243 258 296 301 318 351 404 431 493 530 540 545 569 577 586 595 608 627 644 652 655 698 721 726 734 736 789 793 798 812 828 886 892 925 986 993 1008 1027 1071 1089 1144 1157 1159 1254 1323 1388 1458 1477
82	S:	94* 141* 404 545
	M:	431 608 726 736 1027
	W:	679 1008 1254 1323
85	S:	141*
	M:	545 608
	W:	187
94	S:	82 141* 223 404 545 627
	M:	288 431 608 610 623 698 734 726 736
	W:	886 1027 1109 1254 1323 1408 1478 1497
114	S:	141 181 187* 608* 204 258 493 530 608 674 799
	M:	191 351 789 812 1458
	W:	993 1071 1089 1231 1363 1388 1423 1653
141	S:	82 94* 176 404
	M:	595 886 1254
	W:	1593
176	S:	141* 404 431 545
	M:	736
	W:	726 886 1027 1254 1323
181	S:	94 114 243 721*
	M:	82 627 655
	W:	404 545
183	S:	114 133 243 361* 385 424 443 538
	M:	117 461 644
187	S:	114* 243 459 *(+lots of Pt)*
	M:	263 307 603 608 1044
	W:	886 1012
191	S:	82 721*
	M:	94 114 127 243 356 404 438 608
	W:	798

Table 8 continued.

204	S:	94 114* 404
	M:	176 243 721
	W:	1254
206	S:	82 94*
	M:	176 243 404 586
212	S:	243*
	M:	94 623
	W:	987
223	S:	94*
	M:	404
	W:	715 886 1254
243	S:	212 217 284 343 353 569* 623 836
	M:	809
	W:	698 709 751 956 986
243hi	S:	212 284 343 353 569*
	M:	94
	W:	608 836
252	M:	82 94 114 141 243 608
	W:	431 494
258	S:	114*
	M:	243 925
	W:	644 812
263	S:	301*
	M:	187 243 296
	W:	782
284	S:	243* 284*
	M:	94
288	S:	94*
	M:	82
	W:	431 438 608 1208
296	M:	187 243 263 318 569
301	S:	263*
	M:	296 307 421 569 603 884 1044
	W:	485 1012
318	S:	404*
	M:	82 94 114 296 431 494 586 608 886 1254
	W:	930 934 1003 1160 1241 1306
343	S:	114 243*
	W:	493 809
lo351	S:	114*
	M:	141 243
	W:	438 856 1208

Table 8 continued.

hi351	S:	217 244 460*
	M:	94 114
	W:	1208
404	S:	82 94 114 128 141* 176 223 318
431	S:	94 176*
	M:	82 114 318
	W:	577
459	S:	353*
493	S:	114*
	M:	243 318 343
	W:	577 782 828
540	S:	644*
	M:	530
	W:	114
545	S:	82 94* 176
	M:	114 181 191
569	S:	243*
	M:	318
	W:	632
577	M:	114 431 494 608
	W:	94 925
lo583	W:	94 114 141
hi583	W:	141 318
594	M:	82 94 114 141* 191 318*
608	S:	114*
	M:	94 177 181 187 191 318 577
609	S:	94 114*
	M:	82 183 204
616	M:	94 177
	W:	569
623	M:	94 213* 243* 652 715 734 828
627	S:	94*
	M:	181 187 191 243
644	S:	540*
	M:	183 243
651	M:	82 94 176 623
655	M:	114 181
	W:	789
721	S:	181* 191
	W:	721 892
726	M:	82 94
	W:	176 656

Table 8 continued.

lo734	S:	94*
	M:	623
	W:	987
hi734	S:	94*
	M:	82 176
	W:	431 493 608
751	M:	828
	W:	94 212 243 652 734
756	M:	94*
765	W:	792
772	W:	94
782	W:	263 301
788	S:	114*
	W:	656
792	W:	765 821
798	S:	114*
	M:	82 94
808	M:	243* 343 734
	W:	94 114 187 213 301
812	M:	114 213 302
	W:	94 692
828	M:	627
	W:	493 751 772 987
836	S:	243*
	W:	608
880		None
886	W:	94 114 608
925	W:	387 420
930	W:	82 94 114 141* 176 318
934	W:	114 141 223* 318
951	W:	114 141* 318
986	W:	94 114 141 176 243* 734
993	M:	114*
1003	W:	82 94 141* 318 223
1007	W:	94
1012	W:	114 187* 301
1026	M:	82 94* 141 176
1034	W:	94
1044	M:	187 301*
	W:	114
1070	W:	94 114
1080	W:	114
1089	W:	114

Table 8 continued.

lo1106		None
hi1106	M:	94*
1124	W:	141 318
1144	W:	94
lo1157	W:	94 114
hi1157	W:	176
1168		None
1184	W:	94
1207	W:	94 114* 288 351
1230	M:	114
1241	W:	141 318
1254	S:	141* 318
	M:	82 94 114 204 223
1323	M:	94*
	W:	82 176
1362	W:	114*
1381	W:	82 94
1387	M:	114*
	W:	94
1395	W:	94
lo1406	W:	94
hi1406	W:	94 114
1423		None
1446	W:	94
1457	S:	114*
lo1476	W:	94
hi1476	W:	94
1496	W:	82 94
1501		None
1528	W:	94
1572		None
1593	W:	141* 318

5. Nuclear Structure Theory

5.1 Introduction

Since the early 1950's and the first complete nuclear spectroscopic experiments, it has been known that nuclei with either the number of protons or neutrons equal to 2, 8, 20, 28, 40, 50, 82, or 126 exhibit somewhat unusual properties. A plot of separation energies, for instance, indicates that nuclei with these "magic" numbers of nucleons are more tightly bound than even their nearest neighbors. It was also known that these nuclei possess no ground-state electric quadrupole moments, indicating that the charge distributions were spherical. These two pieces of evidence lead to the understanding that nuclei at magic numbers constitute closed or filled nuclear shells. The nuclei then deviate from sphericity as they depart from the closed-shell regions. The nuclear shell model, developed in 1948 by Mayer, Jensen, Haxel, and Seuss [May49, May50, Hax49, Hax50], very successfully accounted for these observations, helping to clarify much about the structure of the nucleus. It is still the basis for much of today's knowledge of nuclear structure. In 1963 Mayer and Jensen received the Nobel Prize for their work on the shell model.

It is now well known that nuclei across the mass-table exhibit several different stable, ground-state shapes. In addition to the spherical nuclei which exist at closed shells, prolate, oblate, and triaxial shapes are also common. These different shape configurations can generally be understood as being due either to the collective behavior of the core itself, or to the elongated orbits of valence nucleons beyond the (tightly-bound) closed shells. Nuclei lying between regions of stable spherical, prolate, or oblate deformations are the so-called transitional nuclei, which very often exhibit either vibrational "softness" or triaxiality. The triaxiality can best be understood in terms of a nucleus having three different moments of inertia, whereas both the cigar-shaped prolate and doorknob-shaped oblate nuclei have an axis of symmetry, and can therefore be characterized using only two independent moments.

As can be seen in Figure 26, the deformed nuclei make up a large percentage

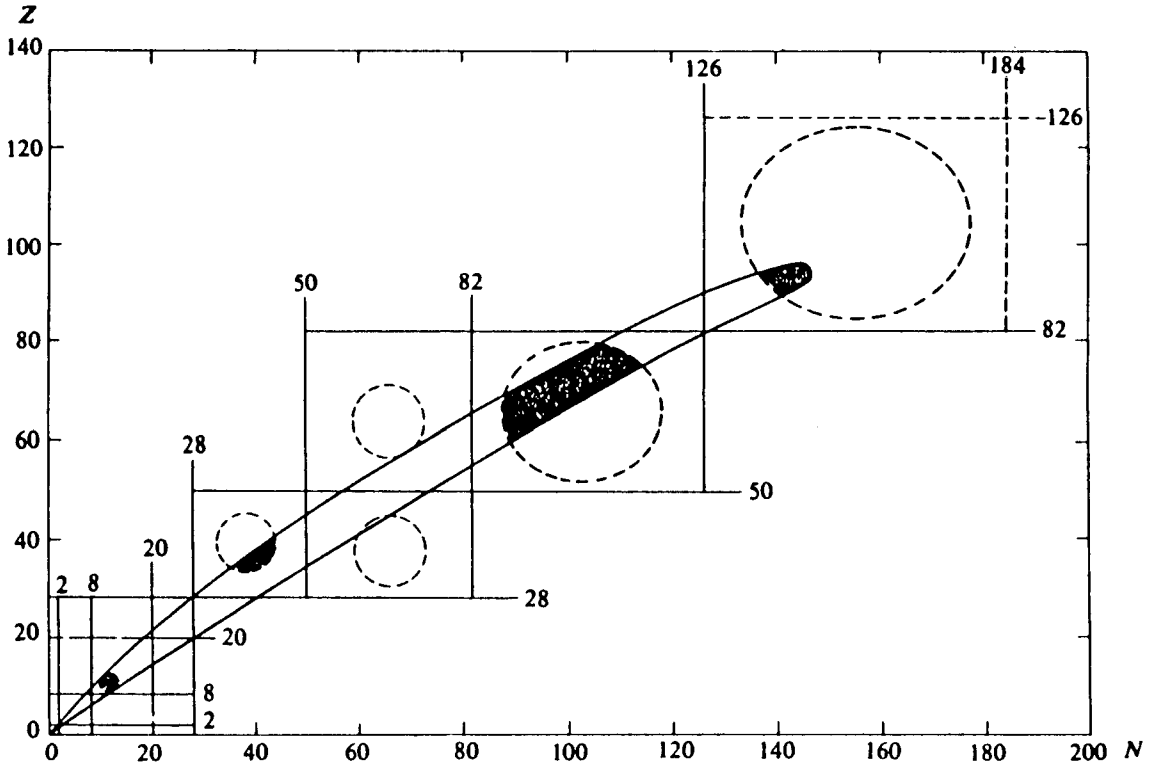

Figure 26 Segre-plot of the nuclei. Magic-numbers are shown as straight lines, and the deformed regions are indicated by dotted lines. Shaded areas represent deformed nuclei within the valley of β-stability.

of the 2300+ known nuclear species. Studying the behavior of deformed nuclei, then, can lead to much understanding of the nuclear force and insight into nuclear properties in general. Since the early 1950's, numerous theoretical approaches have been undertaken to describe low-spin properties of the odd-mass, deformed nuclei. Among the most successful of these are the phenomenological Interacting Boson-Fermion Model (IBFM) and Particle-Rotor Models. These models have sought to describe such various nuclear properties as level energies and static and transitional electromagnetic moments over a wide range of nuclei.

Perhaps the most concrete knowledge of nuclear shapes comes from measurements of the electric quadrupole moments, Q. These are directly related (albeit via some model) to the nuclear charge radii, and therefore (presumably) to the shape of the nucleus. Unfortunately, model dependence comes into the picture when we try to understand the intrinsic quadrupole moments, Q_0 (the moment in the nucleus' rest frame). As an illustration, a prolate nucleus rotating about an axis which is NOT the symmetry axis appears in the lab frame to be oblate. Some assumptions about the projection of the total angular momentum on the symmetry axis must therefore be made in order to extract intrinsic quadrupole moments.

Another sensitive measure of the nuclear shape is the multipole mixing ratio $\delta(E2/M1)$, as defined in Equation (13). As the matrix elements suggest, the mixing ratios are very sensitive to the nuclear wave function itself (Nilsson states for deformed nuclei), and can therefore be used as a tool for understanding the nuclear structure. The phase of the mixing ratio is also important, so successful models must therefore be able to consistently predict the signs of the mixing ratios as well as the magnitudes.

5.2 The Shell and Nilsson Models

The shell model is the most fundamental model of nuclear structure physics. Since single-particle effects are so evident in nuclei, any calculations attempting to describe details beyond the bulk, collective properties must include a description of the valence nucleons; and many nuclear properties result largely from the single-

particle motions. Calculations of binding energies (masses), ground-state moments or shapes, or excitation energies, for instance, are all properties which directly reflect the shell structure of nuclei. With this tenet, then, all of the phenomenological nuclear models can be thought of as shell models.

The early models sought to describe single-particle motion using either spherical square-well or harmonic-oscillator potentials. These potentials alone, however, could not reproduce the necessary energy gaps observed at the magic numbers. By adding a strong spin-orbit coupling term for the odd nucleon,

$$V_{s.o.} \propto \vec{l} \cdot \vec{s}$$

the energy gaps corresponding to the magic numbers were reproduced. In 1955 S. G. Nilsson [Nil55] refined the harmonic oscillator model by including a term proportional to $\vec{l}^2$ which lowers the energy of shells with high orbital momenta. Although there is no real physical justification for adding this "velocity-dependent term", it provides a major correction to the level spacings. Nilsson also used an axially-symmetric anharmonic oscillator, which provided the possibility of obtaining single-particle energies in a deformed potential. He was the first to calculate single-particle energies in a deformed nucleus using this technique: the Modified Harmonic Oscillator (MHO) or Nilsson Model.

The Modified Oscillator Hamiltonian is given as

$$H = \frac{P^2}{2M} + \frac{1}{2}M\left[\omega_\perp^2 (x^2+y^2) + \omega_z^2 z^2\right] + C\vec{l} \cdot \vec{s} + D\vec{l}^2 \qquad (31)$$

with the z axis defining the axis of symmetry. The oscillator potential is most often written in the "stretched" basis which unfortunately is less transparent than the Cartesian system shown in Equation (31) above. In this basis the oscillator potential takes on the form [Ben89]

$$V_{MHO}(\vec{r},\epsilon)=\frac{1}{2}\hbar\omega_0(\epsilon)\varrho_t^2\left[1+2\epsilon_1\left(\frac{4\pi}{3}\right)^{1/2}Y_{10}(\theta_t)\right.$$
$$\left.-\frac{2}{3}\epsilon_2\left(\frac{4\pi}{5}\right)^{1/2}Y_{20}(\theta_t)+2\sum_{\lambda=3}^{\lambda_{max}}\epsilon_\lambda\left(\frac{4\pi}{2\lambda+1}\right)^{1/2}Y_{\lambda 0}(\theta_t)\right] \tag{32}$$

with the stretched coordinates given by

$$\xi=x\left[\frac{m\omega_0(\epsilon)}{\hbar}(1+\epsilon_2/3)\right]^{1/2} \tag{33}$$

$$\eta=y\left[\frac{m\omega_0(\epsilon)}{\hbar}(1+\epsilon_2/3)\right]^{1/2} \tag{34}$$

$$\zeta=z\left[\frac{m\omega_0(\epsilon)}{\hbar}(1-2\epsilon_2/3)\right]^{1/2} \tag{35}$$

where ϵ represents the complete set of deformation parameters from ϵ_1 to $\epsilon_{\lambda max}$. The angle θ_t is defined as

$$\cos\theta_t=\frac{\zeta}{\varrho_t}=\left[\frac{1-2\epsilon_2/3}{1+\epsilon_2(1/3-\cos^2\theta)}\right]^{1/2}\cdot\cos\theta \tag{36}$$

with θ measured from the symmetry axis and

$$\varrho_t^2=\xi^2+\eta^2+\zeta^2. \tag{37}$$

As the nucleus is known to be nearly incompressible, the nuclear volume must be conserved as the nuclei become deformed. This constrains ϱ_t to values which meet

the condition that the equipotential nuclear surface is given by

$$R^2(\theta,\epsilon) = \frac{\hbar}{m\omega_0(\epsilon)}\left[\frac{1-2\epsilon_2/3+\epsilon_2\cos^2\theta_t}{(1-2\epsilon_2/3)(1+\epsilon_2/3)}\right]\varrho_t^2. \tag{38}$$

For very small deformations, mixing of adjacent oscillator shells cannot occur: neighboring shells have different parities, and the next nearest ($N\pm2$) shells are too far away in energy. For small deformations, then, the wavefunctions can be written in the spherical basis $|NLJm\rangle$. The single-particle energies in the deformed potential are then given by

$$E = \frac{2}{3}(N+3/2)\hbar\omega_0\epsilon\left[\frac{3\Omega^2-J(J+1)}{4J(J+1)}\right]. \tag{39}$$

For larger deformations J and L (total and orbital angular momenta of the odd nucleon) are no longer good quantum numbers, and so the asymptotic basis $|Nn_z\Lambda\Omega\rangle$ is used. The principal quantum number is given by $N=n_\perp+n_z$. Ω, Σ, and Λ are respectively the projections of total, spin, and orbital angular momentum on the symmetry axis, and therefore must meet the condition $\Omega=\Sigma+\Lambda$. A vector diagram showing the Nilsson quantum numbers is illustrated in Figure 27. The Nilsson wavefunctions are conventionally written as $\Omega^\pi[Nn_z\Lambda]$. When the axis of symmetry is also the rotation axis, Ω is referred to as K, and the rotational bands are most often labelled by that value. Finally, time-reversal symmetry leads to a degeneracy in Ω, so that each Nilsson orbital can accommodate up to two nucleons. A Nilsson diagram is shown in Figure 28 for odd-protons in the region of $Z=77$, illustrating the behavior of the Nilsson states as the nuclear deformation changes.

5.3 The Woods-Saxon Potential

Because of the unrealistic nature of the MHO potential, the more realistic Woods-Saxon potential (which doesn't need the $\vec{l}^2$ term to "fix up" the Hamiltonian)

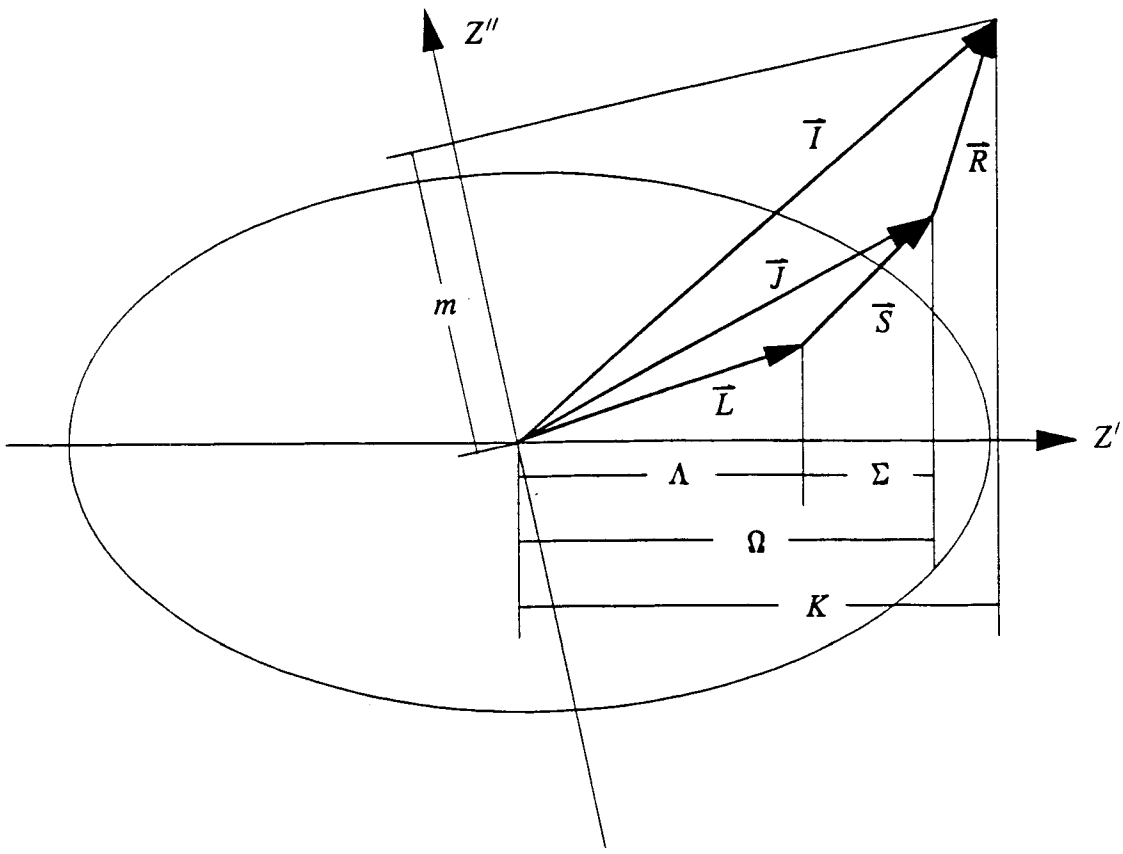

Figure 27 Vector-diagram of angular momenta involved in the Nilsson Model. The odd nucleon has angular momentum J, while the core has total angular momentum R.

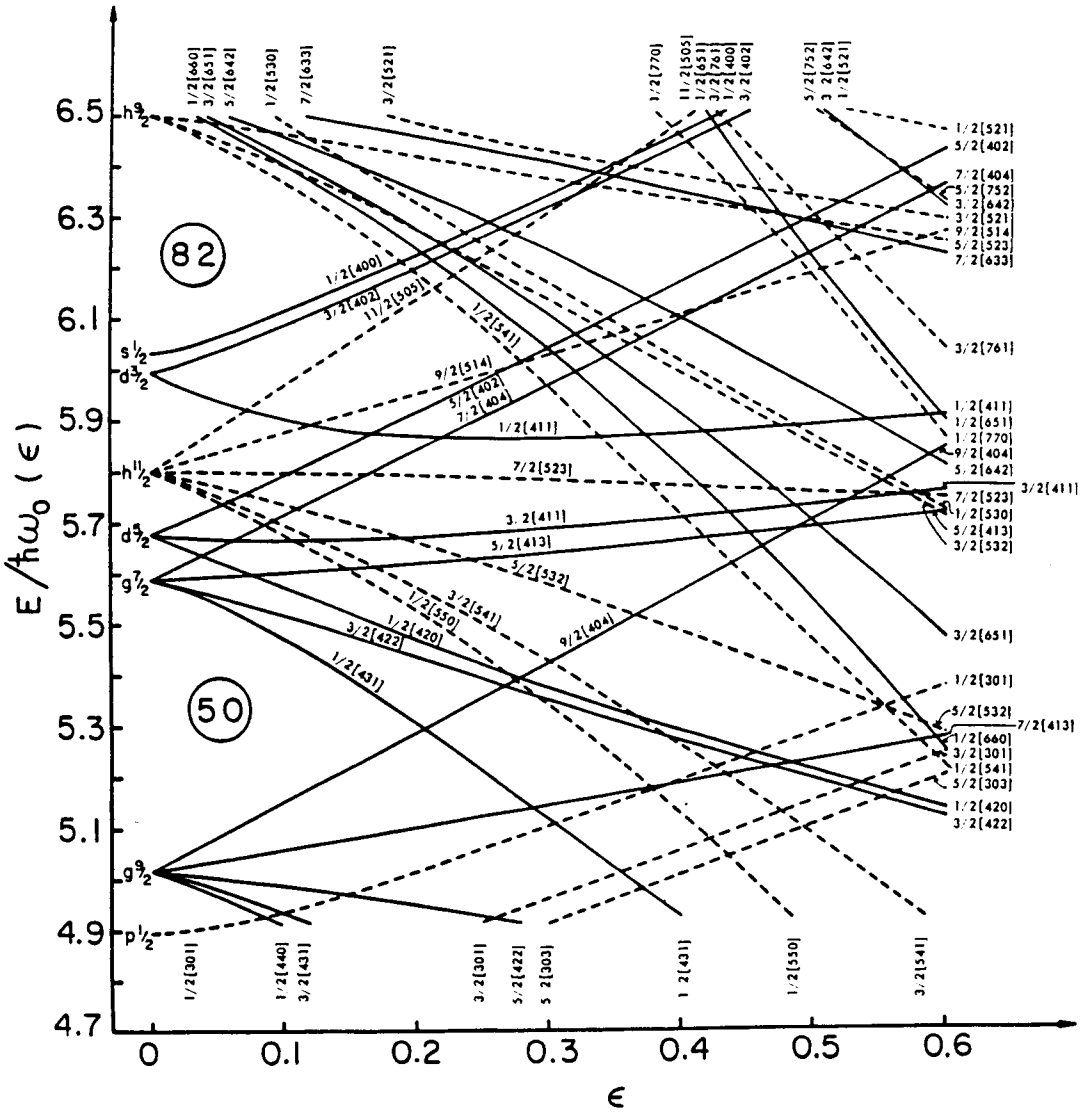

Figure 28 Nilsson diagram of single-particle orbits in a modified-oscillator potential for the Z=77 region. The orbitals are conventionally labelled $\Omega^{\pi}[Nn_z\Lambda]$.

is more often used in modern codes. Exact solubility of the harmonic oscillator makes its use very attractive, but the Woods-Saxon potential more accurately describes the density distribution of the nucleus, and is therefore often preferred. The deformed Woods-Saxon potential is given by

$$V(r,\hat{\alpha}) = \frac{V_0}{1+\exp[(|r| - R(\hat{\Omega},\hat{\alpha}))/a]} \tag{40}$$

where

$$R(\hat{\Omega},\hat{\alpha}) = c(\hat{\alpha})R_0\left(1+\sum_{\lambda\geq 2}\sum_{\mu}\alpha_{\lambda\mu}^{*}Y_{\lambda\mu}(\hat{\Omega})\right) \tag{41}$$

is the distance from the origin to the point on the nuclear surface whose position is specified by the angles $\Omega=(\theta,\phi)$, $R_0=r_0A^{1/3}$ is the radius of a spherical nucleus with the same volume (the volume condition being ensured by $c(\hat{\alpha})$), a is the diffuseness parameter describing the "skin-depth" of the nuclear surface, and $\hat{\alpha}$ describes the set of deformation parameters β_2, β_4, and γ (the quadrupole, hexadecupole, and triaxiality parameters, respectively). As can be seen from Equation (41), the deformation parameters result from a multipole expansion of the nuclear radius. The expansions are carried out in detail in Appendix B. Complete descriptions of the parameters used for the Woods-Saxon potential are given in [Cwi87] and [Lar78].

5.4 The Particle-Rotor Model

The Particle-Plus-Triaxial-Rotor Model (PTRM) was used to generate multipole mixing ratios for comparison with those extracted from conversion coefficients and NO data. The fortran codes used for the calculations were from P. Semmes [Sem91], and all calculations were done on a Digital Equipment Corporation MicroVAX II at Oregon State University. The first assumption in the PTRM is that the nucleus can be understood as a rigidly deformed quantum-mechanical rotor. That is to say that the core is not vibrationally "soft". The second is that there are no polarization effects (by which a nucleon in a high-angular-momentum orbit, such as $h_{11/2}$,

for instance, can alter the core shapes and properties). A single, unpaired nucleon (proton, for ^{187}Ir) orbits about the rigidly deformed core, then, with the Hamiltonian for the system given by

$$H=H_{core}+H_{s.p.}+H_{int} \tag{42}$$

The core Hamiltonian H_{core} is given by the familiar rigid rotor Hamiltonian

$$H_{core}=\frac{\hbar^2}{2J_0}I(I+1) \tag{43}$$

where J_0 is the moment of inertia of the core. The moment of inertia varies hydrodynamically with the triaxiality parameter γ according to the relation

$$J_\kappa=\frac{4}{3}J_0\left[\gamma+\kappa\frac{2\pi}{3}\right]. \tag{44}$$

The subscript κ here refers to the intrinsic axis, and takes on the values 1, 2, 3. The method of calculation is discussed below. The single-particle term $H_{s.p.}$ describes the motion of the unpaired nucleon in the spherical shell-model potential, either Woods-Saxon or Modified Oscillator. Finally, the interaction term contains a monopole (BCS-type) pairing term which provides particle-particle coupling and quadrupole-quadrupole or particle-hole coupling terms,

$$H_{int}= H_{pair}-\kappa q\cdot Q \tag{45}$$

where H_{pair} is the monopole pairing interaction between like nucleons and q and Q are respectively the quadrupole operators for the valence nucleon and the core.

The general scheme of the calculations is as follows: The single-particle energies and eigenfunctions (Nilsson orbitals) are found by solving the Schrödinger equation for the valence nucleon in the deformed mean-field (the deformation parameters β_2, β_4, and γ are input parameters describing this field). A truncated set of orbitals (≤ 15) from near the Fermi surface is then selected and used to construct the strong-coupled basis, in which single-particle properties will be calculated. There is

no mixing between levels of different parity (adjacent shells), so the parity is also selected for each set of Nilsson orbitals used in the basis. Pairing energies are then calculated using the BCS method, and finally the particle-plus-triaxial rotor Hamiltonian is diagonalized using the truncated set of orbitals. The final resulting wavefunctions are used to calculate electromagnetic matrix elements. As a final note, since the mixing ratios calculated in this way depend on the ratio of $E2$ to $M1$ transition probabilities, they are proportional to the theoretical energy as $\sqrt{E_{th}^5/E_{th}^3}$, so must be corrected by the ratio E_{exp}/E_{th} in order to compare them to experimental values.

5.4.1 Theoretical Results for ^{187}Ir

A Woods-Saxon potential was used for the mean-field, in which the only varied parameters were those of the deformation, *i.e.*, β_2, β_4, and γ. These deformation parameters are related to the ϵ parametrization of the MHO, and for small, axial deformations ($-0.2 \leq \beta_2 \leq 0.4$ and $-0.05 \leq \beta_4 \leq 0.15$) are approximated by

$$\epsilon_2 \approx 0.944\beta_2 - 0.122\beta_2^2 + 0.154\beta_2\beta_4 - 0.199\beta_4^2 \tag{46}$$

$$\epsilon_4 \approx -0.852\beta_4 + 0.141\beta_4^2 + 0.122\beta_2\beta_4 + 0.295\beta_2^2. \tag{47}$$

The deformation parameters used for the calculations were chosen as rather "middle-of-the-road" values, using various theoretical and experimental results [And75, Naz90, Sah81, Sch73, Vie79, Wys91]. They were varied only slightly around this region to find the best agreement with the largest number of mixing ratios. Illustrative results from Total Routhian Surface (TRS) calculations from [Wys91] are shown in Figures 29 & 30 for both ^{187}Ir and ^{189}Ir. These are results from Cranked Shell-Model calculations, in which the angular momentum is "cranked up" in steps and the single-particle energy in the "cranked", rotating frame (*ie.* the Routhian) is calculated as a function of deformation parameters β_2 and γ. The low-frequency calculations essentially reproduce Potential Energy Surface contours. The low-lying

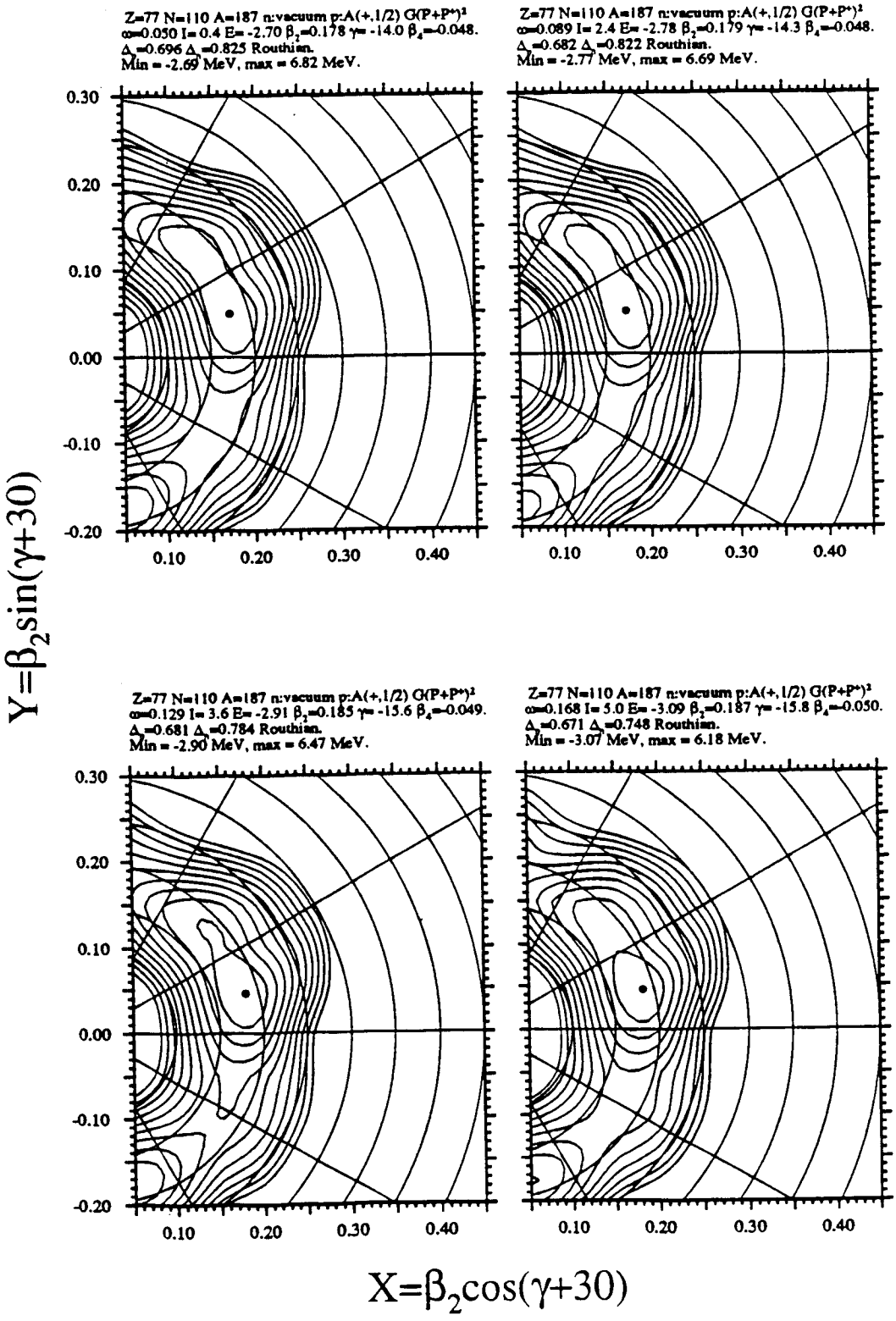

Figure 29 Total Routhian Surface (TRS) plots of ^{187}Ir, indicating the deformation parameters at the minima. Calculations were done by [Wys91] using a W-S potential.

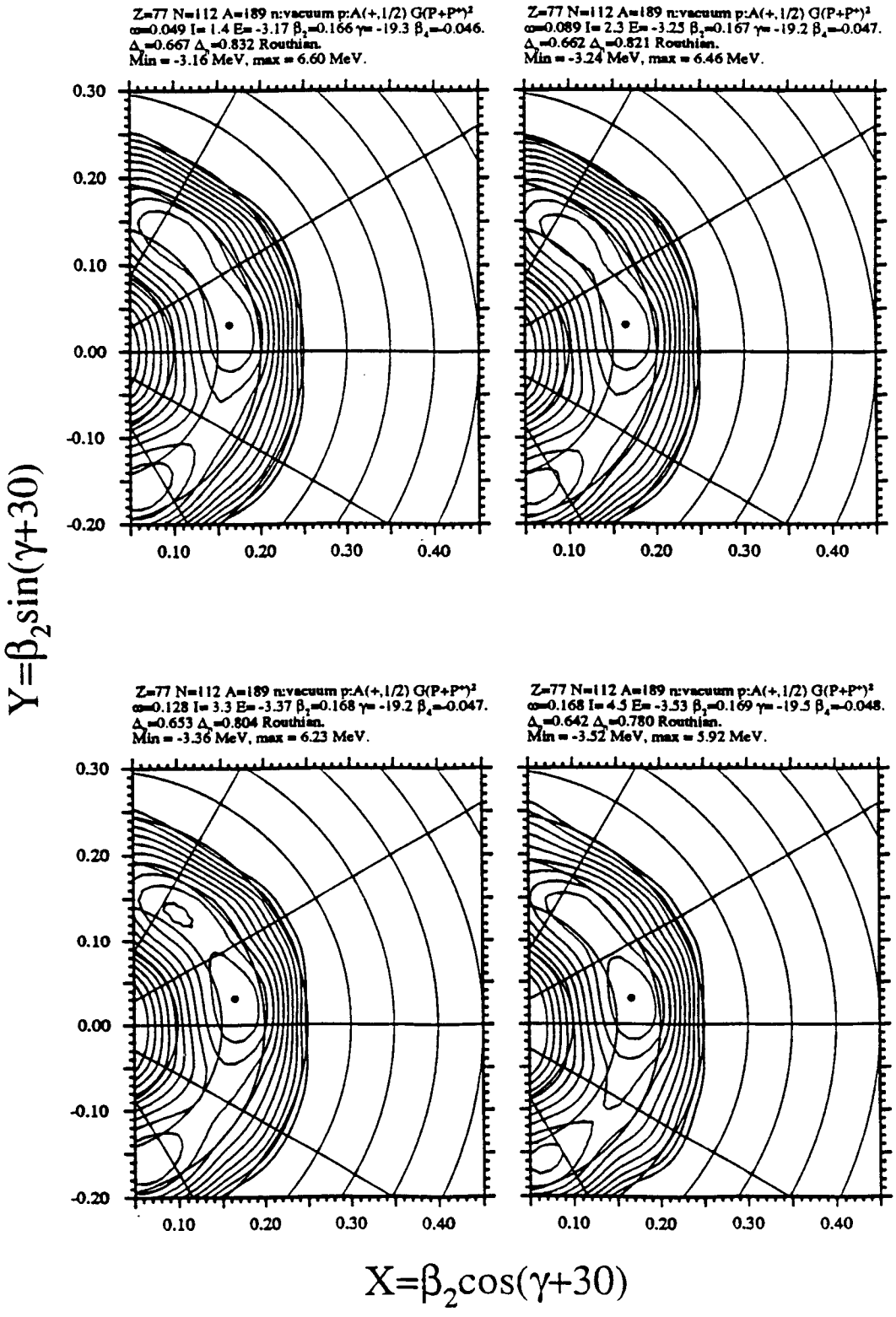

Figure 30 TRS plots for ^{189}Ir. The upper-left plot is the $\omega=0$ surface.

minimum is the ground-state, from which the deformation parameters for the central minimum can be found. While a minimum *is* reached for these nuclei, some gamma-softness is seen.

The moment of inertia parameter J_0 was calculated hydrodynamically using Grodzins' estimate [Rin80] for the energy of the first 2^+ excited state of the even-even cores of ^{187}Ir, and is given [Mey75] in terms of that energy as

$$E(2^+) = \frac{6\hbar^2}{2J_0} \frac{9-\sqrt{81-72\sin^2 3\gamma}}{4\sin^2 3\gamma}. \qquad (48)$$

The estimate for the first 2^+ energy lies near mid-range of the experimental values of 137 and 266 keV [Ram87] for ^{186}Os and ^{188}Pt respectively, and varies maximally with β,γ from 221 keV for $\beta_2=0.18$ and $\gamma=16°$, to 173 keV for $\beta_2=0.195$ and $\gamma=11°$. Standard values [Lar78, Sem91, Cwi87] for $Z=77$, $A=187$ were used for any other parameters in the calculation. Proton pairing-strengths, for example, given by

$$G_p=[17.90+0.176(N-Z)]/A \qquad (49)$$

produced a pairing gap of $\Delta=0.927$ MeV and a Fermi energy of $\lambda_f=-4.777$ MeV. The deformation parameters used in the calculation were $\beta_2=0.18$, $\beta_4=-0.048$, and $\gamma=16°$.

Positive-parity orbitals $|Nn_z\Lambda\Omega\rangle$ within approximately ± 5 MeV of the Fermi surface were included in the strong-coupling basis in which the calculations are performed. Although 11 orbitals were included in the basis, the resulting wave functions are generally characterized by admixtures of only two to three Nilsson orbitals. A well-known (but less well understood) feature of the particle-rotor model is that there is often too much Coriolis coupling of the orbitals, so the possibility of Coriolis attenuation also exists in the code. No attenuation was used for the present calculations, however.

Although the model is able to calculate both absolute and reduced transition probabilities, $B(E2)$ and $T(E2)$, for example, we are concerned only with the transition energies and multipole mixing ratios. Results of the calculations are shown in

Figure 31 and Table 9 for the energies and mixing ratios respectively. Calculated mixing ratios are found to agree remarkably well with data, and the signs are *all* consistent with present findings. A very dominant feature in all of the calculations is the appearance of the $5/2^+[402]$ band. This band has not been identified experimentally in ^{187}Ir, but shows up consistently in the calculations, with band-head energies ranging from 0 to about 400 keV for $0.17 < \beta_2 < 0.20$ and $14° < \gamma < 20°$. Some mixing of the $5/2^+$ members of the $d_{3/2}$ and $d_{5/2}$ bands causes a shift in the energies of the $d_{3/2}$ band along with complications in the transitional matrix elements. It might be useful to point out that in searching for candidates for the $d_{5/2}$ band, one should look for in-band transitions with relatively large *M1* strengths. This is because the $d_{5/2}$ is a spin-up configuration and the magnetic character should be enhanced over the corresponding electric one.

Calculations were not done for the negative-parity transitions, since there were few transitions among negative-parity levels for which mixing ratios (or angular distribution coefficients) were known. Many of the transitions from the negative-parity states populate the low-lying positive-parity bands, and transitions with a change in parity are not calculable in the PTRM. The few transitions for which both NO and conversion electron data were known (permitting determination of the signs of δ) are given in Table 9 even though theoretical values are not available.

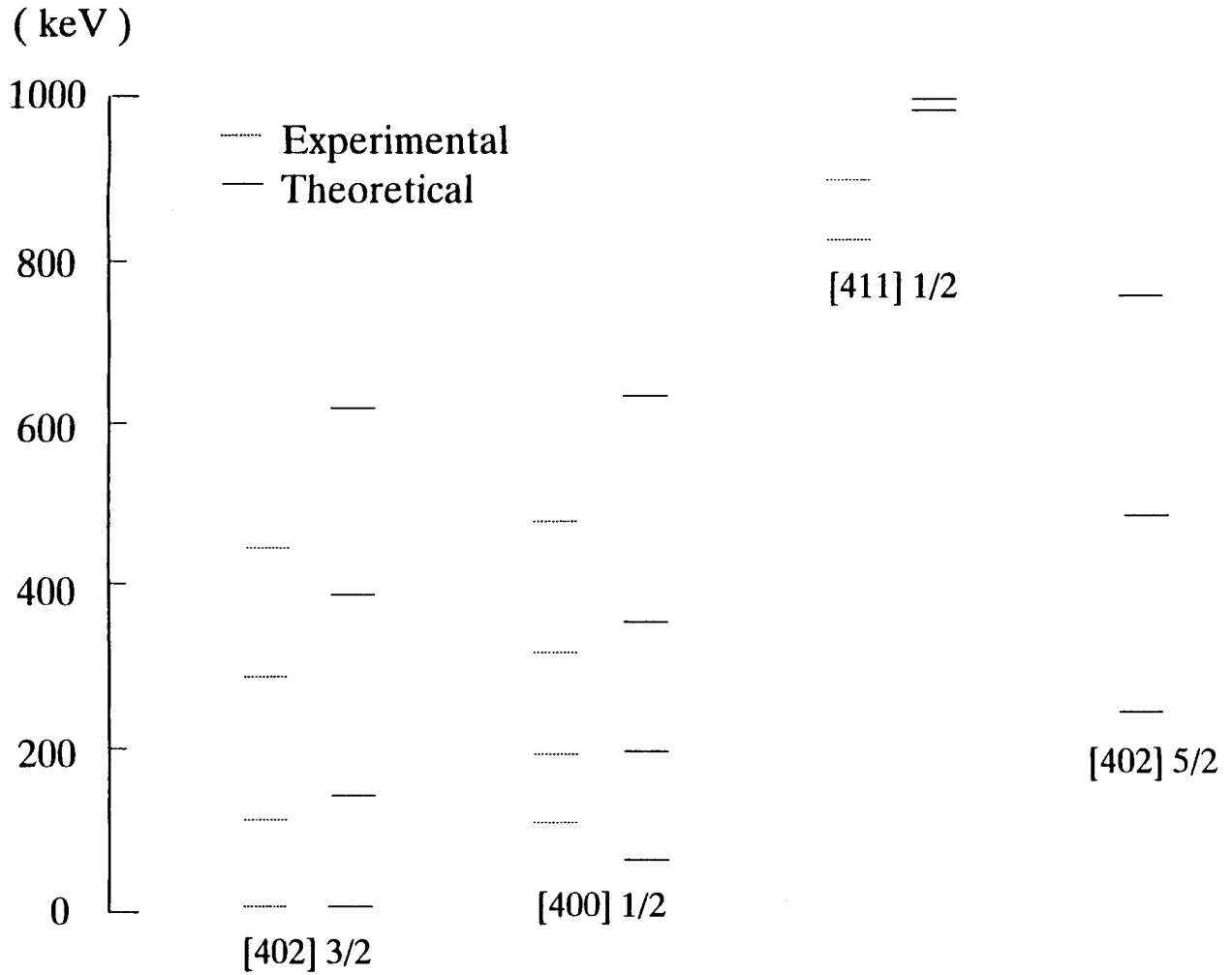

Figure 31 Level energies of the low-lying positive-parity bands in ^{187}Ir, along with theoretical results from the PTRM.

Table 9 Mixing ratios of transitions among positive-parity bands in ^{187}Ir. All signs are from the present study. Values shown are from the Particle-Plus-Triaxial-Rotor Model, conversion coefficients, nuclear orientation, and Nuclear Data Sheets.

E (keV)	δ_{PTRM}	δ_{cc}	δ_{NO}	δ_{NDS} [a)]
819.13	- 0.621	- 0.82(6)	-0.71^{+6}_{-5}	
712.45	- 0.855	- 1.06(5)		
629.27	+0.057	+0.52(3)		
361.09	- 0.419	< -0.14		
311.68	- 0.764	- 0.37(4)	-0.23^{+12}_{-15}	
189.61	- 0.980	-0.35^{+6}_{-9}		- 0.6(3)
122.09	+0.043	# 0.32(3)		< 0.2
110.17	- 0.355	- 0.78(3)		- 0.67(8)
106.55	- 0.041	> 13		
83.18	+0.376		+0.253(8)	+0.15(3)

a) From [Fir91].
#) NO data not available.

5.4.2 Theoretical Results for ^{189}Ir

Calculations were done for the positive-parity levels only, as most of the low-lying structure is due to those levels. Standard parameters were used as in the ^{187}Ir calculations. Only the deformation parameters and pairing strength parameters (which are standard values depending on mass) were different. The choice of deformation parameters were based again on various experimental and theoretical results (especially the TRS calculations of [Wys91] shown in Figure 30). They were varied slightly around these values to find the best agreement with level energy spacing of the $1/2^+[400]$ and $3/2^+[402]$ levels, and mixing ratios of transitions among those bands.

For purposes of calculations, the deformation parameters were chosen as $\beta_2=0.18$, $\beta_4=-0.046$, and $\gamma=19°$. These deformation parameters are very similar

to those used for ^{187}Ir, and were again found to agree remarkably well with experimental mixing ratios among the positive-parity bands. Also similarly to the ^{187}Ir calculations, the $d_{5/2}$ band is seen to come down in energy with increasing β_2,γ, until the band-head lies near 250 keV for the chosen parameters. This again causes some mixing of the $d_{5/2}$ band-head with the I=5/2 members of the $s_{1/2}$ and $d_{3/2}$ bands; the levels repel each other, and complications in the transitional matrix elements result. Despite this complication, however, both intraband and interband transitions are well reproduced. A compilation of mixing ratios for ^{189}Ir transitions is shown in Table 10. Where values were used from conversion coefficients, signs of mixing ratios were determined from the present study.

Table 10 Mixing ratios of transitions among positive-parity bands in ^{189}Ir.

E (keV)		δ_{PTRM}	δ_{NDS} [a]	δ_{NO}
186.7	7/2→5/2[402]	−0.322	−0.53(6)	$-0.36(^{+3}_{-4})$
113.8	5/2→3/2[402]	−0.391	0.64(15)	−0.64(15) [b]
351.0	7/2[400]→5/2[402]	−0.956		
147.1	7/2→5/2[400]	+0.201		
317.7	5/2[400]→3/2[402]	−2.615	−0.56(15)	−0.32(3)
203.9	5/2[400]→5/2[402]	−0.032	0.5(2)	$+0.01(^{+6}_{-5})$
141.2	5/2→3/2[400]	+0.051	0.12(5)	$+0.05(^{+2}_{-1})$
176.5	3/2[400]→3/2[402]	−0.624	0.88(7)	−0.88(7) [b]
82.2	3/2→1/2[400]	+0.271	0.17(2)	+0.17(2) [b]
62.7	3/2[400]→5/2[402]	+0.029	0.25(7)	
721.4	3/2[411]→3/2[402]	−0.615	$0.87(^{+23}_{-43})$	$-0.87(^{+23}_{-43})$
627.1	3/2[411]→1/2[400]	−0.692	−0.7(3)	
607.6	3/2[411]→5/2[402]	+0.204		
544.9	3/2[411]→3/2[400]	+0.058	+0.15(10)	
403.8	3/2[411]→5/2[400]	+0.116	$-0.02(^{+12}_{-8})$	
792.7	1/2[411]→3/2[402]	−0.548	1.0(4)	
616.1	1/2[411]→3/2[400]	+0.853		

a) From [Fir90].
b) Sign from present work, magnitude from [Fir90].

6. Remarks and Conclusions

Multipole mixing ratios have been found for transitions in ^{187}Ir from nuclear orientation and conversion electron spectroscopy. Angular distributions from the oriented ^{187}Pt nuclei were used to determine the signs for 9 transitions in ^{187}Ir, including magnitudes for several others. The most daunting problem encountered in the analysis of the NO data was the exceptionally large number of doublets in the spectrum, even excluding those from the buildup of Os. Analysis of many of the "key lines" in the decay scheme was clouded by this unfortunate occurrence. Finally, as is generally the case for odd-A isotopes -but which is even more pronounced in ^{187}Ir, there are very few $E2$ transitions with which to extract mixing ratios using the relative method. Only two mixing ratios were found using this technique; those of 311.7 and 551.6 keV. Additional mixing ratios, those of 83 and 819 keV, were found by using the known mixing ratios (and thus A_2's) of 189 and 712 keV respectively in a similar, relative technique.

The particle-plus-triaxial-rotor model was used to calculate mixing ratios for transitions among the positive-parity levels, and, using a deformation of β_2=0.18, β_4=-0.048, and γ=16°, was shown to agree very well with experimental data (see Table 9). It is believed that the very good agreement with data for the interband transitions is due mainly to the fact that the deformations of the two low-lying bands ($1/2^+$[400] and $3/2^+$[402]) are very similar. The deformation is an input parameter in the PTRM, and so transitions among bands with widely different deformations are not expected to be reproducible.

The decay scheme presented here accounts for much more decay intensity than previous studies. Approximately 92% of the gamma-ray intensity is included in the updated scheme. No previous decay studies had been done above 1.2 MeV, while there is a great deal of intensity up to about 2.4 MeV. The low-lying bands are heavily populated by these high-energy transitions. The high density-of-states near $E\sim 2$ MeV is not yet understood, but the pairing gap as calculated in the PTRM is nearly 1 MeV. This implies that some particle-particle coupling is responsible for this

feature. A rather interesting doublet of levels at 486 keV was also unraveled by gamma-ray coincidences, showing a lot of structure at those two levels. Several strong coincident cascades remain unplaced, even though coincidence rates were high enough to place them, were they feeding any of the known low-lying structure. The isomeric level at 186 keV complicates the assumption that these transitions populate the ground-state. The total intensity depopulating that level is also rather low, and it is difficult to say which of the unplaced cascades could populate the isomeric level.

Nuclear orientation was also performed on ^{189}Ir following the implantation of ^{189}Au. The spectrum of ^{189}Ir is very "clean" compared to that of ^{187}Ir; only two close doublets complicated the NO analysis of strong lines (those at 243/245, and 607/609 keV). Angular distributions were found for over 100 transitions in Ir. Coincidence data has not yet been fully analyzed, so the updated decay scheme is not yet complete. Mixing ratios have been found, however, for several transitions using the relative method and the decay scheme of [Hed72]. Signs of mixing ratios have again been found for those positive-parity transitions whose magnitudes were known from conversion electrons. Theoretical results from the PTRM agree very well with the experimental mixing ratios, as shown in Table 10. The deformation parameters used in the ^{189}Ir calculations were β_2=0.18, β_4=-0.046, and γ=19°.

Since, as is apparently evidenced by the negative-parity ground state, the most dramatic shape transition occurs in ^{185}Ir, it would be interesting to complete this work by including a NO study of ^{185}Ir. This would help to provide complete systematics over the entire range from A=185 to 193. The orientation of ^{185}Pt has already been performed at UNISOR but the data has not yet been fully analyzed.

References

[And75] S. Andre, J. Boutet, J. Rivier, J. Treherne, J. Jastrzebski, J. Lukasiak, Z. Sujkowski, and C. Sebille-Schuck, Nucl. Phys. **A243**, 229 (1975).

[Ben87] Ragnar Bengtsson, Tord Bengtsson, Jerry Dudek, Georg Leander, Witold Nazarawicz, and Jing-ye Zhang, Phys. Lett. **B183**, 1 (1987).

[Ben89] R. Bengtsson, J. Dudek, W. Nazarewicz, and P. Olanders, Physica Scripta, **Vol. 39**, 196, (1989).

[Bet76] D. S. Betts, *Refrigeration and Thermometry Below 1 Kelvin* (Sussex University Press, 1976).

[Boh69] A. Bohr and B. R. Mottelson, *Nuclear Structure, Vol. 1*, (Benjamin Inc., New York, 1969), p.382.

[Car76] H. K. Carter *et al.*, Nucl. Inst. and Methods **139**, 349 (1976).

[Cwi87] S. Cwiok, J. Dudek, W. Nazarewicz, J. Skalski, and T. Werner, Comp. Phys. Comm. **46**, 379 (1987).

[Deb79] Klaus Debertin and Ulrich Schötzig, Nucl. Inst. and Methods **158**, 471 (1979).

[Fir90] R. B. Firestone, Nucl. Data Sheets **59**, 869 (1990).

[Fir91] R. B. Firestone, Nucl. Data Sheets **62**, 222 (1991).

[Gha84] H. H. Ghaleb and K. S. Krane, Nucl. Phys. **A426**, 20 (1984).

[Gir88] I.C. Girit *et al.*, Hyp. Int. **43**, 151 (1988).

[Gum92] M. A. Gummin, K. S. Krane, Y. Xu, T. Lam, E. F. Zganjar, J. B. Breitenbach, B. E. Zimmerman, P. F. Mantica, and H. K. Carter, Hyp. Int., (Summer, 1992).

[Ham85] J. H. Hamilton, P. G. Hansen, and E. F. Zganjar, Rep. Prog. Phys. **48**, 631 (1985).

[Hax49] O. Haxel, J. H. D. Jensen, and H. E. Seuss, Phys. Rev. **75**, 1766 (1949).

[Hax50] O. Haxel, J. H. D. Jensen, and H. E. Seuss, Z. Physik **128**, 295 (1950).

[Hed72] G. Hedin and A. Backlin, Nucl. Phys. **A184**, 214 (1972).

[Her77] P. Herzog, H. -R. Folle, K. Freitag, M. Reuschenbach, and H. U. Schmidt, Phys. Lett. **62A**, 245 (1977).

[Her78] P. Herzog, H. -R. Folle, K. Freitag, A. Kluge, M. Reuschenbach, and E. Bodenstedt, Nucl. Inst. and Methods **155**, 421 (1978).

[Kem75] P. Kemnitz, L. Funke, H. Sodan, E. Will, and G. Winter, Nucl. Phys. **A245**, 221 (1975).

[Kra71] K. S. Krane, Los Alamos Scientific Lab. Report **LA-4677**, (1971).

[Kra72] K. S. Krane, Nucl. Inst. and Methods **98**, 205 (1972).

[Kra86] K. S. Krane, in *Low-Temperature Nuclear Orientation*, edited by N. J. Stone and H. Postma (North-Holland, Amsterdam, 1986), p. 89.

[Lar78] S. E. Larsson, G. Leander, and I. Ragnarsson, Nucl. Phys. **A307**, 189 (1978).

[Lat81] W. M. Lattimer, K. S. Krane, N. J. Stone, and G. Eska, J. Phys. G **7**, 1713 (1981).

[Leo87] William R. Leo, *Tehniques for Nuclear and Particle Physics Experiments:*

"A How to Approach" (Springer-Verlag, New York, 1987), p. 114.

[Lou74] O. V. Lounasmaa, *Experimental Principles and Methods Below 1K* (Academic Press, 1974).

[Mey75] J. Meyer-Ter-Vehn, Nucl. Phys. **A249**, 111 (1975).

[Mar86] H. Marshak, in *Low-Temperature Nuclear Orientation*, edited by N. J. Stone and H. Postma (North-Holland, Amsterdam, 1986), p. 769.

[May49] M. G. Mayer, Phys. Rev. **75**, 1969 (1949).

[May50] M. G. Mayer, Phys. Rev. **78**, 16 (1950).

[Mil87] W. T. Milner, *HHIRF Computer Handbook.*

[Mle81] R. L. Mlekodaj, E. F. Zganjar, and J. D. Cole, Nucl. Inst. and Methods **186**, 239 (1981).

[Naz90] W. Nazarewicz, M.A. Riley, and J.D. Garrett, Nucl. Phys. **A512**, 61 (1990).

[Nil55] S. G. Nilsson, Mat. Fys. Medd. Dan. Vid. Selsk. **29**, #16 (1955).

[Nuc90] Nuclear Data ND9900 MCA manual, Canberra Industries Inc..

[Rad71] R. Radebaugh and J. D. Siegwarth, Cryogenics 11, 368 (1971).

[Rag89] Pramila Raghavan, At. Data Nucl. Data Tables **42**, 189 (1989).

[Ram87] S. Raman, C. H. Malarkey, W. T. Milner, C. W. Nestor, Jr., and P.H. Stelson, At. Data Nucl. Data Tables **36**, 1 (1987).

[Rin80] P. Ring and P. Schuck, *The Nuclear Many-Body Problem* (Springer-Verlag, New York, 1980), p. 14.

[Ros78] F. Rosel, H. M Fries, K. Alder, and H. C. Pauli, At. Data Nucl. Data Tables **21**, 91 (1978).

[Rou69] J. T. Routti and S. G. Prussin, Nucl. Instr. and Methods **72**, 125 (1969).

[Sah81] R. Sahu, M. Satpathy, and L. Satpathy, Phys. Rev. **C23**, 1777 (1981).

[Sch73] C. Sebille-Schuck, M. Finger, R. Foucher, J. P. Husson, V. Berg, J. Jastrzebski, S. G. Malmskog, G. Astner, B. R. Erdal, P. Patzelt, and P. Siffert, Nucl. Phys. **A212**, 45 (1973).

[Sch79] C. Schuck, J. Genevey-Rivier, V. Berg, A. Knipper, G. Walter, C. Richard-Serre, and A. Hoglund, Nucl. Phys. **A325**, 421 (1979).

[Sem91] Unpublished lecture notes and Fortran codes from P. Semmes, *Nuclear Structure Theory Workshop*, ORNL (1991).

[Spe81] E. H. Spejewski, R. L. Mlekodaj, and H. K. Carter, Nucl. Inst. and Methods **186**, (1981).

[Ste75] R. M. Steffen and K. Alder in *The Electromagnetic Interaction in Nuclear Spectroscopy*, edited by W. D. Hamilton (North-Holland, Amsterdam, 1975).

[Vie79] Ch. Vieu, S. E. Larsson, G. Leander, I. Ragnarsson, W. DeWieclawik, and J. S. Dionisio, Z. Physik **A290**, 301 (1979).

[Whe74] J. C. Wheatly, R. E. Rapp, and R. T. Johnson, J. of Low Temp. Phys. **4**, 1 (1974).

[Wys91] R. Wyss, private communication.

[Zga88] E. F. Zganjar and J. L. Wood, Hyp. Int. **43**, 321 (1988).

Appendices

Appendix A

Solutions for a_λ.

The solutions to Equation (23) are given by

$$a_\lambda = \frac{c_{\lambda,0}R(0°)+c_{\lambda,45}R(45°)+c_{\lambda,90}R(90°)}{b_1R(0°)+b_2R(45°)+b_3R(90°)} \tag{50}$$

with the definitions

$$\begin{aligned}
c_{2,0} &= -3/8\ Q_4(90°) - 13/32\ Q_4(45°) \\
c_{2,45} &= 3/8\ Q_4(90°) - Q_4(0°) \\
c_{2,90} &= Q_4(0°) + 13/32\ Q_4(45°) \\
c_{4,0} &= -1/2\ Q_2(90°) - 1/4\ Q_2(45°) \\
c_{4,45} &= 1/2\ Q_2(90°) + Q_2(0°) \\
c_{4,90} &= 1/4\ Q_2(45°) - Q_2(0°) \\
b_1 &= 3/32\ Q_2(45°)Q_4(90°) - 13/64\ Q_2(90°)Q_4(45°) \\
b_2 &= -3/8\ Q_2(0°)Q_4(90°) - 1/2\ Q_2(90°)Q_4(0°) \\
b_3 &= -1/4\ Q_2(45°)Q_4(0°) - 13/32\ Q_2(0°)Q_4(45°)
\end{aligned}$$

The uncertainties in the a_λ are given by

$$\delta a_\lambda = \left[\sum_{\theta=0,45,90} \left(\frac{\partial a_\lambda}{\partial R(\theta)} \right)^2 (\delta R(\theta))^2 \right]^{1/2} \tag{51}$$

where the derivatives are equal to

$$\frac{\partial a_\lambda}{\partial R(0°)} = \frac{R(45°)(b_2c_{\lambda,0}-b_1c_{\lambda,45})+R(90°)(b_3c_{\lambda,0}-b_1c_{\lambda,90})}{\left[b_1R(0°)+b_2R(45°)+b_3R(90°)\right]^2} \tag{52}$$

$$\frac{\partial a_\lambda}{\partial R(45°)} = \frac{R(0°)(b_1c_{\lambda,45}-b_2c_{\lambda,0})+R(90°)(b_3c_{\lambda,45}-b_2c_{\lambda,90})}{\left[b_1R(0°)+b_2R(45°)+b_3R(90°)\right]^2} \tag{53}$$

$$\frac{\partial a_\lambda}{\partial R(90°)} = \frac{R(0°)(b_1c_{\lambda,90}-b_2c_{\lambda,0})+R(45°)(b_2c_{\lambda,90}-b_3c_{\lambda,45})}{\left[b_1R(0°)+b_2R(45°)+b_3R(90°)\right]^2}. \tag{54}$$

In the six-detector configuration we have 8 independent sets of rates with which to calculate the a_λ. For ^{187}Pt orientation, detectors at 0, 45, 90, 135, 180, and 270° were used. For the ^{189}Pt orientation the 135° detector was replaced with that of 225°. Analysis proceeds as follows:

Detectors				
0	45	90	⇒	$a_2 \pm \delta a_2$ and $a_4 \pm \delta a_4$
0	45	270	⇒	$a_2 \pm \delta a_2$ and $a_4 \pm \delta a_4$
0	135	90	⇒	$a_2 \pm \delta a_2$ and $a_4 \pm \delta a_4$
0	135	270	⇒	$a_2 \pm \delta a_2$ and $a_4 \pm \delta a_4$
180	45	90	⇒	$a_2 \pm \delta a_2$ and $a_4 \pm \delta a_4$
180	45	270	⇒	$a_2 \pm \delta a_2$ and $a_4 \pm \delta a_4$
180	135	90	⇒	$a_2 \pm \delta a_2$ and $a_4 \pm \delta a_4$
180	135	270	⇒	$a_2 \pm \delta a_2$ and $a_4 \pm \delta a_4$

A weighted average of these values is then taken. Since each detector is used 4 times in the averaging, the resulting weighted uncertainty must be multiplied by $\sqrt{4}$. (*ie.*, the final uncertainty is twice the weighted average uncertainty.)

Appendix B

Deformation Parameters for Triaxial Deformations.

In slightly simplified notation, the expansion of Equation (41) up to quadrupole deformation is:

$$R = cR_0\left\{1+\alpha_{20}Y_{20}+\alpha_{21}\left(Y_{21}+Y_{2-1}\right)+\alpha_{22}\left(Y_{22}+Y_{2-2}\right)\right\}. \tag{55}$$

The major axis is chosen such that $\alpha_{21}=0$. We then define

$$\begin{aligned}\alpha_{20} &= \beta_2\cos\gamma \\ \alpha_{22} &= \frac{1}{\sqrt{2}}\beta_2\sin\gamma,\end{aligned} \tag{56}$$

with the constraint that

$$\alpha_{20}^2+\alpha_{22}^2+\alpha_{2-2}^2=\beta_2^2. \tag{57}$$

The $\gamma=0°$ (prolate), $\gamma=30°$(maximal triaxiality), and $\gamma=60°$ (oblate) shapes are simply understood using these definitions. The hexadecupole deformations are given by the additional expansion terms

$$\alpha_{40}Y_{40}+\alpha_{42}\left(Y_{42}+Y_{4-2}\right)+\alpha_{44}\left(Y_{44}+Y_{4-4}\right). \tag{58}$$

There are three hexadecupole deformation parameters; β_4^A, β_4^B, and β_4^C, and the $\alpha_{\lambda\mu}$ are given in terms of them as

$$\alpha_{40} = \tfrac{1}{6}\left[\beta_4^A\left(5\cos^2\gamma+1\right)+\beta_4^B\left(5\cos^2 2\gamma+1\right)+\beta_4^C\left(7\cos^2\gamma-4\right)2\cos\gamma\right] \tag{59}$$

$$\alpha_{42} = \tfrac{1}{6}\left(\tfrac{15}{2}\right)^{1/2}\left[\beta_4^A\sin 2\gamma-\beta_4^B\sin 4\gamma-\beta_4^C\sin\gamma\right] \tag{60}$$

$$\alpha_{44} = \tfrac{1}{6}\left(\tfrac{35}{2}\right)^{1/2}\left[\beta_4^A\sin^2\gamma+\beta_4^B\sin^2 2\gamma+\beta_4^C\sin 2\gamma\,\sin\gamma\right]. \tag{61}$$

In PTRM calculations using the Woods-Saxon potential, β_4^B and $\beta_4^C=0$.